COUPLED CFD-FEM SIMULATION OF FLOATERS WITH MOORING SYSTEMS

A Dissertation

by

HAN HUANG

Submitted to the Office of Graduate and Professional Studies of
Texas A&M University
in partial fulfillment of the requirements for the degree of

DOCTOR OF PHILOSOPHY

Chair of Committee,	Hamn-Ching Chen
Committee Members,	Bert Sweetman
	Kuang-An Chang
	Moo-Hyun Kim
Head of Department,	Sharath Girimaji

May 2021

Major Subject: Ocean Engineering

ABSTRACT

The Finite-Analytic Navier-Stokes (FANS) computational fluid dynamics (CFD) code is coupled with an in-house nonlinear finite element (FEM) mooring analysis program, MOORING3D, to study the dynamic responses of a floating body with a mooring system in complicated environmental conditions. A six degree-of-freedoms (DoFs) motion solver based on the 4th order Runge-Kutta scheme is used as the interface between CFD and the MOORING3D. A specially designed coupling methodology to adapt to the Runge-Kutta scheme is developed. The hydrodynamic loads on the moored floating system are estimated by the CFD using the large eddy simulation (LES) model. The FANS code is solved in conjunction with the level-set (LS) formulation to model free surface effects. The 3rd order TVD (total variation diminishing) Runge-Kutta scheme and the 3rd order ENO (essentially non-oscillatory) scheme are used to numerically solve level-set values. Besides, the methodology is developed for an overset grid system of embedding, overlapping, and moving structured grids.

The dynamic responses of a catenary anchor leg mooring (CALM) buoy system in waves and currents are simulated with the coupled method to demonstrate its feasibility. The simulation results are compared against numerical simulations based on potential flow theories and available experimental measurements. The free-decay motions, wave-induced motions, and wave-current-body interaction are investigated. The agreements between the simulated response amplitude operators (RAOs) and the experimental data provide validations for the coupled method. The results also show the potential capability

of the coupled method in addressing much more complicated free surface flow simulations.

The coupled method is additionally applied to investigate the vortex-induced motion (VIM) of a deep draft semi-submersible platform. The VIM of semi-submersible is gaining increasing attention from both industry and academia with the recent development of semi-submersible platforms. The mooring-induced damping effects on VIM are investigated through the coupled CFD-FEM analysis. The LES turbulence model is used to provide accurate estimation of hydrodynamic loading. Varying reduced velocities are considered. The simulated VIM responses are compared with experiments and previous numerical simulations. The results reveal the mooring-induced damping to be a critical factor contributing to the VIM response reduction in the field. The reduction ratio matches well with the previous model tests and field measurements. The results demonstrate that the coupled FANS-MOORING3D code proves to be a powerful tool for the study of complex fluid-body-mooring interaction.

ACKNOWLEDGEMENTS

I would like to express my deepest gratitude to the advisor and committee chair, Dr. Chen, for his instruction and support throughout my study. Without his guidance, I would never have reached the current research step. I also deeply appreciate his understanding and patience in terms of my personal situations as a part-time Ph.D. student.

I would like to extend my gratefulness to my committee members, Dr. Chang, Dr. Kim, and Dr. Sweetman, for their valuable time, suggestions, and personal encouragement.

Thank Mr. Roy Bleiberg, Mr. Mathew Chakala, and Mr. Lin Zhao in American Bureau of Shipping, for their support throughout the study.

Thanks Dr. Jun Zhang, advisor of my master study, for encouraging me to pursue Ph.D. degree with having a full-time job.

Thanks also go to my friends and colleagues and the department faculty and staff for making my time at Texas A&M University a great experience.

Finally, thanks to my mother and father for their encouragement, support, understanding, and love.

CONTRIBUTORS AND FUNDING SOURCES

TABLE OF CONTENTS

LIST OF FIGURES

LIST OF TABLES

CHAPTER I

INTRODUCTION

1.1 Background and Significance

The objective of this dissertation is to develop a general, accurate, and robust program package, which incorporates computational fluid dynamics module and nonlinear finite element cable dynamic analysis program MOORING3D. The CFD module is based on the Finite-Analytic Navier-Stokes numerical method to solve the unsteady, incompressive Navier-Stokes equation (Chen et al., 1990; Pontaza et al., 2005). The FANS method is capable of not only solving the flow field and predicting velocity and pressure, but also incorporating state-of-the-art turbulence models and free surface models to address challenging fluid dynamics problems including the vortex street formation, the deforming free surface flows, etc. The cable dynamic analysis program MOORING3D and its coupling with the FANS code aim at accurate solutions for mooring dynamics and the interactions between mooring systems and floaters.

The current software which are capable of coupled time domain analysis of the floating system in the marine and offshore industry have their own pros and cons. Programs based on potential flow theory, like WAMIT and AQWA, are the mainstream programs to solve the hydrodynamic loads on floating bodies based on diffraction theory. The hydrodynamic properties obtained from diffraction analysis, including wave load RAO, added mass, radiation damping, hydrostatic stiffness, etc., can be the input of other

time domain analysis programs, in which mooring system is simulated and the floater is treated as a rigid body. For instance, the hydrodynamics output from AQWA can be loaded into Orcaflex for the time-domain analysis; the hydrodynamics output from WAMIT can be the input of SESAM, etc.

However, the commercial software based on potential flow theory neglect viscous effects. Also, the current approach involves collaborative use of different software. The hydrodynamic load, mooring system dynamics, and their interaction cannot be solved simultaneously within one computer program. The popular mooring analysis programs, like Orcaflex and AQWA-NAUT, use lumped mass method. In this dissertation, CFD is used instead of potential flow theories with the capability to address highly complicated flow problems considering viscous effects and free-surface effects. The MOORING3D based on nonlinear FEM is used to solve the mooring dynamics and is to be compared with Orcaflex. The coupling between CFD and the FEM mooring analysis program has rarely been studied previously and is achieved in this dissertation.

Engineering applications of the coupled FANS-MOORING3D code will involve the time domain analysis of most typical floating systems, including SPAR, tension leg platform (TLP), semi-submersible (semi) platform, floating production, storage & offloading (FPSO), catenary anchor leg mooring (CALM) buoy system, floating wind turbine, etc. Various typical types of mooring systems can be simulated by the coupled method, including slack mooring system, truncated mooring system, or semi-taut mooring system.

Two types of floating systems are selected for the in-depth research and investigation. The first floater type is the CALM buoy. The responses of the CALM buoy in wavs and currents are of great interest to the academia and industry, due to its wide application in industry and the highly non-linear motion behavior. The second floater type studied is the semi-submersible platform. The vortex-induced motion of semi-submersible is a crucial issue in designing the platform and mooring lines and risers connected to the hull. The literature review of the existing studies on two types of floaters is presented in the next section. The literature review gives an overview of current developments and approaches with their advantages and disadvantages discussed. It is then followed by a section which outlines the main topics and contributions of this dissertation. The chapter is closed with the organization of the dissertation.

1.2 Literature Review

1.2.1 Numerical Simulations of CALM Buoy

The CALM buoy system is now widely used in many areas (Sagrilo et al., 2002) as an efficient and economic single point mooring system. CALM buoys, which are often connected to FPSOs with two or three large flowlines, are very popular nowadays in the deep-water areas like West Africa oil fields for the offloading purpose. More than 300 systems are being used since the first one was deployed in the 1960's. Compared to other floating structures like FPSOs or TLP, CALM buoy is more sensitive to the response of mooring lines due to its considerably small inertia, damping and hydrostatic stiffness. These features of buoy can result in dangerous motions which may cause fatigue damage

in mooring and flowlines systems. Therefore, the accurate estimation of dynamic motion for CALM buoys is very essential.

Many studies on numerical simulation of CALM buoy wave-induced response have been carried out. Diffraction/radiation theory was used to estimate the hydrodynamic loads and forced oscillation tests were implemented to validate hydrodynamic behavior of the buoy (Kang et al., 2014; Le Cunff et al., 2007; Katayama et al., 2009). Unidirectional nonlinear hybrid wave model (HWM) was also used by the researchers for the estimation of hydrodynamic loads on the buoy, considering the wave kinematics up to second order in wave steepness (Song et al., 2014). In the HMW approach, the coupled dynamic analysis of the CALM buoy system was achieved, with hydrodynamic loads estimated by HWM and mooring system modeled with the non-linear FEM method (Chen et al., 2002; Song et al., 2014). Regarding other approaches for mooring system simulation, varying schemes were utilized, such as lumped mass method (Bunnik et al., 2002) and nonlinear spring replacement method (Sagrilo et al., 2002).

CFD is also used to study the hydrodynamic behavior of the CALM buoy. The Reynolds Averaged Navier-Stokes Equations solver was used to obtain the diffracted flow field and achieved the estimation of hydrodynamic loads on an adaptive CALM buoy (Monroy et al., 2011). However, the buoy model was kept captive by a framed structure without considering the dynamic coupled interaction from the mooring lines. A numerical tool based on the open source CFD toolbox OpenFOAM for application to floating offshore wind turbines was developed, with integration of a quasi-static mooring line

4

analysis model (Liu et al., 2017). However, the quasi-static and dynamic methods for mooring modeling yield discrepancy in body-mooring interaction.

Considering the cable dynamics, the EU FP5 EXPRO-CFD Project developed a commercial CFD software to allow prediction of the response of floating structures in waves. The EXPRO-CFD system is made up from the CFD code CFX, coupled to the AQWA-LINE and AQWA-NAUT hydromechanics codes in accordance with Woodburn et al. (2005). CFX provides the hydrodynamic forces and moments at each time step in the motion simulation, with the dynamics of the floating structure, its moorings and riser/export lines modeled in the AQWA-NAUT software. AQWA-NAUT returns the structure's displacements and velocities to the CFD model to couple motions and fluid flow. The turbulence was modeled using a two-equation k-e model in CFX. The mooring lines in AQWA-NAUT were modeled as rod elements by using the lumped mass method, which was like Orcaflex.

However, the coupling between CFX and AQWA-NAUT was a simplified coupling process in the EXPRO-CFD system, with hydrodynamic loads or mooring loads updated once in each time step. The coupled code required back-and-forth data transfer between two commercial software, slowing down the simulation processes. The model of the CALM buoy in the study of Woodburn et al. (2005) consisted of 200,000 meshes and was limited to adjacent areas of the buoy, meaning the model was designed focusing on wave-induced motions but was not capable of modeling vortex and the resultant VIM if considering current loads. Only motions in three DoFs were reported. The 200,000-mesh system required considerable computation time of one day for about 4000 time steps.

Even though CFD has been recognized as being advantageous in capturing vortex and viscous effects, the diffraction analysis is still a popular approach in industry. The benefits of this conventional method are obvious with its short computation time. The concern is the use of linear hydrodynamic coefficients and empirical estimation on drag loads, which exerts adverse consequences on accuracy of motion which is sensitive to non-linear effects and viscous effects.

Both Woodburn et al. (2005) and Ryu et al. (2006) conducted experiments and numerical simulations based on diffraction theory for the CALM buoy. In accordance with simulations of Ryu et al. (2006), wave loads, added-mass, and radiation damping were calculated based on diffraction theory, and high empirical drag coefficients were used for the time-domain analysis to model viscous effects. It proves that viscous effects play a critical role in the buoy responses besides inertial effects.

The accuracy of conventional numerical simulations highly relies on the reasonable estimation of drag coefficients and damping induced by vortex shedding. Also, the conventional numerical methods use linear added mass, radiation damping, and wave excitation loads in most cases, neglecting the non-linear hydrodynamic effects brought about by changing free surface. CFD can calculate nonlinear effects of wave loads, added-mass, radiation damping, and viscous effects by pressure and shear force integration over the instantaneous wetted surface. The vortex shedding can also be captured by CFD simulation.

1.2.2 VIM of Semi-submersible Platforms

The VIM of semi-submersible offshore platforms becomes a crucial issue as the development of deep draft semi-submersible is gaining increasing popularity for the offshore oil and gas production. At present, the model tests have been the industry-recognized method for estimating the VIM response of semi-submersibles. Waals et al. (2007) conducted experiments on VIM of semi-submersible floaters. In this model test, two soft springs were used to provide the horizontal restoring force to model the mooring system of the floater. However, recent studies performed by Irani et al. (2015), Ma et al. (2013), and Rijken et al. (2009) indicate that the VIM response in the field is much less than as observed in the model tests. For example, Ma et al. (2013) pointed out that amplitudes of VIM in the field appear much smaller than the observation in model tests, with a reduction ratio of as much as 50%. The approach of only using standard model test information leads to the overly conservative estimation of VIM amplitudes. Consequently, the strength check and VIM fatigue life design of mooring lines and risers are affected with significant impact on costs.

The differences between field measurements and model test observations are likely due to different mass ratios, wave effects in the field, Reynolds number, appurtenance structures, and external damping induced by mooring lines and risers. Koop and Wilde (2016) demonstrated that changing the mass ratio of the floater has a small influence on the VIM response. Also, the effect of unsteady current on the VIM response is minimal. Regarding wave damping effects on VIM, the experiments revealed that VIM response under inline or transverse waves is smaller than that without waves and depends on wave

heading and wave height. The VIM response shows a significant reduction or even disappears in large waves (100 year or Hurricane waves) in accordance with Hong et al. (2008) and Goncalves et al. (2013). The reduction in VIM response is negligible in small waves as found in operational seas according to Martin et al. (2012) and Koop and Wilde (2016). The waves are small or absent during loop-current events. Therefore, damping effects associated with waves in operational sea states are not the main reason for the considerable reduction of VIM response as observed in the field.

Regarding effects of appurtenance structures, Koop, and Wilde (2016) indicates that the small appurtenance structures are commonly omitted in VIM model tests for multicolumn semi-submersibles. Rijken et al. (2011) proves that the effect of the appurtenance appears to have only minimal effects on the VIM response. The appurtenance includes riser porches, riser guards, fairleads, anodes, caissons, etc. An increased modeling detail of appurtenance does not significantly change the VIM response. Hence the appurtenance structures are not the reason causing considerable reduction of VIM response in the field.

In terms of the effects of Reynolds number, Chen et al. (2016) used the Finite-Analytic Navier-Stokes (FANS) CFD method for the simulation of semi-submersible VIM response, in both model scale and prototype scale, and compared their numerical results with existing model tests. The simulation results revealed that the computed flow fields and VIM amplitudes in model and full scales are quite similar, and the predicted VIM amplitudes are close to those obtained from the model tests. The research verified the

validity of scaling law and indicated that the Reynolds number is not the factor leading to the VIM response reduction in the field.

Turing to the effects of external damping provided by mooring system and risers, Koop et al. (2016) included the external damping in the CFD calculations and demonstrated that the damping effect of mooring system is an important factor for the observed difference between model tests and field measurements. However, mooring damping levels are dependent on the number of mooring lines, water depth (WD), mooring configuration, etc., and how VIM amplitude reduction responds to different damping levels is unknown. The estimation of mooring damping effects was empirical based on the approach of Koop et al. (2006). The accurate evaluation of mooring damping effects and mooring dynamics effects should be evaluated by a more comprehensive analysis approach.

1.3 Methods of Present Study

The numerical method coupling CFD and nonlinear FEM mooring analysis module is presented in this dissertation. If free-surface effects are critical, the coupled CFD-FEM code is used in conjunctive with the level-set method resolving the free-surface on an overset grid system. Interface-capturing method based on the level-set method has been incorporated. The 3rd order TVD Runge-Kutta scheme (Yu et al, 2003) is used for time derivatives. The 3rd order ENO scheme for spatial derivatives is extended from a two-dimensional (2D) simulation case to three-dimensional (3D). Overset grid method is used

to accommodate the buoy motion in the fixed boundary meshes, largely reducing the computational costs and allowing the motion simulation in all six DoFs.

The in-house MOORING3D code is a cable dynamic analysis program based on a nonlinear FEM theory. The theory was originally established by (Garrett et al., 1982) to solve inextensible line problems, which was the original version of CABLE3D code. It was then developed by (Ma et al., 1994) to analyze rods with small elongations and sea bottom effects. Then the original CABLE3D code was modified by introducing large elongation elements without bending stiffness and verified that the modified algorithm of mooring model is more robust and reliable (Chen et al., 2002). MOORING3D is an in-house mooring analysis code originally developed by (Gu et al., 2017) based on the theory identical to the improved CABLE3D (Chen et al. 2002). The MOORING3D program is improved to address multiple lines and multiple element types and to adapt to the six-DoF motion solver. The mooring line is treated as a long slender structure neglecting bending moments and shear forces.

The level-set FANS adjunctive code and the MOORING3D are coupled to model the dynamic interaction between the floating body and its mooring system, aiming at simulating flow field, free surface, and dynamics of mooring system interaction, and fluid-body interaction simultaneously. The LES model is incorporated as the turbulence model. The six-DoF motion solver program based on 4th order Runge-Kutta scheme serves as the interface between CFD and the MOORING3D to achieve the capacity of addressing both translational and rotational motion. The floater response including highly nonlinear responses in complicated conditions can be estimated with the coupled program package.

1.4 Research Scope

　　The level-set FANS conjunctive method is a well-validated approach in simulating highly complicated free-surface effects. Yu (2009) used the conjunctive code to simulate the green water inundation over the bridge and the wave slamming on the deck. Several program modifications and developments are conducted based on the original code.

- The LES with Smagorinsky subgrid-scale stress (SGS) model had been shown to provide accurate predictions of vortex-induced vibrations of deepwater risers in uniform and shear currents (Huang et al., 2010, 2012). However, the LES model was not included in the original level-set FANS conjunctive code for the two-phase flow simulation. The original code used unsteady RANS equation with the conventional k-ε model for closure. The novelty of the research includes that the LES is incorporated in the level-set FANS code to address the wave-induced motion and wave-current-body interaction of the buoy. The large-scale filtered turbulence is directly solved by the LES model, while the turbulence within the grid is estimated by Smagorinsky model and cannot be solved by k-ε model. The program modification and development are validated by performing the VIM simulations of a semi-submersible with an ideal spring representing the mooring constraint loads. The resultant VIM response is compared to previous model tests and numerical simulations.

- The original version of the MOORING3D was developed by Gu et al. (2017) and could model mooring lines with only one type of element. However, the mooring lines may have different segments with different materials. For instance, the semi-taut chain-polyester rope-chain mooring system is often deployed for semi-submersible platforms, and connectors with lumped mass are used between different segments. Another novelty of the research is that the MOORING3D program is rewritten to include multiple element types to extend the functionality. The extended MOORING3D is verified by modeling various typical types of mooring systems, including slack-chain mooring system, truncated mooring system, and semi-taut chain-rope-chain mooring system. The simulated results are compared with commercial software for verification, which is presented in Section 4.4 and Section 6.3.

- The TVD-ENO level-set numerical scheme developed by Yu (2009) is expanded to three-dimensional in this research. The simulation case of bridge deck slamming done by Yu (2009) is two-dimensional. However, for the buoy simulation in this dissertation, three-dimensional simulation is required for the accurate estimation of free-surface effects and viscous effects by pressure and shear stress integration over the instantaneous wetted surface. The 2nd and 3rd order TVD-ENO schemes should be equivalent after extending to three-dimensional. Therefore, both schemes

are used for wave surface simulation for program self-verification. The three-dimensional 3rd order TVD-ENO scheme is also tested in terms of green water effects. The verification is presented in Section 4.5.

- The two-dimensional bridge deck slamming case performed by Yu (2009) does not introduce the use of moving overset grid system, since no motion needs to be addressed. The buoy studied in this research has small mass and is highly sensitive to nonlinear effects and viscous effects, therefore the accurate estimation of wave loads, added mass, viscous effects, radiation, and free surface effects is critical. The moving overset grid approach by the program PEGSUS is used to accurately estimate the hydrodynamic loads over the wetted surface and predict motion responses. Also, different overset methods can be used based on application types. The verification of overset methods is presented in Section 4.6.

- The MOORING3D is coupled with the six-DoF motion solver and the level-set FANS CFD module on the overset grid system. The coupled CFD-FEM analysis to address both translational and rotational motion of moored floaters has not been performed before and is one of primary novelties of this dissertation. The coupling process needs to address data transfer and coordinate system switch among different modules. The methodology is a specially designed process adapting to the 4th order Runge-Kutta method,

in which the MOORING3D and the motion solver are called for four times within each individual time step. The precision of Runge-Kutta method is improved to achieve a more robust coupling between the MOORING3D, motion solver, and CFD module. The new methodology is validated by comparing the simulated free-decay motions of the CALM buoy with experiments. The validations for free-decay tests are presented in Section 4.7. Further validations are performed by simulating wave-induced motion and wave-current-body interactions of the CALM buoy. The simulated RAOs are validated against experimental measurements. This part of validation is presented in Chapter V. In addition, the coupled CFD-FEM method can be used for VIM simulations of a moored semi-submersible platform. The simulation results agree well with the trend observed in field observation. This part of validation is presented in Chapter VI. The coupled CFD-FEM method is superior to the conventional approach based on potential flow theory in terms of more accurately modeling nonlinear hydrodynamic effects, free surface effects, and viscous and turbulent effects.

Based on the above research efforts, the dissertation covers the following three independent research topics, which are the contents of three journal papers.

The first topic is the coupled CFD-mooring simulations for wave-induced motion of a CALM buoy system with a slack-chain mooring system. The identical models are

created by commercial software AQWA and Orcaflex. The motion of the CFD-mooring analysis is compared to results of commercial software. The investigation of difference between the two approaches reveals inefficiencies of the conventional one and advantages of the CFD-mooring coupled analysis. Even though no direct experimental data is available for this CALM buoy, the comparison of AQWA simulations and experiments of a similar CALM buoy are available in the existing literature review. The published studies of Woodburn et al. (2005) had indicated disadvantages of the diffraction analysis in solving the CALM buoy's motion. The comparison of our simulations and results of Woodburn et al. (2005) additionally indicates the drawbacks of diffraction analysis and the CFD analysis should yield closer results to experiments. The first topic is covered in Chapter IV and Chapter V.

The second topic is the coupled CFD-mooring simulations for free-decay motions, wave-induced motion, and wave-current-body interactions of a CALM buoy system with a truncated mooring system. The resultant motions are compared against model tests of (Ryu et al., 2006) for validation. The mooring system was modeled as catenary cables for this CALM buoy in previous studies (Gu et al., 2017) to provide similar hydrodynamic performance as the CALM buoy model test. However, the method of equivalent truncated mooring system was employed in the model test (Ryu et al., 2006). Truncated mooring system needs to be modeled to thoroughly replicate the model tests. The truncated mooring system is used instead of the catenary mooring system to attain a more straightforward comparison with the experimental measurements. The second topic is covered in Chapter IV and Chapter V.

The third topic is the VIM simulations of a semi-submersible platform with a semi-taut chain-polyester rope-chain mooring system at ultra-deep water areas. Different mooring systems at various water depths or with different mooring configurations are designed by the MOORING3D. Full-scale mooring systems with different mooring systems are simulated for the consideration of different damping levels. The VIM amplitudes with different mooring system are compared to the simulated amplitudes of the damping-free cases and the experimental amplitudes. In-depth studies are performed for a wide range of reduced velocities from 7 to 15 to cover the lock-in and post-lock-in conditions. The simulation results demonstrate that the mooring-induced damping effect is probably the primary cause of the reduction of VIM motion response in the field. In addition, a sensitivity study of how drag coefficients of mooring lines affect the VIM response is also performed. The third topic is covered in Chapter VI.

1.5 Organization

Chapter II describes the mathematical model of level-set RANS method and the incorporation of large eddy simulation. The governing equations of level-set RANS method are given in the physical plane. Chapter II also describes the FEM model of mooring lines based on theory of slender body dynamics incorporating large elongation elements.

Chapter III presents the numerical models for level-set equations and the application of overset grid method. Chapter III describes the interface between CFD

16

module and mooring analysis module and describes the coupling procedure and the six-DoF motion solver based on 4th order Runge-Kutta method.

Chapter IV presents the CALM buoy model description, which is used to verify and validate the level-set RANS method, overset grid method, and the coupling between CFD and MOORING3D. Chapter IV also presents several types of mooring system of the CALM buoy. The mooring systems are modeled by the MOORING3D, including taut truncated mooring system and slack chain mooring system.

Chapter V presents the simulations for wave-induced motion and wave-current-body interaction of the CALM buoy. The comparison between the coupled CFD-mooring analysis, commercial software analysis, and experimental measurements show that the coupled CFD-mooring method can predict floater motion accurately.

Chapter VI presents the VIM simulation of semi-submersible. The effects of mooring-induced damping on semi VIM response are investigated. The simulation results explain the significant reduction of VIM response in field measurements compared to model tests is probably due to mooring-induced damping effects.

Chapter VII presents summary and conclusions.

CHAPTER II

MATHEMATICAL MODEL

2.1 Introduction

This chapter describes the mathematical model of level-set RANS method and the cable dynamics model based on the nonlinear FEM theory. The general equations of level-set function and RANS governing equations are given. The governing equations for the mooring line dynamic analysis are presented.

2.2 Level Set Equations

The level-set method is applied to capture the air-water interface for the simulation of waves and free surface effects. One of the challenges of simulating free surfaces by CFD lies on how to track the air-water interface. The interface-tracking and interface-capturing methods are the common approaches of solving air-water interface.

The interface-tracking methods follow the free surface motion and use boundary-fitted grids which are adjusted at each time step following the free surface motion. Turning to the interface-capturing methods, the computation of the interface is typically performed on a fixed grid, which is extended beyond the free surface. The shape of this free surface is determined by cells that are partially filled. The level-set method is one of the most typical numerical strategies to predict interface motion among several interface-capturing methods. Yu (2007) and Chen et al. (2009) used the level-set FANS method to model

violent free surface. Zhao (2014) proposed a coupled level-set and volume-of-fluid method to model sloshing and green water effects.

The level-set FANS method of Chen et al. (2009) is employed for the wave simulation in the present study. The Navier–Stokes equations are solved in conjunction with the level-set formulation for wave-current-body interaction problems. The level set function, specified as ϕ, is the signed distance from the interface, which is air-water interface in this study. The region of each phase can be distinguished by the sign of the level set function:

$$\phi(x,t) \begin{cases} < 0: & air \\ = 0: & interface \\ > 0: & water \end{cases} \tag{2.1}$$

The advection equations of the level set function during time t with the underlying velocity $\overrightarrow{V}$ are written as follows:

$$\frac{\partial \phi}{\partial t} + \overrightarrow{V} \cdot \nabla \phi = 0 \tag{2.2}$$

Both the density and viscosity at air–water interfaces depend on the level-set values being a distance function. The fluid properties are assumed to vary smoothly across a narrow transition zone around the free surface. The transition zone is defined by $|\phi| \leq \varepsilon$, where ε is half of the thickness of the interface. In the transition of the interface, the fluid properties are smoothed by Heavi-side function $H(\phi)$:

$$H(\phi) = \begin{cases} 0 & if \ \phi < -\varepsilon \\ \frac{1}{2}\left[1 + \frac{\phi}{\varepsilon} + \frac{1}{\pi}\sin\left(\frac{\pi\phi}{\varepsilon}\right)\right] & if -\varepsilon \leq \phi \leq \varepsilon \\ 1 & if \ \phi > \varepsilon \end{cases} \tag{2.3}$$

More specifically, the density and viscosity are calculated in the following manner respectively:

$$\rho(\phi) = \rho_a + (\rho_w - \rho_a) \cdot H(\phi) \tag{2.4}$$

$$\mu(\phi) = \mu_a + (\mu_w - \mu_a) \cdot H(\phi) \tag{2.5}$$

where the subscripts 'a' and 'w' represent air and water, respectively. This enables the accurate and stable numerical results for free surface simulation.

2.3 RANS Equations

The fluid field around the buoy is computed by unsteady incompressible three-dimensional RANS method in time domain, which is called the Finite Analytic Navier-Stokes code (Chen et al., 2013; Chen et al., 1988, 1989; Huang et al., 2012; Pontaza et al., 2004, 2005).

LES with Smagorinsky model is used to model the sub-grid scale turbulence in this study. The fluid domain is divided into finite volume scheme to solve the continuity equation. The LES turbulence model, which applies volume-averaging Navier-Stokes equation, is used to model the turbulence. Small scale vorticity is filtered out with this method to improve the computational efficiency as well as ensure the simulation quality. Equation 2.6 is the non-dimensional differential equation used by LES turbulence model. Dynamic pressure is considered in this equation.

$$\frac{\partial \overline{u}_i}{\partial t} + \frac{\partial}{\partial x_j}\left(\overline{u}_i \overline{u}_j\right) = -\frac{1}{\rho}\frac{\partial \overline{p_d}}{\partial x_i} + \frac{\nu}{Re}\frac{\partial^2 \overline{u}_i}{\partial x_j \partial x_j} - \frac{\partial \tau_{ij}}{\partial x_j} \tag{2.6}$$

where p_d is dynamic pressure, Re is the Reynolds number, and τ_{ij} is the subgrid-scale

Reynold stress tensor. τ_{ij} is determined by Smagorinsky's subgrid-scale turbulence

model shown from Eq. (2.7) to (2.11).

$$\tau_{ij} = \overline{u_i u_j} - \overline{u}_i \overline{u}_j \tag{2.7}$$

$$\tau_{ij} = -2\nu_t \overline{S_{ij}} \tag{2.8}$$

$$\nu_t = (C_S \Delta)^2 \sqrt{2\overline{S_{ij}} \cdot \overline{S_{ij}}} \tag{2.9}$$

$$S_{ij} = \frac{1}{2}\left(\frac{\partial \overline{u}_i}{\partial x_j} + \frac{\partial \overline{u}_j}{\partial x_i}\right) \tag{2.10}$$

$$\Delta = \left(\Delta_x \Delta_y \Delta_z\right)^{1/3} \tag{2.11}$$

$$C_S = 0.1 \tag{2.12}$$

where $\overline{S_{ij}}$ is the local strain tensor, C_S is the Smagorinsky's coefficient, and Δ is a vorticity

size value which filter out any vorticity smaller than it. The LES turbulence model had

been shown to provide accurate predictions of vortex-induced vibrations (VIV) of deep

water risers in uniform and shear currents (Huang et al., 2010, 2012) as well as vortex and

wake-induced vibrations (WIV) of dual risers in tandem and side-by-side arrangements

(Chen et al., 2013).

The RANS equations are rewritten in the level-set formulation while employing

the level-set method to solve free-surfaces. The total pressure is to be solved, which is

different from Equation 2.6. The gravity term is considered in the RANS equation to

generate the gravitational waves. It is assumed both water and air are governed by the

incompressible Navier-Stokes equations.

$$\frac{\partial \bar{u}_i}{\partial t} + \frac{\partial}{\partial x_j}\left(\bar{u}_i \bar{u}_j\right) = -\frac{1}{\rho(\phi)}\frac{\partial \bar{p_t}}{\partial x_i} + \frac{\nu(\phi)}{Re}\frac{\partial^2 \bar{u}_i}{\partial x_j \partial x_j} - \frac{\partial \tau_{ij}}{\partial x_j} - \frac{\delta_{i,3}}{Fr^2} \tag{2.13}$$

where p_t is total pressure and Fr is the Froude number. The density and viscosity are dependent on the level-set values. ρ_a and ν_a are used while the grid is in air, and ρ_w and ν_w are used while the grid is in water. The LES model is incorporated into the level-set RANS equation to model turbulence and free surfaces simultaneously.

2.4 MOORING3D

Based on the motion equation of a cable in Cartesian coordinate (Lindahl et al., 1983), the governing equation describing the motion of a cable can be deduced as

$$\left(\tilde{\lambda}\mathbf{r}'\right)' + \mathbf{q} = \rho \ddot{\mathbf{r}} \tag{2.14}$$

where

$$\tilde{\lambda} = \frac{T}{1+\varepsilon} \tag{2.15}$$

$$\varepsilon = \frac{T}{EA} \tag{2.16}$$

where T is the tension tangential to cable's direction, EA is the elastic stiffness of the cable, $\mathbf{r}$ is a vector to describe the configuration of the cable, which is a function of the deformed arc length of cable s and time t, and is shown in Figure 1 cited from Chen's paper (Chen, 2002). $\mathbf{q}$ stands for external force per unit length. ρ is the mass of the cable per unit unstretched length.
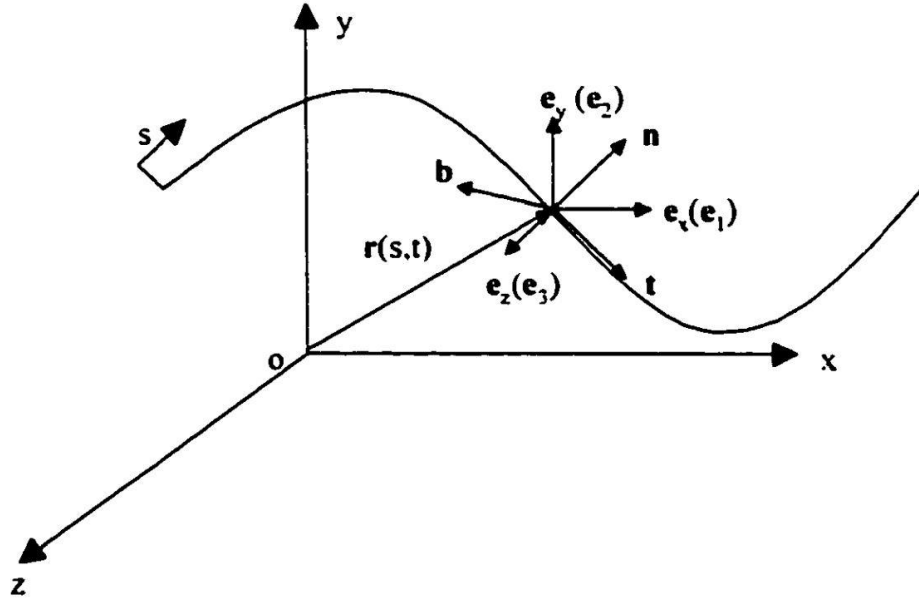
Figure 1. Coordinate System of the MOORING3D (Chen, 2002)

The external forces **q** is composed of hydrostatic, hydrodynamic, and gravity forces. The gravity force is expressed like

$$\mathbf{q}_t(s, t) = -\rho_t g A_t \mathbf{e}_y \tag{2.17}$$

The hydrodynamic force is divided into added-mass force, drag force, and Froude-Krylov force. The added-mass force and drag force can be predicted with Morrison equation.

After dividing the external force into these three parts, the governing equation becomes

$$\mathbf{M}\ddot{\mathbf{r}} - \left(\tilde{\lambda}\mathbf{r}'\right)' = \mathbf{q} \tag{2.18}$$

where

$$\mathbf{M} = \rho_f A_f \mathbf{I} + \rho_f A_f C_{Mn}(1 + \varepsilon)\mathbf{N} + \rho_f A_f C_{Mt}(1 + \varepsilon)\mathbf{T} \qquad (2.19)$$

$$\mathbf{q} = \left(\rho_f A_f - \rho_t A_t\right)g\mathbf{e}_y + \rho_f A_f(1 + \varepsilon)(\mathbf{I} + C_{Mn}\mathbf{N} + C_{Mt}\mathbf{T})\mathbf{a}_f$$

$$+ \frac{1}{2}\rho_f D_f C_{Dn}(1 + \varepsilon)\mathbf{N}(\mathbf{v}_f - \dot{\mathbf{r}})\left|\mathbf{N}(\mathbf{v}_f - \dot{\mathbf{r}})\right|$$

$$+ \frac{1}{2}\rho_f D_f C_{Dt}(1 + \varepsilon)\mathbf{T}(\mathbf{v}_f - \dot{\mathbf{r}})\left|\mathbf{T}(\mathbf{v}_f - \dot{\mathbf{r}})\right| \qquad (2.20)$$

$$\mathbf{T} = \frac{\mathbf{r}'^{^T}\mathbf{r}'}{(1+\varepsilon)^2} \qquad (2.21)$$

Besides, the configuration vector $\mathbf{r}$ must obey the stretching constrain equation:

$$\mathbf{r}' \cdot \mathbf{r}' = (1 + \varepsilon)^2 \qquad (2.22)$$

which can also be interpreted as

$$\mathbf{r}' \cdot \mathbf{r}'(1 - \tilde{\varepsilon})^2 = 1 \qquad (2.23)$$

with

$$\tilde{\varepsilon} = \frac{\tilde{\lambda}}{EA} \qquad (2.24)$$

The foundation of predicting the hydrodynamic behavior of cable with large elongation and no bending stiffness is established with governing equation (2.18) together with rod constraint equation (2.22). Hermite cubics/quadratics shape functions are used to discretize the coefficients in summation form. Galerkin's method is applied to discretize the partial differential terms. The governing equations of each element become

$$\gamma_{ikm}M_{njm}\ddot{u}_{kj} + \beta_{ikm}\tilde{\lambda}_m u_{kn} = \mu_{im}q_{mn} + f_{in} \qquad (2.25)$$

and cable constraint equation

$$\frac{1}{2}\beta_{ikm}u_{in}u_{kn} + \frac{1}{2}\tilde{\eta}_{iklm}\left(-2\tilde{\varepsilon}_l + \tilde{\varepsilon}_l^{\ 2}\right)u_{in}u_{kn} - \frac{1}{2}\tau_m = 0 \qquad (2.26)$$

where

$$u_{1n}(t) = \mathbf{r_n}(0,t),\ u_{2n}(t) = L\ \mathbf{r_n}'(0,t),\ u_{3n}(t) = \mathbf{r_n}(L,t),\ u_{4n}(t) = L\ \mathbf{r_n}'(L,t),$$

$$\tilde{\lambda}_1(t) = \tilde{\lambda}(0,t),\ \tilde{\lambda}_2(t) = \tilde{\lambda}(L/2,t),\ \tilde{\lambda}_3(t) = \tilde{\lambda}(L,t),\ \text{and}$$

$$q_{1n} = q_n(0,t),\ q_{2n} = q_n(L/2,t),\ q_{3n} = q_n(L,t),$$

L refers to the element length. j and n are index from 1 to 3 indicating the three dimensions. i and k run from 1 to 4, indicating the index of Hermite cubic shape functions. l and m run from 1 to 3, indicating the index of the quadratic shape functions.

The unknowns of original governing equations are $\mathbf{r}$ and $\tilde{\lambda}$. In terms of these set of ordinary differential equations, the unknowns are $\ddot{u}_{kj}$, u_{kn} and $\tilde{\lambda}_m$. By adopting Newmark-β method elaborated in (Chen, 2002), the acceleration term $\ddot{u}_{kj}$ can be written as term relating to u_{kj}. Therefore, each element has 15 unknowns through the discretized equation. After applying the boundary conditions, the modified equations can be written in a matrix form as $\mathbf{A}\delta\mathbf{x} = \mathbf{b}$, with $15 + 8(N-1)$ independent equations to describe the mooring line with N elements in three dimensions. This method has been proved efficient in predicting the hydrodynamic response of the cables (Chen, 2002).

CHAPTER III

NUMERICAL MODEL

3.1 Introduction

This chapter describes the finite difference scheme for level set equation. In addition, the chapter describes the interface between the CFD and the mooring modules and how the two modules are coupled. The algorithm for six-DoF motion solver and the associated coupling algorithm are elaborated.

3.2 CFD Module

3.2.1 Level-set Numerical Scheme

The contravariant velocity components (Chen and Patel, 1989) are introduced to express the level set evolution equation in the transformed coordinates (ξ^i, τ).

$$U^i = JV^i = \sum_{j=1}^{3} b^i{}_j U_j \tag{3.1}$$

$$\frac{\partial \phi}{\partial \tau} + \sum_{i=1}^{3} \frac{\partial (U^i \phi)}{\partial \xi^i} = 0 \tag{3.2}$$

The above equation is advanced using the 3rd order TVD Runge-Kutta scheme (Yu and Chen, 2006) which is total variation stable：

$$\begin{cases} \phi^{(1)} = \phi^n - \Delta\tau \cdot L(\phi^n) \\ \phi^{(2)} = \frac{3}{4}\phi^n + \frac{1}{4}\phi^{(1)} - \frac{\Delta\tau}{4} \cdot L(\phi^{(1)}) \\ \phi^{n+1} = \frac{1}{3}\phi^n + \frac{2}{3}\phi^{(2)} - \frac{2\Delta\tau}{3} \cdot L(\phi^{(2)}) \end{cases} \tag{3.3}$$

where $L(\phi) = \sum_{i=1}^{3} \frac{\partial (U^i \phi)}{\partial \xi^i}$. The subscript n and n+1 refer to the time step.

Various ENO schemes are used to discretize the spatial operator L, including the 2nd order and the 3rd order scheme. In this dissertation, the 3rd order scheme is further developed to expand from two-dimensional to three-dimensional. The spatial operator is discretized in the transformed plane (ξ, η, ζ) in a conservative manner.

$$\sum_{i=1}^{3} \frac{\partial(U^i \phi)}{\partial \xi^i} = (U^1 \phi)_{i+\frac{1}{2},j,k} - (U^1 \phi)_{i-\frac{1}{2},j,k} +$$

$$(U^2 \phi)_{i,j+\frac{1}{2},k} - (U^2 \phi)_{i,j-\frac{1}{2},k} + (U^3 \phi)_{i,j,k+\frac{1}{2}} - (U^3 \phi)_{i,j,k-\frac{1}{2}} \quad (3.4)$$

The 3rd order ENO scheme is specified as follows:

$$\phi_{i+\frac{1}{2}} = \begin{cases} \frac{11}{6}\phi_{i+1} - \frac{7}{6}\phi_{i+2} + \frac{1}{3}\phi_{i+3}, & \text{if } r_3 = -1 \\ \frac{1}{3}\phi_i + \frac{5}{6}\phi_{i+1} - \frac{1}{6}\phi_{i+2}, & \text{if } r_3 = 0 \\ -\frac{1}{6}\phi_{i-1} + \frac{5}{6}\phi_i + \frac{1}{3}\phi_{i+1}, & \text{if } r_3 = 1 \\ \frac{1}{3}\phi_{i-2} - \frac{7}{6}\phi_{i-1} + \frac{11}{6}\phi_i, & \text{if } r_3 = 2 \end{cases} \quad (3.5)$$

with r_3 defined as follows:

$$r_3 = \begin{cases} r_1, & \text{if } \left|\delta\phi_i^{-r_1+1}\right| \geq \left|\delta\phi_i^{-r_1}\right| \text{ and } \left|\delta^2\phi_i^{-r_1+1}\right| \geq \left|\delta^2\phi_i^{-r_1}\right| \\ r_1 - 1, & \text{if } \left|\delta\phi_i^{-r_1+1}\right| < \left|\delta\phi_i^{-r_1}\right| \text{ and } \left|\delta^2\phi_i^{-r_1}\right| \geq \left|\delta^2\phi_i^{-r_1+1}\right| \\ r_1 + 1, & \text{if } \left|\delta\phi_i^{-r_1+1}\right| \geq \left|\delta\phi_i^{-r_1}\right| \text{ and } \left|\delta^2\phi_i^{-r_1+1}\right| < \left|\delta^2\phi_i^{-r_1}\right| \\ r_1, & \text{if } \left|\delta\phi_i^{-r_1+1}\right| < \left|\delta\phi_i^{-r_1}\right| \text{ and } \left|\delta^2\phi_i^{-r_1+2}\right| < \left|\delta^2\phi_i^{-r_1+1}\right| \end{cases}$$

$$(3.6)$$

where r_1 is defined as:

$$r_1 = \begin{cases} 1 & \text{if } U^n_{i+\frac{1}{2}} \geq 0 \\ 0 & \text{if } U^n_{i+\frac{1}{2}} < 0 \end{cases} \quad (3.7)$$

denoting:

$$
\begin{cases}
\delta\phi_i^{-1} = \phi_i - \phi_{i-1} \\
\delta\phi_i^0 = \phi_{i+1} - \phi_i \\
\delta\phi_i^1 = \phi_{i+2} - \phi_{i+1}
\end{cases}
\qquad
\begin{cases}
\delta^2\phi_i^{-1} = \phi_{i-2} - 2\phi_{i-1} + \phi_i \\
\delta^2\phi_i^0 = \phi_{i-1} - 2\phi_i + \phi_{i+1} \\
\delta^2\phi_i^1 = \phi_i - 2\phi_{i+1} + \phi_{i+2} \\
\delta^2\phi_i^2 = \phi_{i+1} - 2\phi_{i+2} + \phi_{i+3}
\end{cases}
$$

Yu et al. (2007) introduced the 2nd order ENO scheme. Yu et al. (2007) simulated the green water over a bridge by using the 3rd order TVD Runge-Kutta scheme and the ENO scheme of both 2nd and 3rd order. However, the 3rd order ENO scheme was limited to two-dimensional for the case of green water simulation. The CALM buoy is modeled with a three-dimensional wave surface to be generated in this dissertation; therefore, the two-dimensional 3rd order TVD and ENO schemes are extended to three-dimensional. The extended 3rd order TVD and ENO schemes are verified by comparing to the 2nd order scheme.

3.2.1 Overset Grid Method

The overset grid method is used by decomposing the grid into a few computational blocks in the current level-set RANS method. The continuity equation and Navier-stokes equations are solved in the multi-block overset grids. The grid near the structure can be refined to get accurate solutions. The PEGSUS program (Suhs and Tramel 1991) is employed to determine the interpolation information for linking grids before calculations. Information between each two adjacent subdomains is transferred by overlapping common region between both borders. Information transferred include velocities, pressure, viscosity, level-set values, etc.

Two approaches are used to accommodate the motions of floating body. Self-verification of the coupled code can be performed by comparing the simulation results of the two approaches.

The first approach can be used if only horizontal motions of surge and sway are considered. All blocks are moving together with the floating body in this approach, with PEGSUS only being called once at the initialization stage. The background grid, covering both air and water, moves together with the floater. The computation time can be reduced with this approach.

The second approach is used while considering motions of all six DoFs. Only blocks wrapping the floating body are moved together with the body, with identical translational and angular speed with respect to the floater's center of gravity (CoG). The background mesh blocks remain fixed. Grid interpolation through PEGSUS is performed at every time step to model the changing translational displacement and tilting angle. The overset grid information is updated at every time step. The overset grid approach is utilized to accommodate the complex flow and relative motion between the floating body, wake, and background grid blocks.

The two approaches should be equivalent and will be verified by simulating the free-decay motion of the CALM buoy in surge direction. The verification is presented in Section 4.6. The first approach is used in the VIM simulations of semi-submersible platform in Chapter VI. Only surge and sway motion are considered for VIM and computation time can be saved with the first approach. The second approach is used by all simulations relating to CALM buoys, as detailed in Chapter V.

3.3 Interface between CFD and MOORING3D

Two coordinate systems are used to express the mooring configuration in MOORING3D and floater motion in the six-DoF motion solver, respectively. O'X'Y'Z' is a space-fixed coordinate system for mooring lines and is used in MOORING3D. Its origin locates at the still water surface and Y' axis directs positive upward. OXYZ is a space-fixed coordinate system for the floating structure and is used in the CFD module and the six-DoF motion solver, with origin at the still water surface and Z axis positive upward. O' and O are coincident. oxyz is a body-fixed coordinate system moving and rotating with the floater. At initial position, o is as well coincident with O' and O.
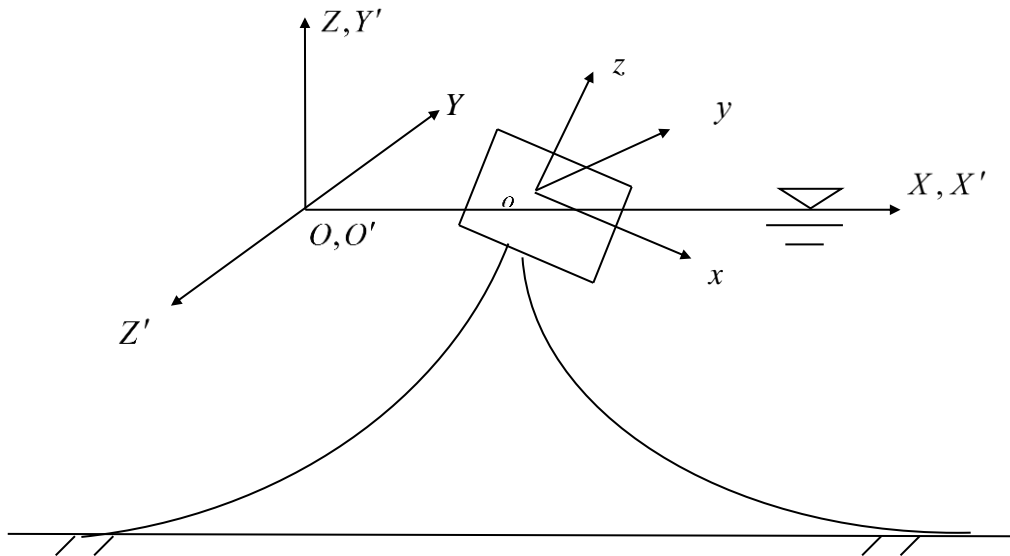
Figure 2. Coordinate system for structure and mooring system

A transfer matrix L between OXYZ and O'X'Y'Z' is introduced:

$$L = \begin{Bmatrix} 1 & 0 & 0 \\ 0 & 0 & -1 \\ 0 & 1 & 0 \end{Bmatrix} \qquad (3.8)$$

And the coordinates in O'X'Y'Z' can be transformed to coordinates in OXYZ system by applying the matrix L:

$$\begin{Bmatrix} X \\ Y \\ Z \end{Bmatrix} = L \begin{Bmatrix} X' \\ Y' \\ Z' \end{Bmatrix} \qquad (3.9)$$

In each time step, the FANS code updates the flow field in OXYZ system and the hydrodynamic loads on the floater, based on the updated floater position calculated from the last time step. The calculations in FANS code are performed in a dimensionless form, therefore the instantaneous floater coordinates, displacements, and hydrodynamic forces are all in dimensionless forms. However, the MOORING3D parameters are dimensional. Therefore, the dimensionless instantaneous floater position needs to be transferred to dimensional instantaneous locations of the fairleads, which are the input of the MOORING3D. Translational and rotational motions of a floating platform are required to determine the instantaneous positions of the fairleads.

The coordinates and time increment are dimensionalized before being calculating fairlead positions. For the displacement of buoy,

$$\boldsymbol{\xi} = \tilde{\boldsymbol{\xi}} * \lambda * charl \qquad (3.10)$$

$$\tau = \tilde{\tau} \frac{\sqrt{\lambda} * charl}{charu} \qquad (3.11)$$

where $\boldsymbol{\xi} = (\xi_1, \xi_2, \xi_3)^t$ is the dimensional translational displacement of the floater expressed in the space fixed coordinate system, and $\tilde{\boldsymbol{\xi}}$ is the dimensionless form of $\boldsymbol{\xi}$; τ is the dimensional time step used in MOORING3D, and $\tilde{\tau}$ is the dimensionless time step

used in FANS code; λ is the length scale ratio from full size to model scale; $charl$ and $charu$ are characteristic length and characteristic velocity used for normalization in FANS code.

The relationship between space-fixed dimensional coordinates $\hat{\boldsymbol{x}} = (\hat{x}, \hat{y}, \hat{z})^t$ and body-fixed dimensional coordinates $\boldsymbol{x} = (x, y, z)^t$ is as follows:

$$\hat{\boldsymbol{x}} = \boldsymbol{\xi} + \boldsymbol{T}^t \boldsymbol{x} \tag{3.12}$$

T is a transfer matrix between body-fixed coordinate system and the space-fixed coordinate system, superscript t represents transpose of a matrix.

$\boldsymbol{T} =$

$$\begin{bmatrix} \cos\alpha_3\cos\alpha_2 & \sin\alpha_3\cos\alpha_1 + \cos\alpha_3\sin\alpha_2\sin\alpha_1 & \sin\alpha_3\sin\alpha_1 - \cos\alpha_3\sin\alpha_2\cos\alpha_1 \\ -\sin\alpha_3\cos\alpha_2 & \cos\alpha_3\cos\alpha_1 - \sin\alpha_3\sin\alpha_2\sin\alpha_1 & \cos\alpha_3\sin\alpha_1 + \sin\alpha_3\sin\alpha_2\cos\alpha_1 \\ \sin\alpha_2 & -\cos\alpha_2\sin\alpha_1 & \cos\alpha_2\cos\alpha_1 \end{bmatrix}$$

T is an orthogonal matrix with the property that $T^t = T^{-1}$

$\boldsymbol{\alpha} = (\alpha_1, \alpha_2\ \alpha_3)^t$ are the Euler angles in the sequence of the roll-pitch-yaw motion.

Since the body-fixed coordinates of mooring line fairleads are known in advance, their instantaneous locations can be calculated using the above formulas at every time step. The MOORING3D updates the mooring configuration with the updated fairlead positions and returns with the full-scale dynamic forces and moments. Forces and moments applied on the hull are the overall tension from mooring lines and the moments induced by the mooring tension with respect to the CoG of the floater, and can be expressed as:

$$\mathbf{F}_c = \sum_{m=1}^{M}(\mathbf{LF}_m) \tag{3.13}$$

$$\mathbf{M}_c = \sum_{m=1}^{M}[\mathbf{r}_m \times (\mathbf{TLF}_m)] \tag{3.14}$$

32

where $\mathbf{F}_m$ refers to mooring force of the mth mooring line, which is expressed in the O'X'Y'Z' coordinate system, with the subscript m indicating mooring line number. M indicates the total number of mooring lines.

$\mathbf{F}_c$ refers to the coupling mooring forces expressed in the OXYZ coordinate system and is returned to the CFD module after transferring to dimensionless. $\mathbf{r}_m$ represents the coordinates of fairleads in the body fixed coordinate system oxyz, and $\mathbf{M}_c$ is the moment induced by $\mathbf{F}_m$. $\mathbf{M}_c$ is expressed in the body-fixed coordinate system oxyz.

Both $\mathbf{F}_c$ and $\mathbf{M}_c$ are to be transferred back to dimensionless before returning to FANS as feedback. For the overall dimensionless mooring forces and moments,

$$\widetilde{\mathbf{F}}_c = \frac{\mathbf{F}_c}{\rho * charl^2 * charu^2 * \lambda^3 * 1.025} \tag{3.15}$$

$$\widetilde{\mathbf{M}}_c = \frac{\mathbf{M}_c}{\rho * charl^3 * charu^2 * \lambda^4 * 1.025} \tag{3.16}$$

where $\widetilde{\mathbf{F}}_c$ and $\widetilde{\mathbf{M}}_c$ are dimensionless form of $\mathbf{F}_c$ and $\mathbf{M}_c$, and are used in the FANS code.

3.4 Six-DoF Motion Solver

The governing translational and rotational motion equations based on the Newton's Second Law are specified as:

$$\widetilde{m}\widehat{\boldsymbol{a}}_g = \widetilde{\mathbf{F}}_c + \widetilde{\mathbf{F}}_h \tag{3.17}$$

$$\widetilde{\mathbf{I}}_g \frac{d\boldsymbol{\omega}}{dt} + \boldsymbol{\omega} \times \widetilde{\mathbf{I}}_g \boldsymbol{\omega} = \widetilde{\mathbf{M}}_c + \widetilde{\mathbf{M}}_h \tag{3.18}$$

where $\widetilde{m}$ is dimensionless mass of the floater.

$\widetilde{\mathbf{I}}_g$ is dimensionless mass inertia with respect to the CoG, expressed in the body-fixed coordinate system oxyz.

33

$\widehat{\boldsymbol{a}}_g$ is dimensionless acceleration at the space-fixed coordinate system O'X'Y'Z'.

$\boldsymbol{\omega}$ is angular velocity at the body-fixed coordinate system oxyz.

The relationship between $\boldsymbol{\omega}$ and the derivatives of the Euler angles is given by:

$$\boldsymbol{\omega} = \mathbf{B}\frac{d\boldsymbol{\alpha}}{dt} \tag{3.19}$$

$$\mathbf{B} = \begin{bmatrix} \cos\alpha_3\cos\alpha_2 & \sin\alpha_3 & 0 \\ -\sin\alpha_3\cos\alpha_2 & \cos\alpha_3 & 0 \\ \sin\alpha_2 & 0 & 1 \end{bmatrix} \tag{3.20}$$

where $\boldsymbol{\alpha}=(\alpha_1, \alpha_2, \alpha_3)^t$ are the Euler angles in the roll-pitch-yaw sequence.

The relationship between $\frac{d\boldsymbol{\omega}}{dt}$ and the second derivatives of the Euler angles is given

by:

$$\frac{d\boldsymbol{\omega}}{dt} = \mathbf{B}\frac{d^2\boldsymbol{\alpha}}{dt^2} + \boldsymbol{\alpha}_q \tag{3.21}$$

where

$$\boldsymbol{\alpha}_q = \mathbf{Q}\frac{d\boldsymbol{\alpha}}{dt} = \begin{bmatrix} -\cos\alpha_3\sin\alpha_2\alpha_{2t} - \sin\alpha_3\cos\alpha_2\alpha_{3t} & \cos\alpha_3\alpha_{3t} & 0 \\ \sin\alpha_3\sin\alpha_2\alpha_{2t} - \cos\alpha_3\cos\alpha_2\alpha_{3t} & -\sin\alpha_3\alpha_{3t} & 0 \\ \cos\alpha_2\alpha_{2t} & 0 & 1 \end{bmatrix}\begin{pmatrix} \alpha_{1t} \\ \alpha_{2t} \\ \alpha_{3t} \end{pmatrix}$$

By implementing the expressions for $\boldsymbol{\omega}$ and $\frac{d\boldsymbol{\omega}}{dt}$ into rotational motion equation, the

roll-pitch-yaw sequence defined by the Euler angles is obtained.

The 4th order Runge-Kutta method is used to calculate acceleration, velocity, and displacement of the floater, in both translational and rotational aspects. The detailed numerical scheme is elaborated as follows:

$$(\widetilde{\mathbf{F}}_{c_{n1}}, \widetilde{\mathbf{M}}_{c_{n1}}, \mathbf{r}_n) = \text{MOORING3D}(\widetilde{t}_n, \widetilde{v}_n, \widetilde{x}_n, \mathbf{r}_{n-1}, CP) \tag{3.22}$$

$$\widetilde{v_1} = \widetilde{\tau}\widetilde{\mathbf{a}} \text{ where } \widetilde{\mathbf{a}} = motion\_solver(\widetilde{\mathbf{F}}_{c_{n1}}, \widetilde{\mathbf{M}}_{c_{n1}}, \widetilde{\mathbf{F}}_{h_n}, \widetilde{\mathbf{M}}_{h_n}) \tag{3.23}$$

$$\widetilde{x_1} = \widetilde{v_n}\tilde{\tau} + \frac{1}{2}\widetilde{v_1}\tilde{\tau} \tag{3.24}$$

$$\left(\widetilde{\mathbf{F}}_{c_{n2}}, \widetilde{\mathbf{M}}_{c_{n2}}, \mathbf{r}_n\right) = \text{MOORING3}D\left(\tilde{t}_n + \frac{\tilde{\tau}}{2}, \widetilde{v_n} + \frac{\widetilde{v_1}}{2}, \widetilde{x_n} + \frac{\widetilde{x_1}}{2}, \mathbf{r}_n, CP\right) \tag{3.25}$$

$$\widetilde{v_2} = \tilde{\tau}\tilde{\mathbf{a}} \text{ where } \tilde{\mathbf{a}} = motion\_solver\left(\widetilde{\mathbf{F}}_{c_{n2}}, \widetilde{\mathbf{M}}_{c_{n2}}, \widetilde{\mathbf{F}}_{h_n}, \widetilde{\mathbf{M}}_{h_n}\right) \tag{3.26}$$

$$\widetilde{x_2} = \widetilde{v_n}\tilde{\tau} + \frac{1}{2}\widetilde{v_2}\tilde{\tau} \tag{3.27}$$

$$\left(\widetilde{\mathbf{F}}_{c_{n3}}, \widetilde{\mathbf{M}}_{c_{n3}}, \mathbf{r}_n\right) = \text{MOORING3}D\left(\tilde{t}_n + \frac{\tilde{\tau}}{2}, \widetilde{v_n} + \frac{\widetilde{v_2}}{2}, \widetilde{x_n} + \frac{\widetilde{x_2}}{2}, \mathbf{r}_n, CP\right) \tag{3.28}$$

$$\widetilde{v_3} = \tilde{\tau}\tilde{\mathbf{a}} \text{ where } \tilde{\mathbf{a}} = motion\_solver\left(\widetilde{\mathbf{F}}_{c_{n3}}, \widetilde{\mathbf{M}}_{c_{n3}}, \widetilde{\mathbf{F}}_{h_n}, \widetilde{\mathbf{M}}_{h_n}\right) \tag{3.29}$$

$$\widetilde{x_3} = \widetilde{v_n}\tilde{\tau} + \frac{1}{2}\widetilde{v_3}\tilde{\tau} \tag{3.30}$$

$$\left(\widetilde{\mathbf{F}}_{c_{n4}}, \widetilde{\mathbf{M}}_{c_{n4}}, \mathbf{r}_n\right) = \text{MOORING3}D(\tilde{t}_n + \tilde{\tau}, \widetilde{v_n} + \widetilde{v_3}, \widetilde{x_n} + \widetilde{x_3}, \mathbf{r}_n, CP) \tag{3.31}$$

$$\widetilde{v_4} = \tilde{\tau}\tilde{\mathbf{a}} \text{ where } \tilde{\mathbf{a}} = motion\_solver\left(\widetilde{\mathbf{F}}_{c_{n4}}, \widetilde{\mathbf{M}}_{c_{n4}}, \widetilde{\mathbf{F}}_{h_n}, \widetilde{\mathbf{M}}_{h_n}\right) \tag{3.32}$$

$$\widetilde{x_4} = \widetilde{v_n}\tilde{\tau} + \frac{1}{2}\widetilde{v_4}\tilde{\tau} \tag{3.33}$$

$$\widetilde{v_{n+1}} = \widetilde{v_n} + \frac{1}{6}\left(\widetilde{v_1} + 2\widetilde{v_2} + 2\widetilde{v_3} + \widetilde{v_4}\right) \tag{3.34}$$

$$\widetilde{x_{n+1}} = \widetilde{x_n} + \frac{1}{6}\left(\widetilde{x_1} + 2\widetilde{x_1} + 2\widetilde{x_3} + \widetilde{x_4}\right) \tag{3.35}$$

$$\widetilde{t_{n+1}} = \tilde{t}_n + \tilde{\tau} \tag{3.36}$$

$$\widetilde{X_{n+1}} = \text{PEGSUS}(\widetilde{x_{n+1}}); \left(\widetilde{\mathbf{F}}_{h_{n+1}}, \widetilde{\mathbf{M}}_{h_{n+1}}\right) = \text{CFD}(\widetilde{X_{n+1}}) \tag{3.37}$$

$\tilde{\tau}$ is the dimensionless time step.

$\tilde{\mathbf{a}}$ is the acceleration calculated at each of four internal stages.

$\widetilde{v_1}$, $\widetilde{v_2}$, $\widetilde{v_3}$, $\widetilde{v_4}$ are all six-DoF vectors and mean estimated dimensionless translational and angular velocity increment of four internal stages.

35

$\widetilde{x_1}$, $\widetilde{x_2}$, $\widetilde{x_3}$, $\widetilde{x_4}$ are all six-DoF vectors and mean displacement increment of four internal stages.

$\widetilde{\boldsymbol{v}}_n$ refers to dimensionless translational and angular velocity.

$\widetilde{\boldsymbol{x}}_n$ refers to dimensionless translational and angular displacement.

$\mathbf{r}_n$ is the vector describing the configuration of mooring lines specified in Section 3.2.

CP is a control parameter telling which internal stage it is.

$\widetilde{\mathbf{F}}_{c_{n1}}$ and $\widetilde{\mathbf{M}}_{c_{n1}}$ are dimensionless mooring tension and moment, and 1 refers to the first internal stage of the RK method. $\widetilde{\mathbf{F}}_{c_{n2}}$ and $\widetilde{\mathbf{M}}_{c_{n2}}$, $\widetilde{\mathbf{F}}_{c_{n3}}$ and $\widetilde{\mathbf{M}}_{c_{n3}}$, $\widetilde{\mathbf{F}}_{c_{n4}}$ and $\widetilde{\mathbf{M}}_{c_{n4}}$ refer to the mooring loads at the second, third, and forth internal stage, respectively.

$\widetilde{\mathbf{F}}_{h_n}$ and $\widetilde{\mathbf{M}}_{h_n}$ are the dimensionless hydrodynamic loads calculated by FANS code, and $\widetilde{X_n}$ is the mesh system used by CFD.

$\widetilde{t_n}$ is the dimensionless time.

The subscript n of all parameters means the time step number.

The function motion_solver() is used to evaluate the translational and rotational accelerations through the motion equations of Eq. (3.17) and (3.18). The calculated acceleration $\tilde{\mathbf{a}}$ is used at each internal stage for the calculation of velocity increment ($\widetilde{\boldsymbol{v}_1}$, $\widetilde{\boldsymbol{v}_2}$, $\widetilde{\boldsymbol{v}_3}$, $\widetilde{\boldsymbol{v}_4}$) and displacement increment ($\widetilde{x_1}$, $\widetilde{x_2}$, $\widetilde{x_3}$, $\widetilde{x_4}$).

MOORING3D module is called for four times within each time step. The input of MOORING3D include the dimensionless displacement and velocity in all six DoFs and a

36

control parameter specifying the internal stage of Runge-Kutta method. How MOORING3D works is illustrated as follows:

1. At first, within MOORING3D, the estimated dimensionless displacement and velocity is transferred to dimensional form. Then the instantaneous positions of all fairleads are obtained through Eq. (3.12)

2. The CP determines whether the factor of 0.5 is applied to the time step, velocity increment, and displacement increment.

    a. The predicted velocity and displacement from calculation of last time step is used at the first internal stage (Eq. 3.22),

    b. Half increment and half of time step are used for prediction at the second and third internal stage (Eq. 3.25 and Eq. 3.28),

    c. The whole of time step and increment are used at the fourth internal stage (Eq. 3.31).

3. The MOORING3D updates the mooring configuration and calculates the mooring loads of each line. The overall mooring tension and moment in the global coordinate system is obtained by Eq. 3.13 and Eq. 3.14. The loads are then transferred to dimensionless form $\widetilde{\mathbf{F}}_c$ and $\widetilde{\mathbf{M}}_c$ by Eq. 3.15 and Eq. 3.16.

4. The CP also determines whether the mooring configuration needs to be reset to input values. The mooring configuration needs to be reset to $\mathbf{r}_n$ at the 2nd, 3rd, and 4th time of calling MOORING3D, for the evaluation of dynamic tension and moment of the next step. The mooring configuration is updated from

37

$\mathbf{r}_{n-1}$ to $\mathbf{r}_n$ only at the 1st internal stage, meaning the mooring calculation is proceeded from last time step to the current time step.

The hydrodynamic loads $\widetilde{\mathbf{F}_h}$ and $\widetilde{\mathbf{M}}_h$ are estimated one time at each time step, as is specified in Equation 3.37. This is due to considerably increasing computing costs if meshes are adjusted and hydrodynamic loads are calculated for all four internal stages within one time step. The mooring loads $\widetilde{\mathbf{F}_c}$ and $\widetilde{\mathbf{M}}_c$ are estimated four times within one time step based on Equations 3.22, 3.25, 3.28, and 3.31.

After $\widetilde{\boldsymbol{x}_{n+1}}$ is calculated, it is applied to computational blocks to update floater position. The program PEGSUS (Suhs and Tramel, 1991) is used to move blocks wrapping the floating body to achieve six-DoF simulations. The interpolation information for linking grids is updated without tedious grid regeneration, following the approaches discussed in Section 3.2.1. Then the CFD module updates the flow field and calculates new hydrodynamic loads $\widetilde{\mathbf{F}_h}_{n+1}$ and $\widetilde{\mathbf{M}}_{h_{n+1}}$ through pressure and shear force integration over the instantaneous wetted surface. The simulation proceeds to the next time step. The precision of Runge-Kutta method is improved to achieve a more robust coupling between the MOORING3D, motion solver, and FANS CFD module.

3.5 Summary

In this dissertation, all six DoFs of motion in waves and currents can be calculated. The level-set method based on the 3rd order TVD scheme and the 3rd order ENO scheme is applied to capture the air-water interface for the simulation of free surface effects and

incoming waves. Grid interpolation through the overset grid method is performed at every

time step to update the grids to accommodate the floater's changing position and tilting

angle. Additionally, the MOORING3D program is further developed with the capacity to

model a mooring system with large elongation elements and multiple element types and

to adapt to the motion solver.
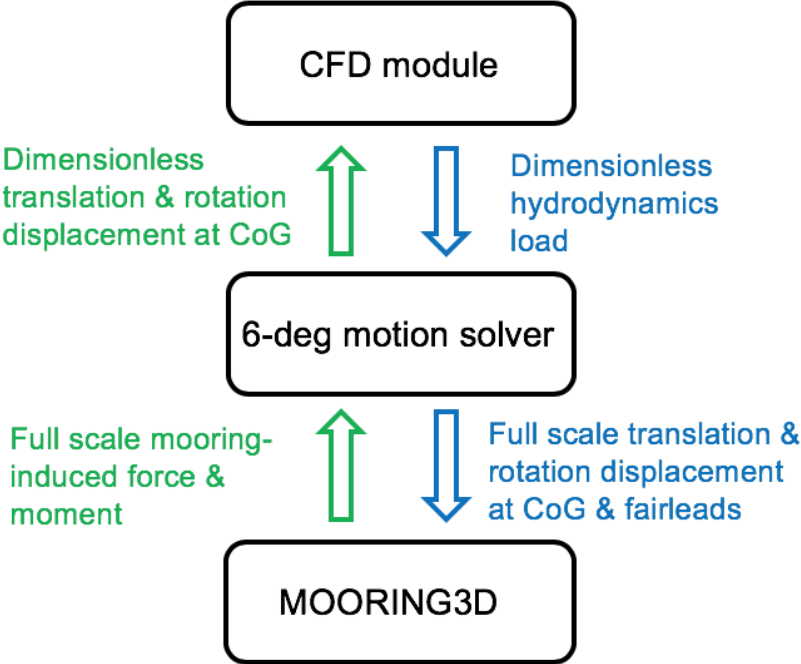
Figure 3. Integration of CFD module, motion solver and MOORING3D

Figure 3 shows the visual interactive coupling procedures and data transfer

between the CFD, motion solver, and MOORING3D modules. To be simplified, the CFD

code updates the flow field and the dimensionless hydrodynamic forces and moments ($\widetilde{\mathbf{F}_h}$

and $\widetilde{\mathbf{M}_h}$) in each time step. The updated floater position is transmitted to the motion solver

and the MOORING3D. The MOORING3D updates the full-scale mooring configuration

and returns with updated full-scale dynamic tension and moment. The updated overall mooring tension and moment are then transferred back to dimensionless form ($\widetilde{\mathbf{F}}_c$ and $\widetilde{\mathbf{M}}_c$) and are returned to the motion solver. The motion is calculated by the motion solver considering mooring and hydrodynamic loads. The acceleration, velocity and displacement are calculated by 4th order Runge-Kutta method. The simulation proceeds to the next time step after the floater position is updated.

CHAPTER IV

VERIFICATION AND VALIDATION

4.1 Introduction

This chapter describes program verification and validation by modeling the CALM buoy with its mooring system. Two calm buoys are selected for study. The first CALM buoy was used in the model tests of Bunnik et al. (2002) and numerical simulations of Song et al. (2014). The second CALM buoy was used in the experiments and numerical simulations of Ryu et al. (2006). A slack chain mooring system and a taut truncated mooring system are used for the two CALM buoys, respectively. At first, this chapter presents the model description for the CALM boy. The verification of two mooring systems modeled by the MOORING3D is also presented. Also, this chapter presents the verification of numerical methods of level-set method, overset grid method, and coupling between the CFD and the mooring program.

4.2 Model Description of CALM Buoys

Two CALM buoys are selected for model verification and validation with their basic information presented in Table 1. Buoy #1 is the buoy with a slack chain mooring system, and Buoy #2 is the buoy with a truncated mooring system. Both the coupled CFD-mooring analysis and AQWA-Orcaflex analysis are performed for Buoy#1 for verification and validation. The advantages and disadvantages of the two methods are to be discussed.

The coupled CFD-mooring analysis for Buoy#2 are performed for comparison with model tests.

The critical parameters of the prototype CALM buoys are specified in Table 2. The CFD models are created at model scale. The scale ratios of the two CALM buoys are 20 and 35.6, respectively.

Table 1. CALM buoy information summary

Buoy #	Mooring System	Available Experimental Data	Previous Simulation	Simulation to be performed
1	9-point chain system	Load RAOs of Bunnik et al. (2002)	Song et al. (2014)	AQWA-Orcaflex; CFD-Mooring analysis
2	4-point truncated mooring system	Motion RAOs of Ryu et al. (2006)	Ryu et al. (2006)	CFD-Mooring analysis

Table 2. Parameters for the CALM buoy model

Parameter	Unit	Buoy #1	Buoy #2
Model test scale	N.A.	20	35.6
Water depth	m	500	106.8
Buoy hull diameter	m	20	17.0
Buoy mass in air	ton	1299	878.6
KG	m	5.1	3.4
Buoy total Rxx	m	5.18	4.39
Buoy total Ryy	m	5.18	4.39

The grid structure around the buoy and the overset grid system is demonstrated in Figure. 4 (a). The grid parameters are normalized by the outer diameter of the buoy. The

buoy hull diameter is used as the characteristic length for full scale, and the model-scale

characteristics length is obtained by dividing the full scale one with the scale ratio, as is

shown in Table 3. To achieve Froude scaling, the characteristics velocity V is determined

as square roots of the product of characteristic length and gravity acceleration. the

characteristics time T is obtained by dividing D with V. Since mooring system is in full-

scale, full-scale characteristic parameters are used while nondimensionalizing the full-

scale mooring loads.

(a) Grids around buoy, side view   (b) Grids around buoy, top view
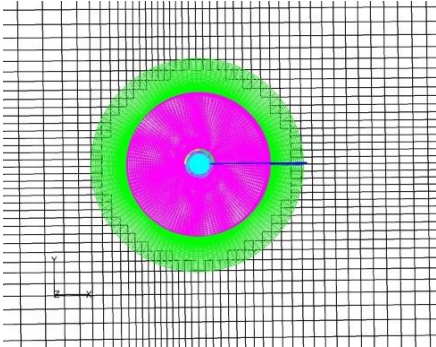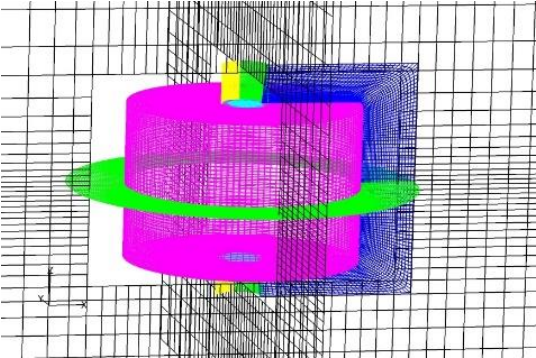
(c) Computational domain
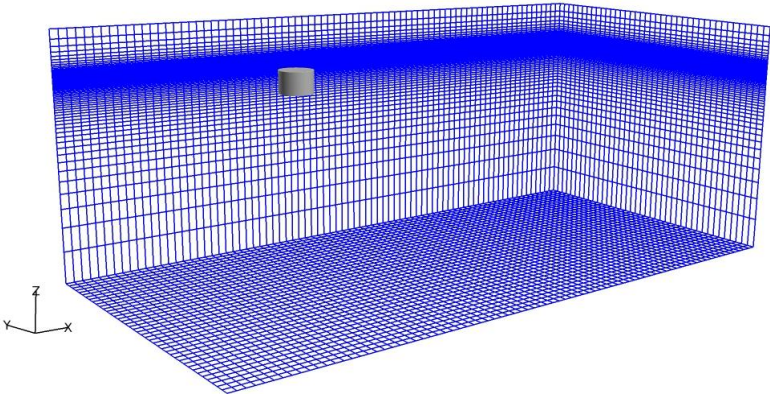
Figure. 4 Grids around the buoy and the computational domain

43

The characteristic parameters for both model and prototype scales of the two CALM buoys are summarized in Table 3. The non-dimensional hydrostatic pressure is equal to the non-dimensional depth after Froude scaling with this estimation. The nondimensional OD is 1 for both Buoy #1 and Buoy #2. The draft is subjected to both buoy self-weight and vertical mooring forces and is adjusted automatically in the CFD module.

Table 3. Summary of characteristic length, velocity, and time for Froude scaling

Buoy	Scale	Characteristic length D (m)	Characteristic velocity V (m/s)	Characteristic time T (s)
Buoy #1	Prototype	20	$\sqrt{20 \times 9.8}$	1.429
	Model	20/20	$\sqrt{20/20 \times 9.8}$	0.319
Buoy #2	Prototype	17	$\sqrt{17 \times 9.8}$	1.317
	Model	17/35.6	$\sqrt{17/35.6 \times 9.8}$	0.221

The overset grid approach by Suhs and Tramel (1991) is used to best describe the motion of each subdomain of the fluid. Information among adjacent subdomains is transferred by overlapped common regions between both borders with the overset grid method. The buoy is surrounded by three adjacent grid blocks, which include one primary boundary-fitted grid block wrapping the buoy with the dimensions of 122×31×129 and another two small blocks with the dimensions of 31×31×31 at the buoy top and the bottom respectively. The magenta grid surface, green grid surface, and the blue grid surface

44

represent grids in the three cutting surfaces of the main block, as can be seen from Figure. 4 (a) and (b). The small block at the top of the buoy fills the holes surrounded by the main block, with the light blue grid surface that fits the buoy top surface and small yellow and green grid surfaces that allow the information transfer with the main block. The bottom small block has the same configuration as the one at the top. In total, 547,460 grid points in three blocks are used for the buoy's adjacent area. How three blocks around the buoy interact and exchange information with the background blocks through overset grids is displayed in Figure. 4 (a) and (b), which show from side view and top view, respectively.

The near wall spacing is consistent with the study conducted by Gu et al. (2019) and is set as $10^{-3}D$ for the model-scale buoy with resultant y^+ within the viscous sublayer. Gu et al. (2019) performed the mesh sensitivity study of the CALM buoy of the same size in currents, and it proved that the simulation with the near wall mesh spacing of $10^{-3}D$ is convergent. The flow separation is captured, and the viscous effects are estimated reasonably with the use of LES in the study of Gu et al. (2019). Chen et al. (2016) proved that the use of LES with y^+ around 2-3 yields convergent results for the vortex-induced motion simulation, which are validated against experiments. Therefore, the mesh density is sufficient and the use of LES is suitable in the model-scale CALM buoy simulation.

The simulation domain is -5≤x/D≤15, -5≤y/D≤5, and -6.28235≤z/D≤1.25647, as shown in Figure. 4 (c). A rectangular fixed block is designed to resolve the liquid and airflow fields in the background besides the three blocks around the buoy, and it stays stationary throughout the simulations. The block fills the entire simulation domain and

solves the fluid in the far-field. Another refined block with the range of -1.5≤x/D≤8.5, -1.5≤y/D≤1.5, and -1.00518≤z/D≤1.25647 is designed to resolve the flow field around the buoy. Grid sizes in x- and y-directions increase considerably for the far-field ocean. These two stationary background blocks add another 332,100 grid points. Overall, the system has about 0.9 million grid points in 5 blocks.

only the three blocks adjacent to the buoy shown in Figure. 4 (a) are moved together with the buoy to achieve the six-DoF motion simulation, with identical translational and angular speed with respect to the buoy's CoG. The two background mesh blocks remain fixed. The overset grid method proposed by Suhs and Tramel (1991) is applied to obtain the updated oversetting grid information. The CFD module calculates the flow field based on the updated grids in the next time step. Besides, Neumann conditions for velocity components and linear extrapolation for pressure are used on the outlet boundary. Far-field conditions are used for the other boundaries of the simulation domain.

The wall clock time for each time step of computation is about 10 seconds on a single processor. The time step is selected as 0.02 dimensionless time, which is equivalent to 0.02633 s for the prototype simulation and 0.0044 s for the model scale simulation. A calculation of 6,000 steps over the 900,000-mesh system takes about 16 hours, faster than EXPRO-CFD system which took one day for simulation of 4000 time steps over the 200,000-mesh system. The simulation time could be further reduced significantly with the use of parallel computing over multiple processors.

4.3 Skirt Effect Corrections

4.3.1 Buoy #1

Buoy #1 used by Bunnik et al. (2002) had a skirt. However, the detailed size information of the skit is not available. In accordance with Bunnik et al. (2002), the surge and heave wave forces are far less influenced by the skirt and can be well predicted by a linear diffraction model. The wave-exciting pitch moments on the buoy are affected by the presence of the skirt which induces viscous forces. However, the viscous effects are limited comparing to buoy hull due to its much smaller cross-sectional area. Song et al. (2014) excluded the skirt in the AQWA diffraction analysis. Both Bunnik et al. (2002) and Song et al. (2014) provided limited information on added mass and damping induced by the skirt. Therefore, the skirt is omitted in both the CFD and AQWA model in this dissertation. However, due to skirt's influences on pitch direction, the correction of viscous force is considered by a simplified approach in both the coupled CFD-mooring analysis and the AQWA-Orcaflex simulation. The viscous moment is simplified as a linear damping term.

4.3.2 Buoy #2

In terms of Buoy #2, the buoy model adopted by Ryu et al. (2006) also had a skirt. The skirt has various holes, and the detailed dimensions of holes and the skirt thickness are not available. The skirt was also omitted from the CFD model in the study of Gu et al. (2019). Ryu et al. (2006) conducted numerical simulations for the buoy with and without the skirt based on diffraction theory. The simulated results indicated that skirt effects on

RAO are limited and that excluding the skirt effects does not jeopardize the comparison with model tests. For instance, the difference between simulated heave RAO with and without the skirt showed a difference of at most 8%. The simulation results without the skirt agree well with experimental results, and in certain periods, appear even closer to the experiments than the simulations with the skirt.

The skirt effects are considered with a more detailed approach for Buoy#2 to achieve a more straightforward comparison with model tests. Though the skirt is not directly modeled in the CFD due to lack of dimension details, the extra added mass induced by the skirt is given by Ryu et al. (2005). The skirt added mass varies with motion period and is approximately 5×10^5 kg for heave and 1.8×10^7 $kg \cdot m^2$ for pitch, respectively. The skirt added mass is directly considered in the six-DoF motion solver. Combining with the buoy's added mass calculated by CFD, a more accurate representation of overall added mass for heave and pitch is achieved. Additionally, the skirt-induced viscous damping loads are calculated in the motion solver. The viscous force and moment are given by Cozijn et al. (2005):

$$FZ(t) = -\frac{1}{2} \cdot \rho \cdot C_D \cdot \frac{A_S}{2\pi} \cdot \int_0^{2\pi} V(t, \alpha) \cdot |V(t, \alpha)| \cdot d\alpha$$

$$MY(t) = \frac{1}{2} \cdot \rho \cdot C_D \cdot \frac{A_S}{2\pi} \cdot R_S \int_0^{2\pi} \cos(\alpha) \cdot V(t, \alpha) \cdot |V(t, \alpha)| \cdot d\alpha$$

where FZ and MY are drag forces and moments, C_D is the drag coefficient, A_S is the skirt circular area, and R_S is the skirt radius. The drag force and moment vary with time and vertical velocity V. The angle α defines the tangential position around the skirt

circumference. The skirt added mass and damping is considered in the heave and pitch directions accordingly in the coupled analysis.

It is also worthwhile to investigate how the skirt influences the buoy's wave-induced motion through the coupled analysis. Sensitivity studies of simulations without the skirt are also conducted. The skirt-free simulations are compared to those with the skirt. The comparison indicate that the skirt had limited influence on the buoy's wave-induced responses for the selected wave periods. The details are discussed in Chapter V.

4.4 Mooring3D Verification

This section describes the CALM buoys' mooring systems that are modeled by the MOORING3D. The slack chain mooring system is used with the CALM buoy modeled by Bunnik et al. (2002) and Song et al. (2014). The taut truncated mooring system is used in the model tests of CALM buoy by Ryu et al. (2006). The same mooring models are created in the commercial software Orcaflex and compared with the MOORING3D for its verification.

4.4.1 Slack Chain Mooring System of Buoy #1

The model tests of Buoy #1 were performed by Bunnik et al. (2002) with available measurement data of wave exciting forces. However, the detailed mooring properties and configuration were not available. Song et al. (2014) selected the same buoy and designed multiple mooring system for the buoy to study the buoy responses in waves by using both diffraction analysis and hybrid wave model (HMW). Song et al. (2014) used AQWA for

diffraction analysis of the buoy. The hydrodynamic output of AQWA is regarded as the input of Orcaflex. The buoy is treated as a rigid body in Orcaflex with full-scale mooring system being modeled to attain a time-domain coupled analysis.

Table 4. Summary of mooring line properties of slack chain mooring system

Parameter	Unit	Value
Length	m	2144
Wet weight	kg/m	98.7
EA	kN	413700
Pretension	kN	1062.6
Fairlead angle	degree	40.5
Added mass coefficient	N.A.	1.0
Drag coefficient	N.A.	1.2

The designed mooring systems by Song et al. (2014) included a 9-point slack-chain mooring system, which is replicated in this study by the MOORING3D. The simulated water depth is 500 meters. The nine mooring lines are divided into three bundle groups, each of which has azimuths of 60, 180, and 300 degrees with respect to the buoy's x-axis, and each line is separated by 5 degrees in each bundle. The R4 chain has a diameter of 2.5 inches. The length of each mooring line is about 7,032 ft (2,144 m), with the estimated MBL of 796 kips (4,300 KN). The configuration of the slack chain mooring system is shown in Figure. 6. The pretension at the top of individual line is about 1062.6 kN. The equivalent model in Orcaflex generates the top tension of around 1065 kN, with difference of less than 0.3% to the MOORING3D result.

Mooring stiffness curves in surge, sway, and heave directions are formed by applying consecutive displacements to the buoy in both programs. Figure. 5 reveals that the mooring stiffness curves generated in the MOORING3D program in three directions almost overlap with those calculated in Orcaflex. There is a minor discrepancy between the two stiffness curves in surge and sway directions when offset is large.
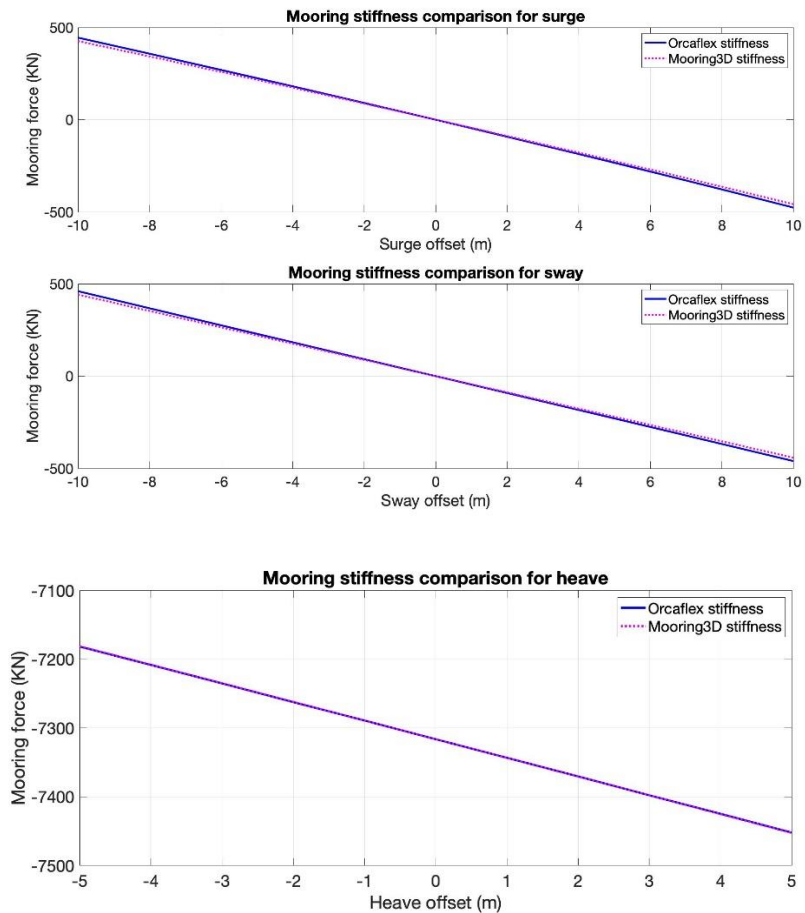

Figure. 5 Mooring stiffness comparison of slack chain system

The added mass coefficient is taken as 1.0, as shown in Table 5. The drag coefficient is taken as 1.2, properly modeling the drag loads applied on mooring lines. The overall weight of one individual mooring line is about 211.6 ton, which is almost 16% of

the buoy mass. The line dynamic effects are significant for the buoy's motion in this case and properly modeled by the coupled analysis.
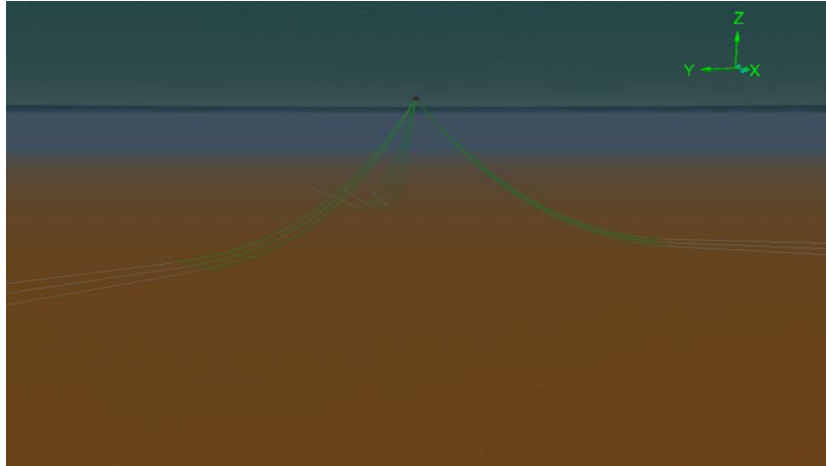
Figure. 6 Snapshot of the 9-point slack-chain mooring system

4.4.2 Taut Truncated Mooring System of Buoy #2

Ryu et al. (2006) used the truncated mooring method for the CALM buoy model test due to the limitations of experimental water depth. Gu et al. (2017) used catenary cables to provide similar hydrodynamic performance as the CALM buoy. In this study, the taut mooring system with parameters identical to model tests is modeled by using large elongation elements to attain a thorough replication of model tests.

The mooring system configuration is designed to have the stiffness characteristics and pretension of a mooring system of 1000-meter water depth. The truncated mooring system includes 4 legs spaced 90° apart, with fairlead declination angles of 45°. The pretension is designed to provide the net mooring load on the buoy. The full-scale parameters of the mooring lines adopted in the model test are presented in Table 5. The

MOORING3D program is used to model the mooring system. Simultaneously, the model is also created in Orcaflex. Top tension obtained from MOORING3D equals approximately 14,700 kN and the difference with pretension of 150 metric tons in model tests is within 0.1%. The comparison validated the MOORING3D FEM model with the use of large elongation elements.

Table 5. Summary of mooring line properties of truncated mooring system

Parameter	Unit	Value
Length	m	133.3
Wet weight	kg/m	3
EA	Metric tons	1963
Pretension	Metric tons	150
Fairlead angle	degree	45
Added mass	N.A.	1.0
Drag coefficient	N.A.	1.2

Mooring stiffness curves in surge, sway, and heave directions are formed by applying consecutive displacements to the buoy in both programs. Figure. 7 reveals that the mooring stiffness curves generated in the MOORING3D program in three directions almost overlap with those calculated in Orcaflex. The mooring stiffness in two horizontal directions is 165.86 kN/m. The mooring stiffness in the vertical direction is 373.79 kN/m, higher than that in surge and sway. Because the fairlead positions and mooring line declination angles are also consistent with model tests, the simulated rotational stiffness for roll, pitch, and yaw are justified to be equivalent to model tests.
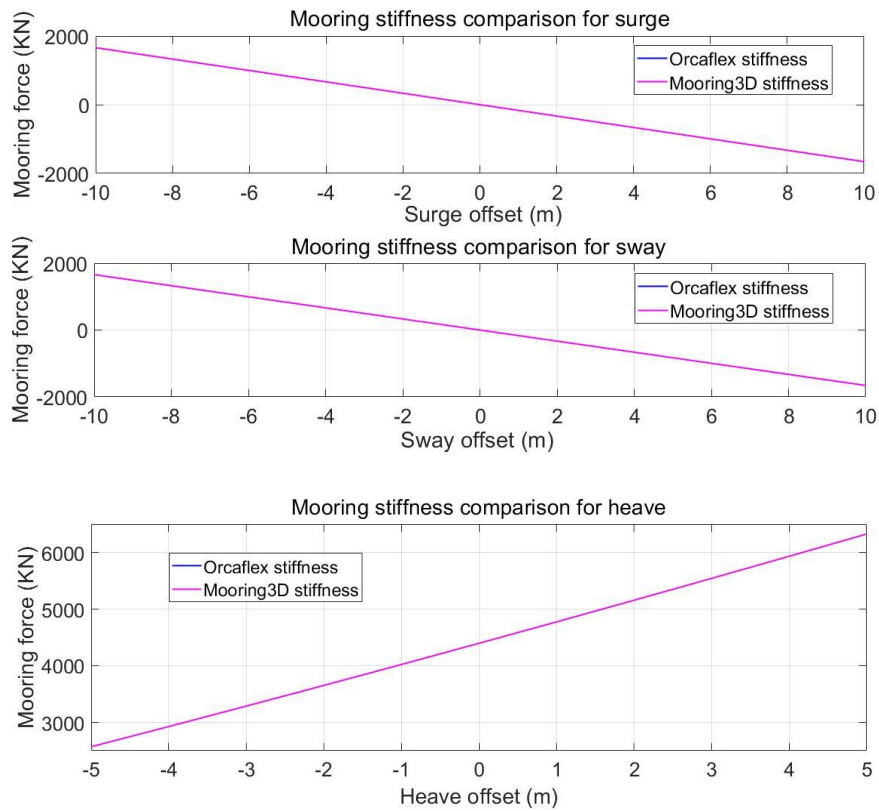
Figure. 7 Mooring stiffness comparison of truncated mooring system

Figure. 8 displays the truncated mooring system configuration. The truncated mooring system in the experiment is replicated by modeling it with large elongation elements. The line elongation is modeled properly. The overall wet weight of the mooring line is about 1.6 ton. Though it is small compared to buoy's mass, the inertial effects of lines are still considered in the dynamic mooring analysis. Both inertial effects and damping effects induced by the mooring system are captured. The thorough replication of mooring system allows the experimental comparison of simulated free-decay and wave-induced responses.
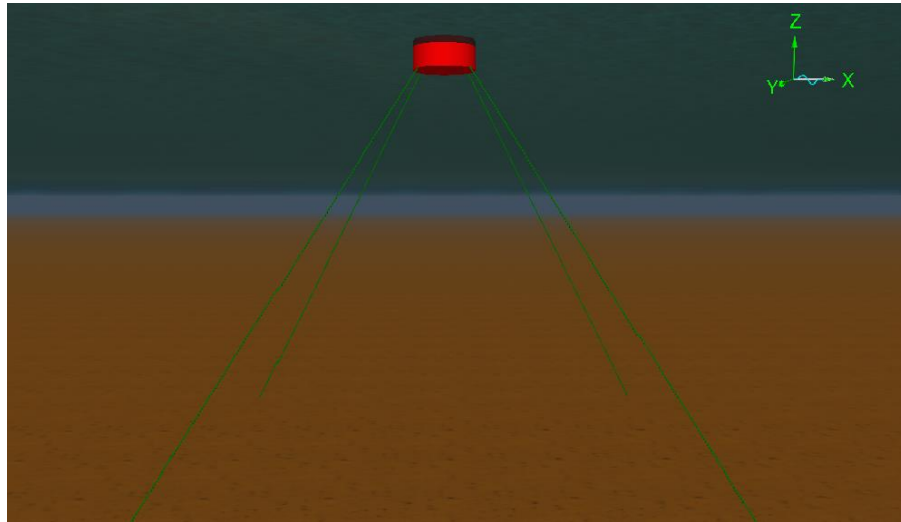
Figure. 8 Snapshot of the 4-point taut truncated mooring system

4.5 Verification of Three-dimensional 3rd Order ENO Scheme

The 3rd order ENO scheme for level-set method is extended from two-dimensional to three-dimensional. The three-dimensional 2nd order ENO scheme was introduced by Yu (2007) for green water and sloshing simulation and was validated against experiments. The waves with periods of 8.5 seconds and 9.2 seconds are generated by applying the associated wavemaker boundary conditions. Both the 2nd order and the 3rd order ENO scheme are applied.

A numerical wave elevation probe is placed beside the buoy near the edge of the computational domain in the wavemaker's downstream direction. The distance from the probe to the wavemaker is the same as the distance from the buoy's center to the wavemaker, therefore the undisrupted instantaneous wave elevation measured at the probe equals the incident waves at the buoy. The wave elevation is extracted at the air-water interface where the level-set value equals zero at the probe location.

The level-set values are initialized within the simulation domain. The surface at z/L=0 is initialized as the initial air-water interface. The pressure is also initialized as the dimensionless hydrostatic pressure. The level-set values below the interface are positive, representing the underwater region, and the level-set values above the interface are negative, representing the air. In terms of the underwater region, the wavemaker boundary condition with prescribed particle velocities induced by the wavemaker is applied to the leftmost plane. Various wave sequences are generated with wave periods of more than 7 seconds at full scale. For the shortest wave, one wavelength is represented by more than 70 mesh points.

Figure. 9 shows the wave elevation time histories at the wave probe obtained by 2nd and 3rd order ENO scheme. The two time histories overlap with each other, indicating the reliability of 3rd order ENO scheme. The extended three-dimensional 3rd order ENO scheme will be applied in the forthcoming simulations.
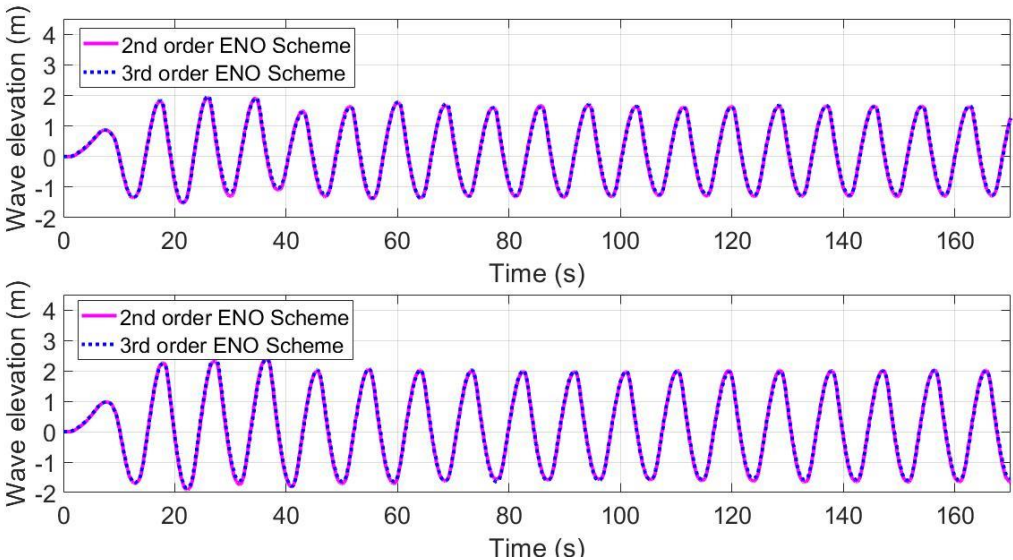
Figure. 9 Comparison of 2nd order and 3rd order ENO scheme

Figure. 10 (a) and (b) display the air-water interface of a test simulation case when waves with a period of 8.5 seconds are generated with the corresponding boundary conditions, with (a) showing the wave crest and (b) showing the wave trough. Te buoy is fixed in the test cases. The wave sequence appears reasonable. The level-set method not only reasonably models waves, but also captures the wave surface run-up in the front side of the buoy, as is shown in Figure. 10 (a).

(a) Wave crest and wave run-up
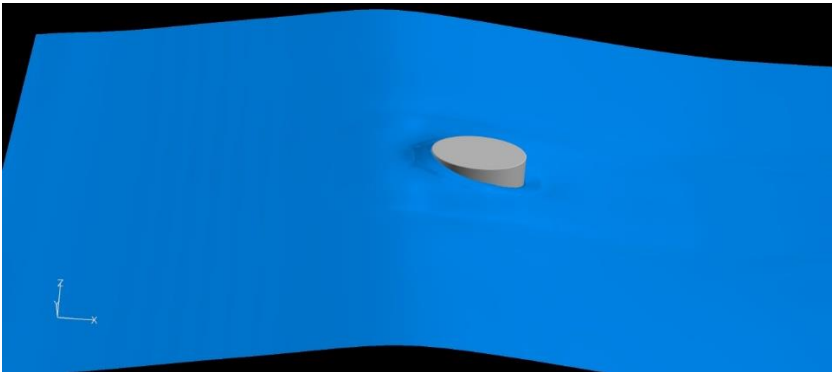
(b) Wave trough
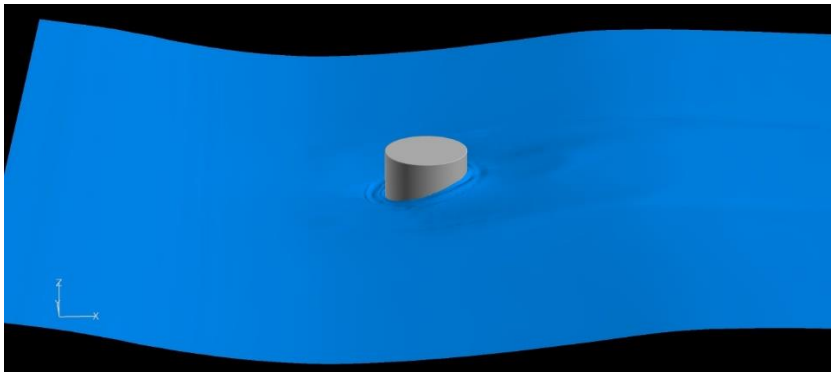
Figure. 10 Three-dimensional wave surfaces

If wave amplitude is enlarged, a test case of green water can be conducted, with green water would be observed at the top of the buoy. Figure. 11 shows the evolution of green water on the buoy top as a wave passes. The green water test case demonstrates that the level-set method based on 3rd order ENO scheme is capable of simulations of much more complicated free surface effects.
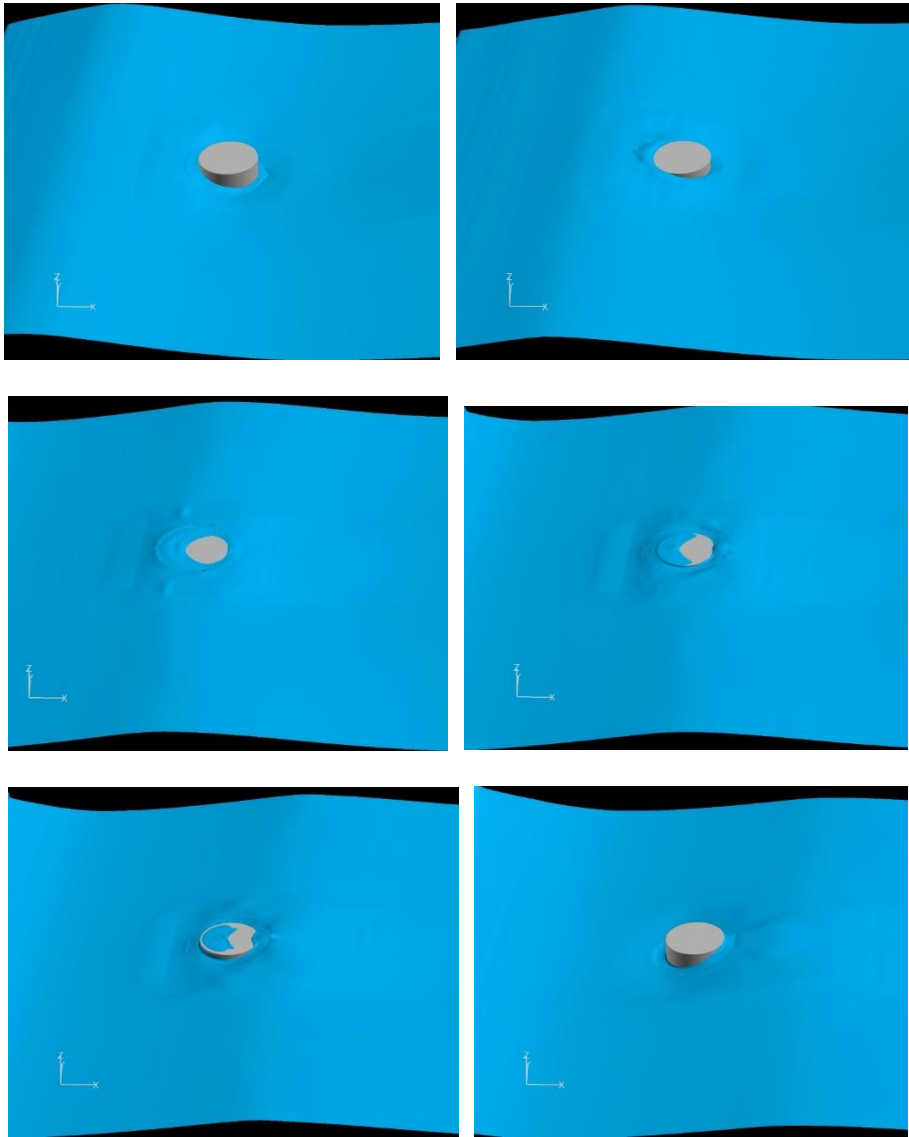
Figure. 11 Green water test case

4.6 Verification of Overset Grid Method

Two overset grid approaches are used to accommodate the floater motion as discussed in Chapter III. Figure. 12 shows the comparison of the two overset grid methods by modeling Buoy #2 with truncated mooring system used by Ryu et al. (2006). Method #1 is the method which calls PEGSUS to do the interpolation at every time step, moves only the adjacent blocks to the buoy, and allows the simulation of motions of six DoFs. Method #2 is the method of calling PEGSUS at only the initialization stage and moving all computational blocks along with the buoy, including the background mesh. Method #2 only allows simulation of horizontal motion.
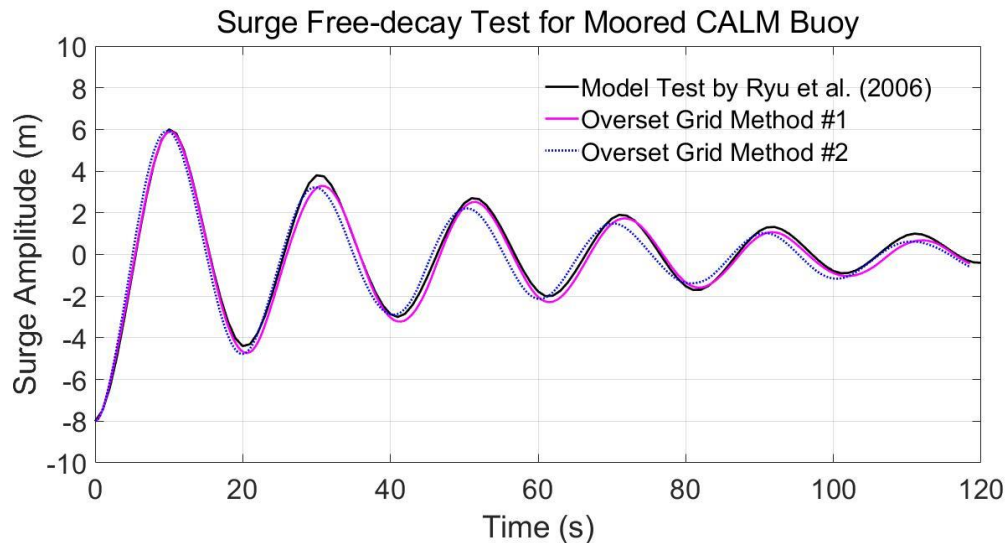
Figure. 12 Comparison of two overset grid methods

The surge free-decay tests for the CALM buoy with truncated mooring system are simulated by the two approaches for the verification of overset grid method. The results indicate that the simulated time histories of both approaches agree well with the

59

experimental measurements. Method #2 is faster in computation. However, the application of Method #2 is limited to horizontal motion when heave and rotation are negligible. It can be used in scenarios like VIM simulation of semi-submersible. Method #1 is adopted for the simulation of CALM buoy.

4.7 Validations for Free Decay Tests

Simulations for free decay tests of Buoy #2 in surge, heave, and pitch are performed with the coupled FANS-MOORING3D codes. The resultant free-decay motion is compared to model tests by Ryu et al. (2006) to validate the CFD model and the mooring system set-up.

Figure. 13 compares the free-decay surge motion of the buoy model obtained from the coupled analysis and the model test. The simulated surge motion agrees well with the model test, demonstrating the accuracy of the numerical model in capturing the added mass and damping. Both the numerical simulation and experiment unveil the natural period of the CALM buoy system in the surge direction to be approximately 20.5 seconds. The simulated motion in the first period nearly overlap with the model test. Starting from the second period, the comparison between the two motion time histories illustrates a slight difference of at most 5%. The skirt correction is not applied because the skirt influence is minimal in the surge direction. The agreement between the simulation and experiment indicates the overall inertial and damping effects calculated in the coupled analysis to be approximately equivalent to the model tests. The MOORING3D program correctly models mooring stiffness, line inertial effects, and mooring-induced damping

effects. The CFD module not only correctly models the CALM buoy's added mass, but also reasonably models the viscous damping effects with the use of LES.

Figure. 14 compares the pitch free-decay motion obtained from the coupled analysis to the model tests. The comparison manifested a minor discrepancy between the two motion time histories. The pitch period in the coupled analysis is around 4.7 seconds, almost identical to the experimental pitch period of 4.8 seconds. The pitch motion in model tests manifests a slightly faster trend of attenuation than the coupled analysis, but both time histories indicates the amplitude being reduced to lower than 5% of the original amplitude after about five cycles. The amplitudes of both time histories diminish to about $0.5°$ in the fifth cycle, meaning the pitch motion almost vanishes. Figure. 15 compares the free-decay heave motion obtained from the coupled analysis to the model test. The comparison reveals a minor discrepancy between the two motion time histories. The heave period in the coupled analysis agrees well with the experimental heave period of 6.8 seconds. Both time histories show that after four cycles, the amplitudes are reduced to less than 5% of the initial amplitude. The skirt approximation is applied to pitch and heave free-decay simulations. The agreement-of-motion comparison in Figure. 14 and Figure. 15 not only indicates the skirt being reasonably approximated, but also demonstrates the inertial and damping effects from CALM buoy and its mooring system being correctly modeled.
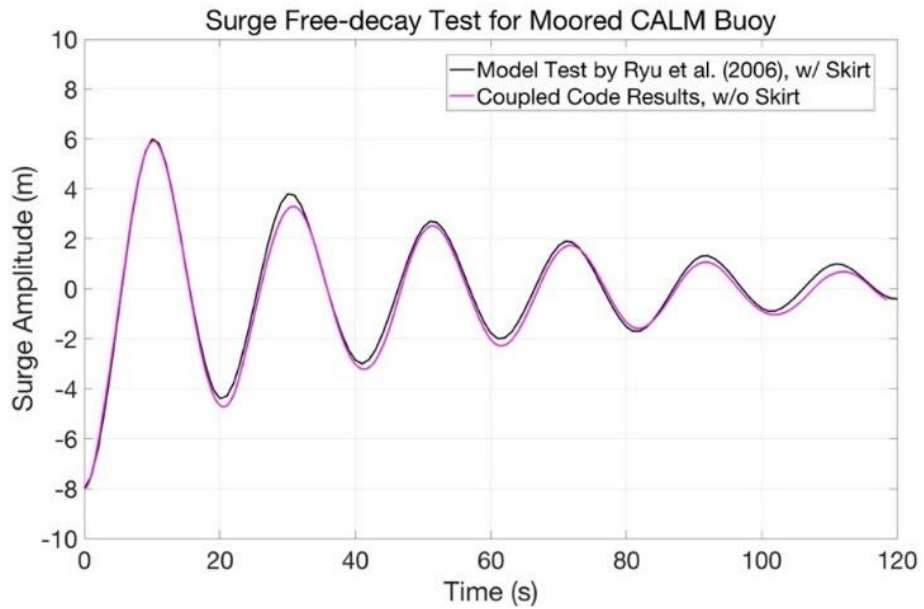
Figure. 13 Comparison between simulated surge free decay motion and model test
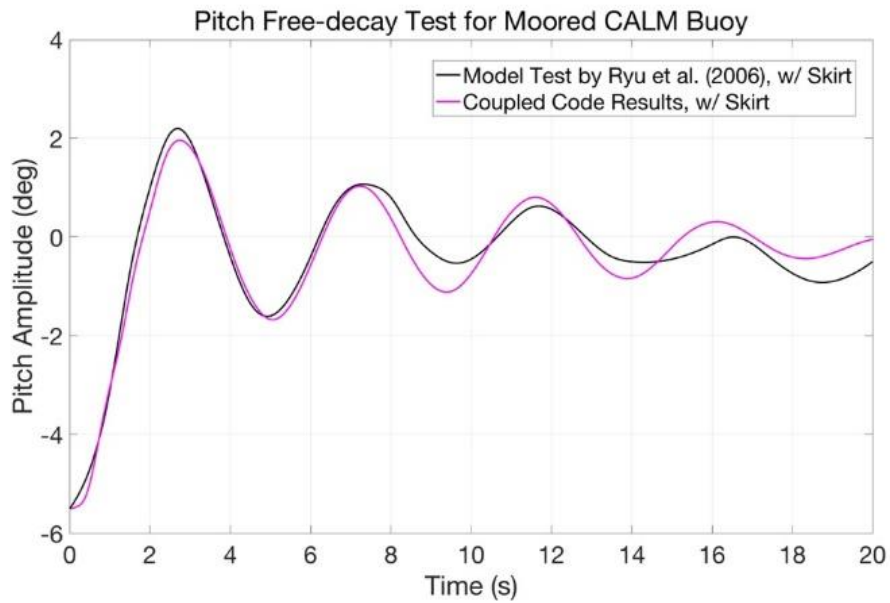
Figure. 14 Comparison between simulated pitch free decay motion and model test

62
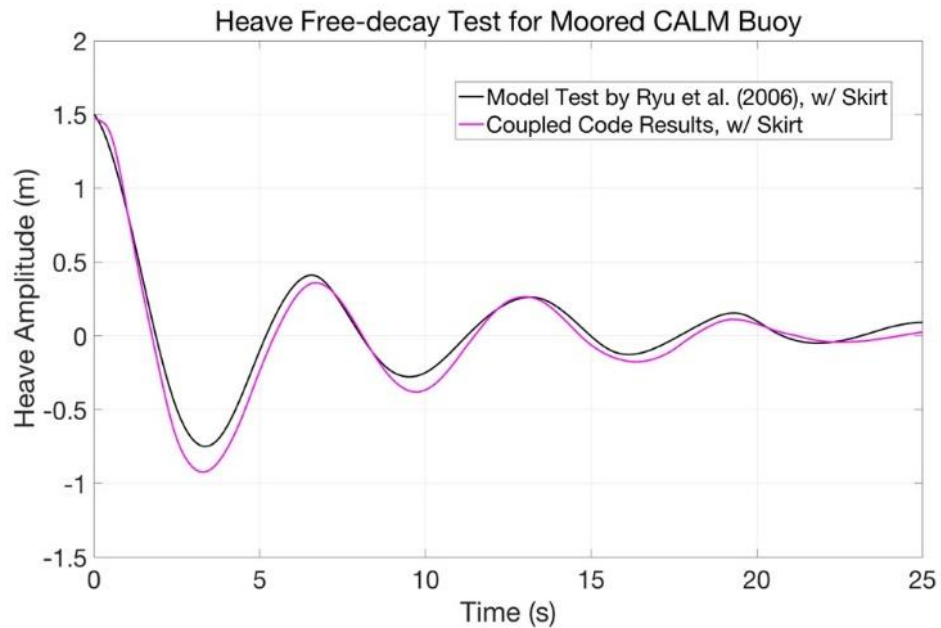
Figure. 15 Comparison between simulated heave free decay motion and model test

To summarize, the calculated natural frequencies of surge, heave, and pitch are 0.048, 0.147, and 0.208 Hz, respectively, and generally match with the natural frequencies obtained in the model tests. Additionally, the comparison of time histories manifests similar amplitude attenuation rate in the surge, heave, and pitch directions. Both inertial effects and damping effects of the CALM buoy system are correctly modeled by the coupled CFD-FEM code. The dynamic interaction between the buoy and its mooring system is modelled correctly. The coupling between the FANS CFD code and the FEM mooring model is validated by this experimental comparison.

CHAPTER V

WAVE-INDUCED MOTION OF CALM BUOYS

5.1 Introduction

This chapter describes the simulations for wave-induced motion of CALM Buoys with the coupled FANS-MOORING3D codes.

Section 5.2 presents the modeling details of Buoy #1 with AQWA-Orcaflex integrated model, which is the conventional approach in industry. Section 5.3 presents the coupled CFD-mooring simulation results of Buoy #1 and discusses the reasons leading to the discrepancy between the CFD-mooring analysis and the diffraction-based analysis.

Section 5.4 presents the wave-induced motion simulated results of Buoy #2 and its validation by comparing to experimental measurements. Section 5.5 presents the simulated wave-current-body interaction of Buoy #2.

5.2 AQWA-Orcaflex Integrated Model of Buoy #1

The CFD-mooring coupled program is compared to the existing commercial software AQWA and Orcaflex, which are widely used by the industry. Regular wave analyses are performed by both approaches with wave periods of 8.5, 9.2, 10.5, 11.5, and 12.5 seconds. These five periods are selected since the experimental wave load RAOs from wave period of 8 to 13 seconds were available in model tests of Bunnik et al. (2002). The hydrodynamics calculated by AQWA-LINE can be validated by comparing against

experimental measurements. The skirt is omitted in both the CFD-mooring coupled code and the AQWA model due to the skirt's limited size data.

AQWA, the diffraction analysis program, is used to model the buoy to obtain hydrodynamic loading, by running for a range of wave frequencies to build data on load RAOs, added mass and radiation damping. The load RAOs are defined as the ratio of wave exciting forces to wave amplitude in the frequency domain and are critical in determining the buoy motion. Figure. 16 shows the load RAOs obtained in AQWA and the corresponding experimental measurements.

Bunnik et al. (2002) measured wave load RAOs of the buoy for not only irregular wave but also various cases of regular waves. The load RAOs of regular waves show slight differences in surge and heave directions. However, the regular waves manifest discrepancy with irregular waves in terms of load RAOs in the pitch direction. The regular wave load RAO shows approximately 50% larger than irregular wave load RAO in the period of 9 seconds in pitch direction. In addition, the experiments of regular waves reveal that the load RAOs are dependent on the wave amplitude at certain periods. For instance, the load RAOs with wave height of 2m is almost 1.8 times the load RAOs with wave height of 1m. The wave load RAOs are not sensitive to wave amplitude in surge and heave directions, according to slight differences between wave height of 2m and 1m.

In terms of the comparison between load RAOs calculated by AQWA and experiments, Figure. 16 shows that the AQWA numerical results agree well with the experiments in surge and heave directions. The measured load RAOs shows slightly larger than RAOs from AQWA diffraction analysis in surge direction. The diffraction analysis

results almost agree with measurements also in heave direction. The skirt is omitted in the diffraction model, and it exerts limited effects on the load RAOs in surge and heave directions. However, the load RAOs in pitch directions show discrepancies with experimental measurements. Bunnik et al. (2002) also provided phases of wave loads with respect to frequencies. Phases of wave loads from AQWA agree well with phases through experiments in surge and heave directions. But AQWA results have phase difference of about 60° in pitch direction.

This is consistent with conclusions drawn by Bunnik et al. (2002) that the surge and heave wave forces are far less influenced by the skirt, while the pitch moments on the buoy are affected by the presence of the skirt. In addition, the buoy draft in the diffraction analysis model is fixed, without considering the free surface effects. Both of skirt effects and free surface effects probably lead to the difference between diffraction analysis results and experimental measurements of pitch wave load RAOs.

The hydrodynamic output of AQWA are regarded as the input of Orcaflex. The full-scale 9-point slack chain mooring system is modeled in Orcaflex to attain a time-domain coupled analysis. The reaction forces of the attached mooring lines, as well as all the hydrodynamic loads based on the AQWA input, are calculated, and used in the motion equations of the CALM buoy in each time step. The resulting motions, velocities and accelerations of the buoy are used in the dynamic equations of the mooring and offloading lines to calculate the line loads on the floaters. The time step is 0.1 second in OrcaFlex simulations.
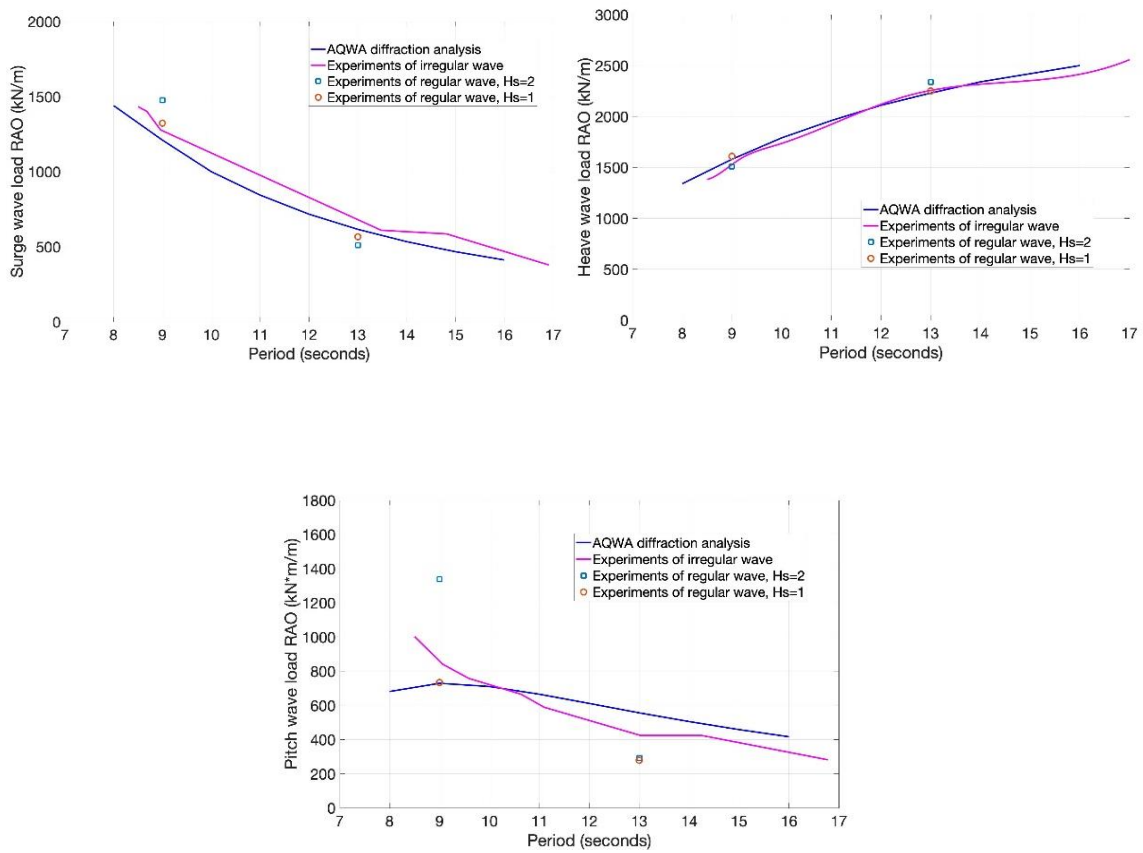
Figure. 16 Wave excitation load RAO calculated in AQWA vs Experiments

5.3 Wave-induced Motion of Buoy #1

The motion time histories obtained through the two numerical simulations are compared in this section. The time histories are not expected to be the same, due to discrepancies of hydrodynamics calculated from AQWA and CFD, even though the wave load RAOs of AQWA are validated against experiments.

Woodburn et al. (2005) used similar approaches to study the motion behavior of a CALM buoy in the EU FP5 EXPRO-CFD Project. The buoy had a diameter of 23 m, larger than Buoy #1 with OD of 20 m. The mooring configuration and properties were not available in Woodburn et al. (2005). AQWA-LINE was used to build a diffraction panel model. AQWA-NAUT was then run with the floating system modeled as simple point mass and inertia, with attached mooring lines modeled as rod elements by using the lumped mass method, which was the same modeling approach as in Orcaflex. The experiments, commercial CFD analysis, and diffraction-based analysis are all available in the study of Woodburn et al. (2005) and reveal how they are correlated, providing feasible references for our analyses.

5.3.1 Motion Analysis

The sea elevation and motion time histories calculated by the CFD-mooring coupled analysis and AQWA-Orcaflex are compared. Figure. 17, Figure. 18, Figure. 19, Figure. 20, and Figure. 21 show the comparison with wave periods of 8.5, 9.2, 10.5, 11.5, and 12.5 seconds, respectively. The wave heights of 3 to 4 meters are selected in the CFD-mooring coupled analysis so that the wave amplitude covers sufficient vertical meshes to

ensure the accuracy of level-set method. The Airy regular wave with the same wave height is generated in Orcaflex for each wave period.

Figure. 17 and Figure. 18 show that the surge motion time histories of the coupled analysis manifests motion of low frequency other than the wave frequency when wave period is 8.5 or 9.2 seconds. The surge oscillation amplitude appears smaller than the AQWA-Orcaflex results if excluding the low frequency oscillation for both wave periods. The low frequency surge motion corresponds to the surge natural frequency of the buoy system and could possibly be due to the turbulence modeled by LES. Besides, it may be induced by the initial pulse of the wave. Since the ramp-up stage is not incorporated in the wavemaker boundary condition, the first few waves hitting the buoy are slightly stronger than the waves after stabilization, applying some impulse to the buoy and leading to the low frequency motion.

The heave motion amplitudes of the coupled analysis appear smaller than those of AQWA-Orcaflex model for most time periods. The time histories of both numerical simulations have slight phase differences in surge and heave directions, which is due to the viscous effects modeled in CFD. However, the pitch motion amplitude of coupled analysis is larger than that of AQWA-Orcaflex with considerable phase differences. One reason of considerable phase difference is that the buoy's diffraction model cannot predict well the wave exciting loads and phases in the pitch direction. Another reason is that the damping effects caused by viscous forces and turbulence are modeled in the CFD, which can contribute to the phase lag. The nonlinear hydrodynamic effects, viscous effects, and

69

turbulence effects that may contribute to the difference are to be discussed in the RAO analysis.

Figure. 19, Figure. 20, and Figure. 21 show that the surge motion time histories of the coupled analysis are mostly regular after the ramp-up stage, when wave period is 10.5, 11.5, and 12.5 seconds. Low frequency motion is negligible in these three cases. The surge amplitudes also appear smaller than those of Orcaflex. The phase difference is negligible in the surge direction. The heave motion of the coupled analysis appears smaller than those of Orcaflex. The pitch amplitudes of coupled analysis are larger than that of Orcaflex with phase differences.

Figure. 17 Comparison of wave elevation and motion time histories, T=8.5s

Figure. 18 Comparison of wave elevation and motion time histories, T=9.2s

70

Figure. 19 Comparison of wave elevation and motion time histories, T=10.5s
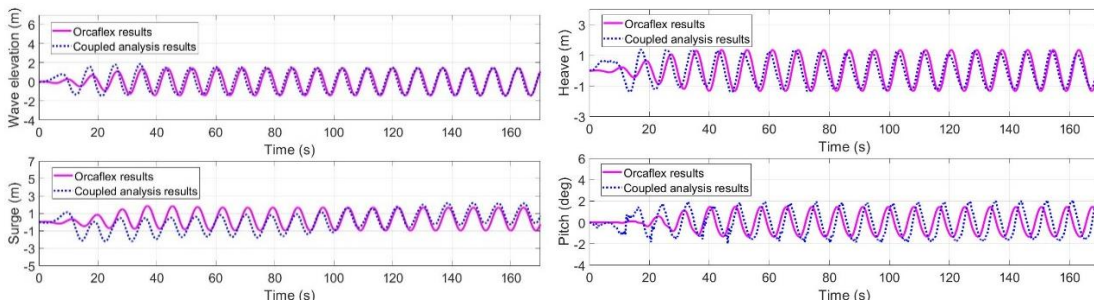

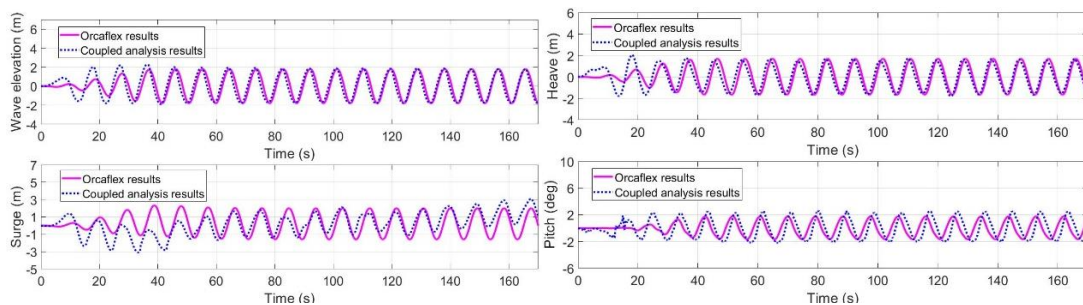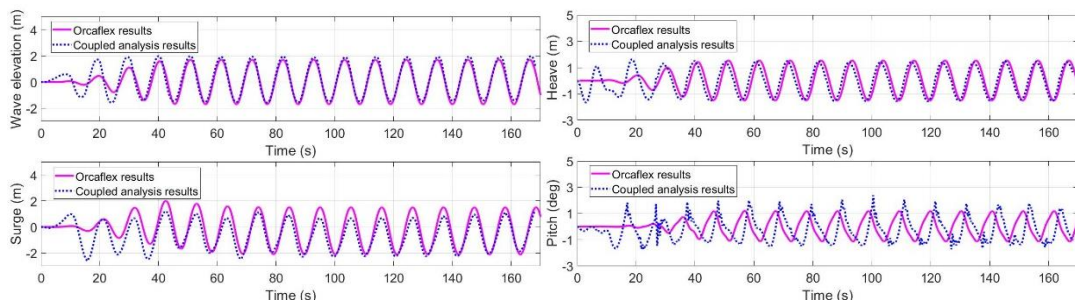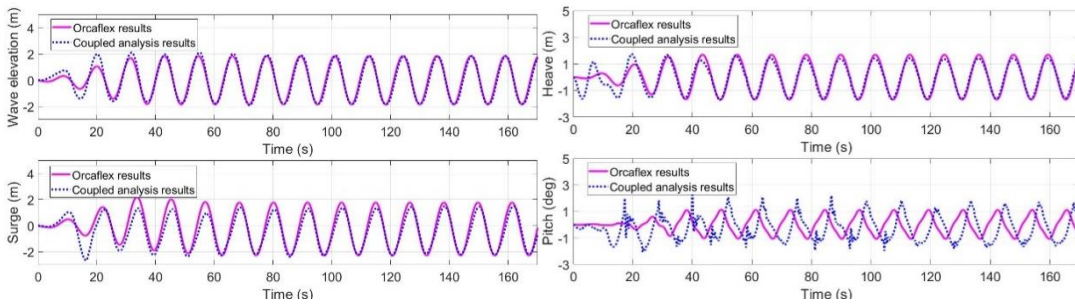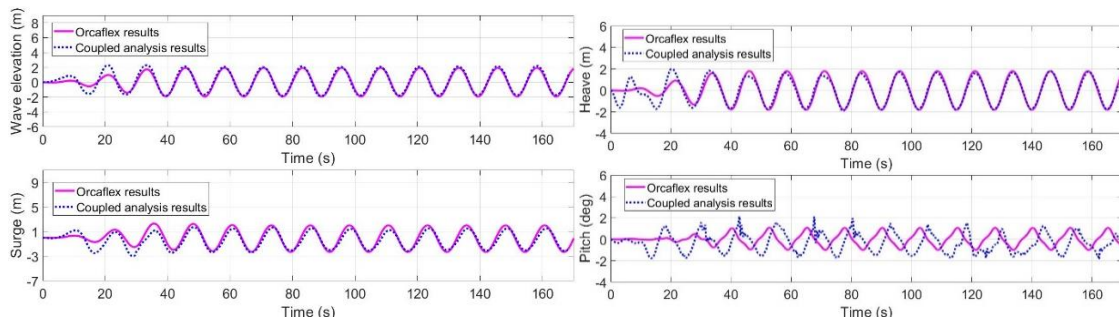**Figure. 20 Comparison of wave elevation and motion time histories, T=11.5s**

Figure. 21 Comparison of wave elevation and motion time histories, T=12.5s

71

5.3.2 Spectrum and RAO Analysis

RAO, which maps the wave elevation process to the dynamic response process, is given by the square root of the ratio of response spectra to wave spectra. RAO analysis is performed on numerical results of both simulations. The first approach is the harmonic spectrum analysis which can exclude the motion components other than wave frequencies. Another set of RAOs are obtained by calculating standard deviation (SD) of motion and dividing it by that of sea elevation. The motion components at all frequencies are covered in the SD approach.

The spectrum analysis comparisons are displayed in Figure. 22. The main peaks of each spectrum diagram are positioned at 0.118, 0.109, 0.095, 0.087, and 0.08 Hz, corresponding to the periods of 8.5, 9.2, 10.5, 11.5, and 12.5 seconds. The surge spectrum of wave periods of 8.5 and 9.2 seconds have leftmost peaks at low frequency of around 0.01 Hz, indicating that the surge time histories have motion components at low frequency as observed in Figure. 17 and Figure. 18. The surge spectrum of periods of 10.5 and 11.5 seconds appears flat other than the primary peak, agreeing with the observation of regular pattern in Figure. 19 and Figure. 20. The surge spectrum of period of 12.5 seconds also has a leftmost peak at low frequency. The peak is small compared to the main peak, meaning the low frequency motion is not considerable as it is shown in Figure. 21. The pitch spectra of all wave periods have peaks at frequencies two times the wave frequency, which might contribute to the slight irregular fluctuations of pitch motion.

RAO results of both coupled analysis and Orcaflex are summarized in Table 6. RAOs through spectrum analysis and SD approach are computed and compared to

AQWA-Orcaflex results. The spectrum analysis and SD approach lead to different results for motions that comprised components other than wave frequencies as shown in Figure. 22. The surge RAO of period of 8.5 seconds through spectrum analysis is about 20% smaller than that of SD approach. The RAO results of two approaches are close with differences of up to 3% for relatively regular motion time histories.
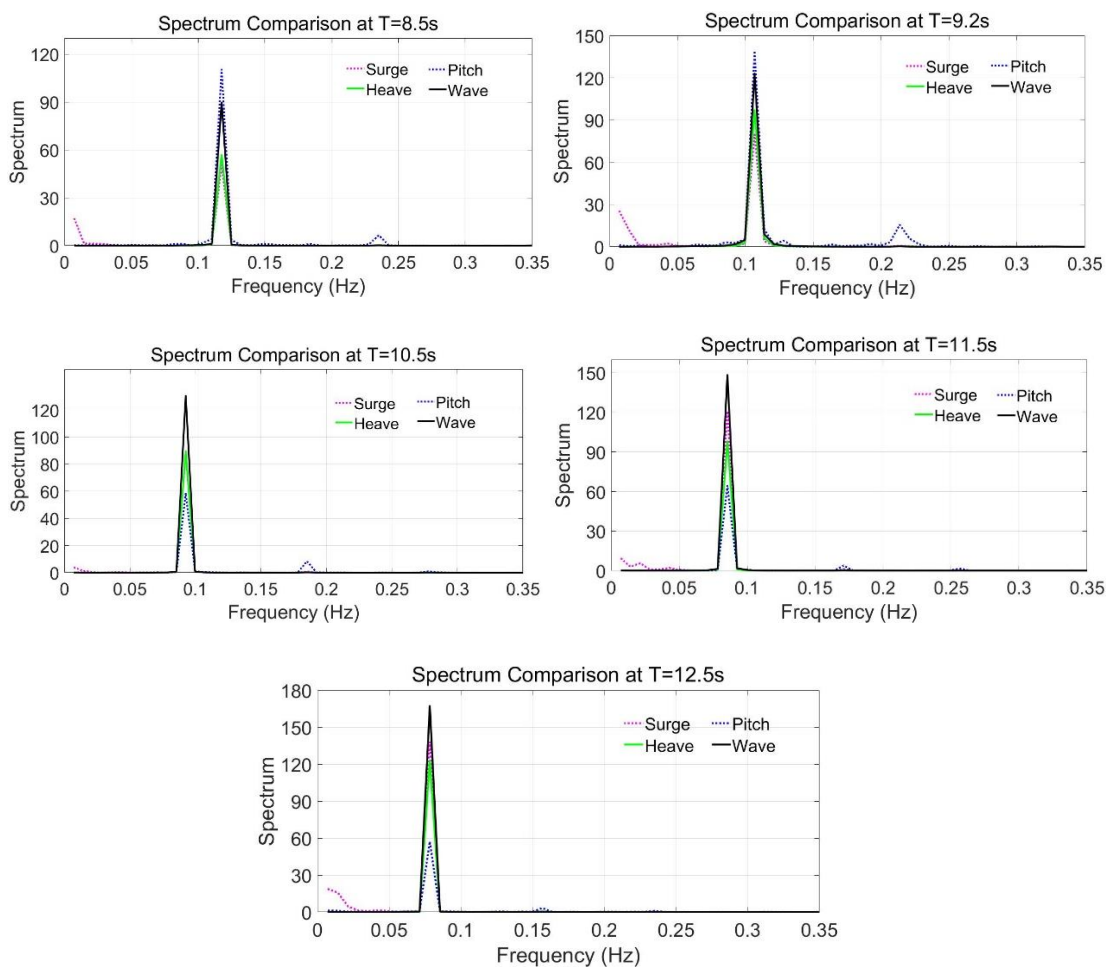
Figure. 22 Spectrum analysis results of coupled CFD-mooring analysis

RAOs from both approaches are shown in the right plots of Figure. 23. The comparison results of Woodburn et al. (2005) are also included in the left plots of Figure. 23. Our results can be compared to Woodburn's results, due to the similar buoy dimension and the same methodologies. Observing the right plots, the surge and heave RAOs obtained through the CFD-mooring coupled analysis generally manifest smaller than the AQWA-Orcaflex modeling approach. In terms of the pitch RAOs, CFD results manifest larger than AQWA-Orcaflex results in all wave periods.

Table 6. RAO results summary of Buoy #1

Period	Motion	RAO (Spectrum analysis)	RAO (SD Ratio)	RAO of Orcaflex
8.5s	Surge	0.788	0.829	0.929
	Heave	0.812	0.796	0.946
	Pitch	1.109	1.159	0.993
9.2s	Surge	0.763	0.940	1.006
	Heave	0.887	0.866	0.933
	Pitch	1.063	1.17	0.945
10.5s	Surge	0.823	0.863	1.063
	Heave	0.829	0.837	0.893
	Pitch	0.671	0.742	0.648
11.5s	Surge	0.902	0.907	1.106
	Heave	0.814	0.811	0.914
	Pitch	0.659	0.714	0.542
12.5s	Surge	0.914	1.04	1.123
	Heave	0.858	0.848	0.928
	Pitch	0.564	0.607	0.473

(a) Buoy of Woodburn et al. (2005)   (b) Coupled CFD-mooring analysis
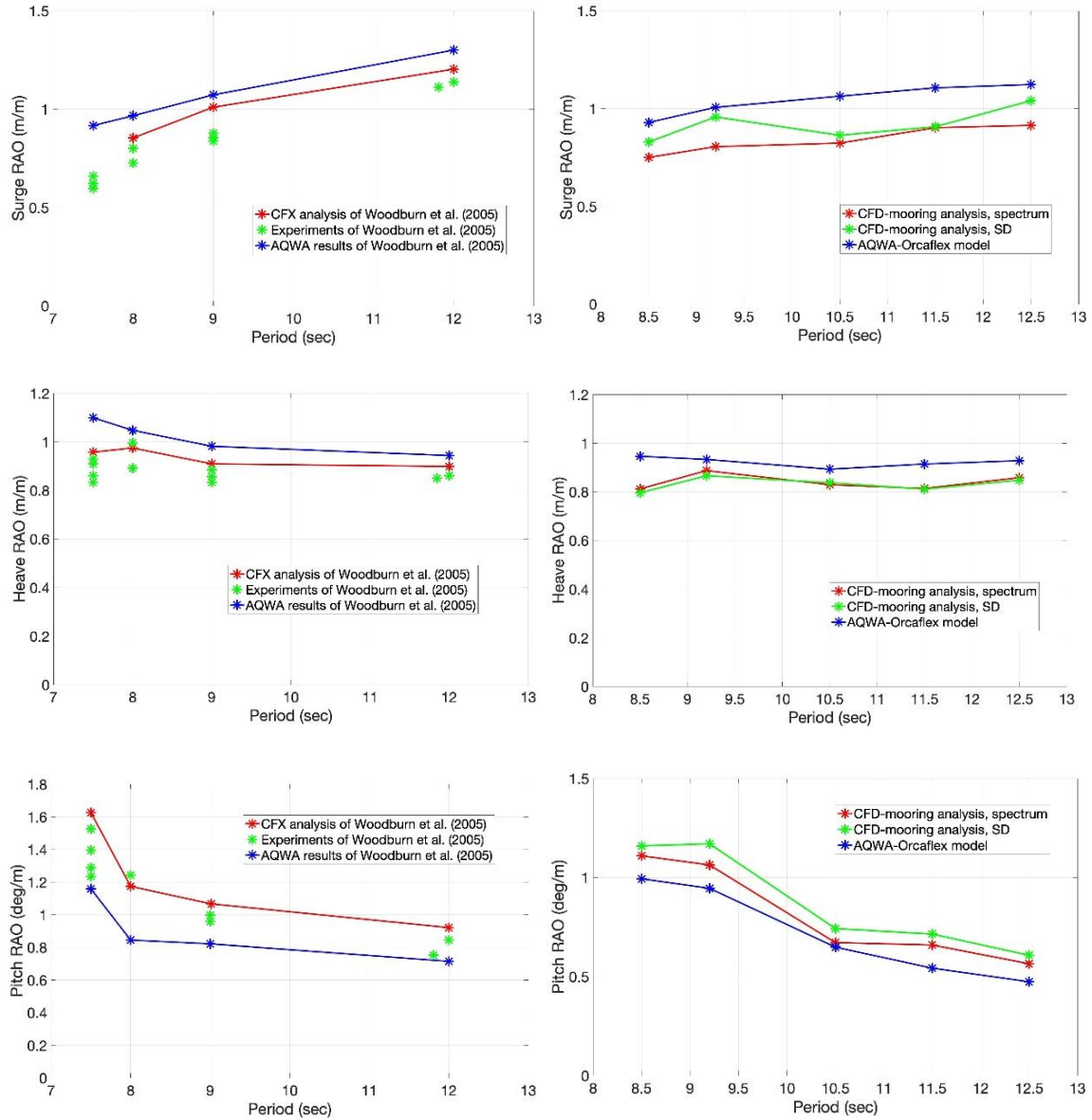

Figure. 23 RAO comparison.

(a): buoy of Woodburn et al. (2005) (OD=23m). (b): CALM buoy #1 (OD=20m).

The trend is consistent with studies performed by Woodburn et al. (2005). Woodburn et al. (2005) indicated that the AQWA model generally over-predicted the response in surge and heave and under-estimated the pitch response comparing to experiments, and our analysis reveal that the AQWA model predicts larger surge and heave responses and smaller pitch response than the CFD-mooring coupled analysis. Woodburn et al. (2005) also indicated that their EXPRO-CFD results were closer to the experimental measurements than AQWA in all DoFs.

Table 7. RAO ratios of change summary of Buoy #1

T	Motion	AQWA to CFD	AQWA to CFD	T	Motion	AQWA to experiments
8.5s	Surge	-15.2%	-10.8%	7.5s	Surge	-31.7%
	Heave	-14.2%	-15.6%		Heave	-19.7%
	Pitch	11.7%	16.7%		Pitch	17.5%
9.2s	Surge	-24.1%	-6.6%	8s	Surge	-21.1%
	Heave	-4.9%	-7.2%		Heave	-9.9%
	Pitch	12.5%	23.8%		Pitch	47.15%
10.5s	Surge	-22.6%	-18.8%	9s	Surge	-20.2%
	Heave	-7.2%	-6.3%		Heave	-12.6%
	Pitch	3.5%	14.5%		Pitch	19.1%
11.5s	Surge	-18.4%	-18.0%	12s	Surge	-13.5%
	Heave	-10.9%	-11.3%		Heave	-9.3%
	Pitch	21.6%	31.7%		Pitch	11.8%
12.5s	Surge	-18.6%	-7.4%			
	Heave	-7.5%	-8.6%			
	Pitch	19.2%	28.3%			

The ratios of change are summarized in Table 7. The reduction ratio from AQWA to CFD analysis is around 15% to 25% in surge direction, and the reduction ratio from AQWA to experiments of Woodburn et al. (2005) is around 13% to 30%. The reduction ratios in heave direction are around 5% to 16%, and the corresponding reduction ratios of experiments are around 9% to 20%. The increasing ratio in pitch direction are around 10% to 30%, and the corresponding increasing ratios of experiments is 10% to 50%. Generally, the ratios of change of RAOs through the coupled CFD-mooring analysis agree with those of previous experiments. Though direct experiments are not available for this CALM buoy with the slack chain mooring system, we believe that the CFD-mooring coupled analysis provide better solutions than AQWA-Orcaflex model.

5.3.3 Discussion

The reduction in surge and heave RAOs of the CFD-mooring analysis should be due to the viscous and turbulent effects, which provide additional damping to the buoy system. Katayama et al. (2009) also conducted experimental studies on viscous effects of a drifting buoy and concluded that viscous effects are significant for the heave motions of the drifting buoy. Figure. 24 shows the typical momentum vector distribution around the buoy when the wave period is 11.5 seconds. Figure. 24 (a) and (b) show the scenarios when the buoy surges to the left and the right, and Figure. 24 (c) and (d) show the scenarios when the buoy heaves upside and downside, respectively. Strong vortex structure is observed near the buoy with the consideration of LES model.

The vortex is considered a strong element to contribute to the damping effects in surge, heave, and pitch. The vortex damping effects are difficult to be represented by a linear damping or drag coefficient estimation. The representation of linear wave radiation damping appears to be insufficient in the AQWA-Orcaflex model. The overall drag load on the buoy plays a significant role.

The increase in pitch RAOs of the CFD-mooring analysis requires further investigation, though it manifests the same trend with Woodburn et al. (2005). One reason is the inaccuracy of diffraction analysis in calculating pitch wave load RAO as it is shown in Figure. 16. The AQWA-Orcaflex model adopts the added mass, radiation damping and wave excitation loading RAOs calculated from the linear diffraction analysis, neglecting the non-linear hydrostatic and Froude-Krylov excitations at each time step over the wetted surface. The nonlinear effects brought about by changing free surface should be significant in the pitch direction.

The analysis results and the comparison with Woodburn et al. (2005) show that the practice of linear diffraction analysis for CALM buoy, especially in the pitch direction, seems not comprehensive. Though AQWA-Orcaflex coupled model is a popular approach in the industry, the accurate simulations and validations against experiments strongly depend on the empirical estimations for drag, inertia or lifting effects, and vortex shedding. In addition, the conventional approach adopts the linear added mass, radiation damping and wave excitation loading RAOs, neglecting the non-linear effects at each time step. The free-surface effects are captured and all hydrodynamic forces and moments acting on the buoy are calculated by pressure and shear force integration over the instantaneous

78

wetted surface in the CFD-mooring coupled analysis. The coupled method provides improved predictions of details including flow separation, viscous and turbulent effects.

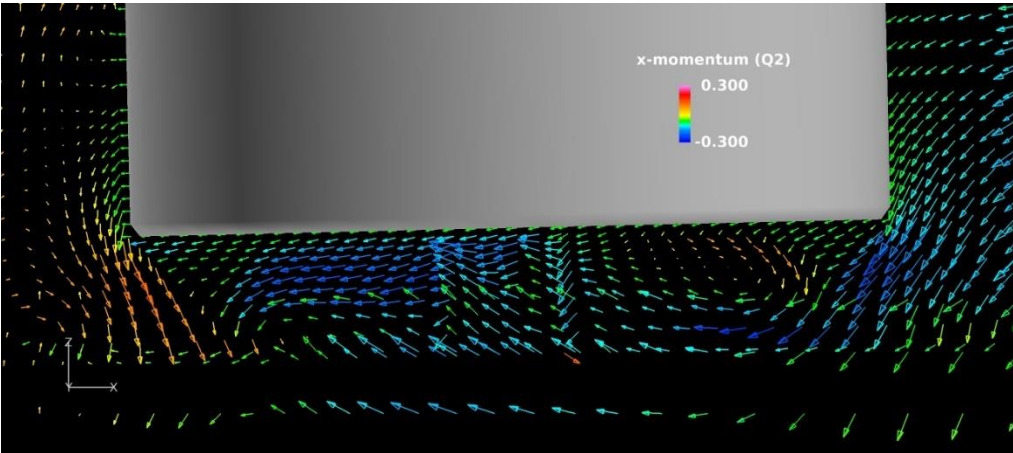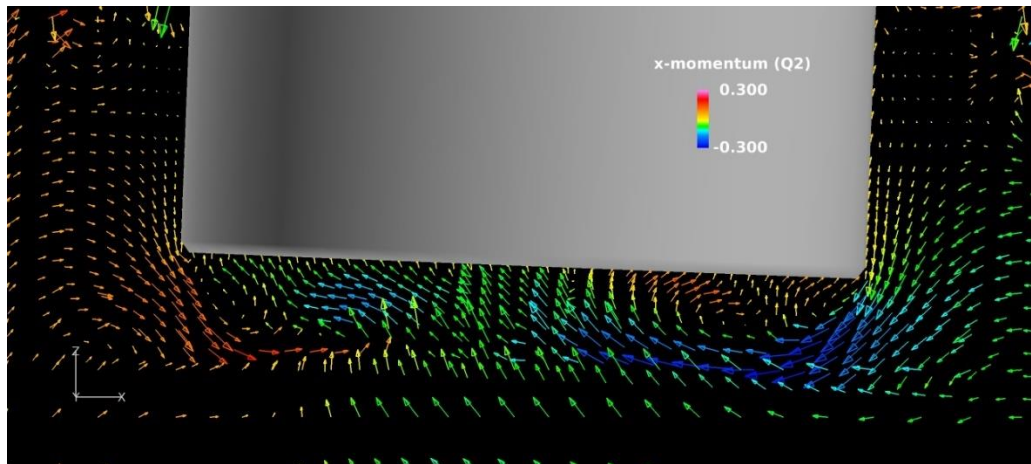(a) Surge to the left
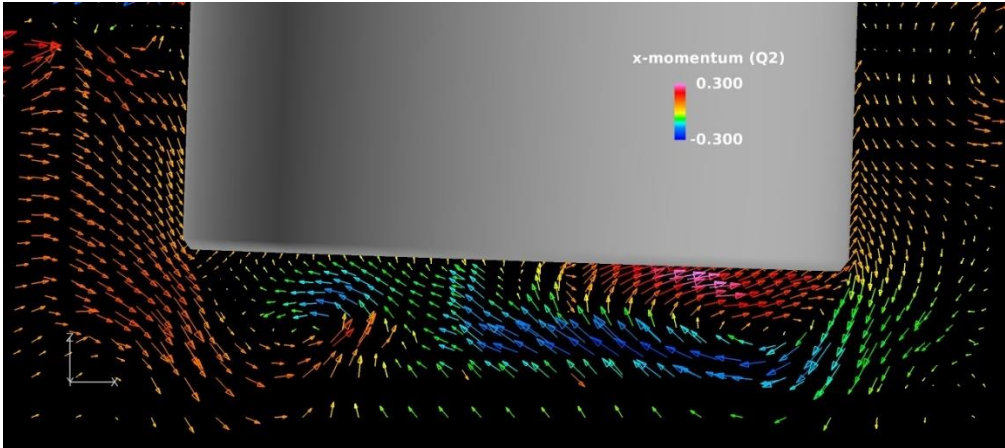
(b) Suge to the right

Figure. 24 Momentum field in the buoy's adjacent area
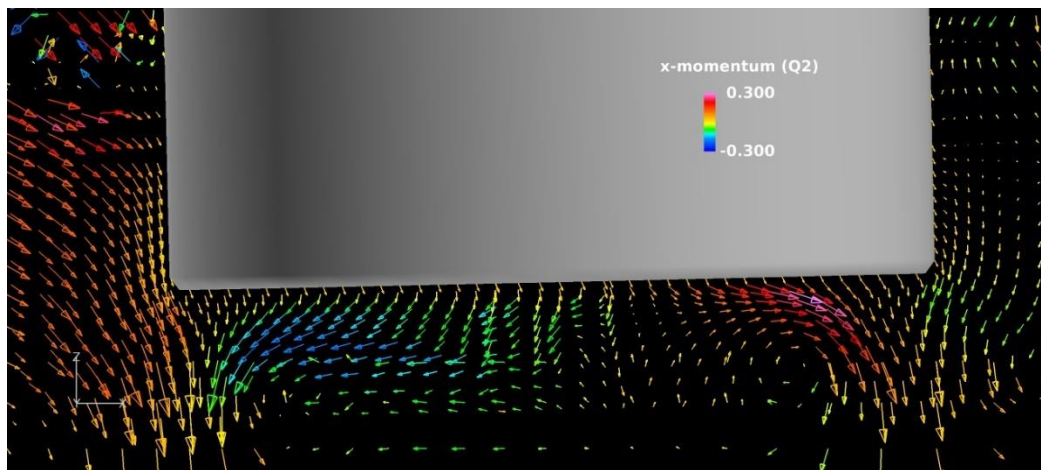
(c) Heave upside

(d) Heave downside

Figure. 24 (Continued) Momentum field in the buoy's adjacent area

5.4 Wave-induced Motion of Buoy #2

Ryu et al. (2006) conducted experiments for the CALM buoy in the Offshore Engineering Basin at the Institute for MARIN Dynamics in Canada. The same buoy is modeled as Buoy #2 in this study. Gu et al. (2019) studied CALM buoy response in currents with the coupled method, and the study is limited to horizontal inline and transverse motion.

Wave-induced motion simulations are performed with the model-scale buoy to achieve a straightforward comparison with model tests after the free-decay simulations are validated. Five sets of regular wave sequences are generated to study the buoy RAO, with time periods of 7, 8.5, 10.5, 12.5, and 14.5 seconds at full scale. The motions in sway, roll, and yaw are tiny and neglected in this section. The dynamic responses in surge, heave, and pitch are extracted. Harmonic spectrum analyses are conducted on the motion time histories of surge, heave, pitch, and wave elevation to unveil the buoy RAO, excluding the ramp-up time. The calculated RAO is compared to the model tests by Ryu et al. (2006).

5.4.1 Fluid Field Analysis

Five sets of regular wave sequences are generated to study the buoy RAO, with time periods of 7, 8.5, 10.5, 12.5, and 14.5 seconds at full scale. Wave elevations, fluid momentum and vortex field are extracted and investigated for the periods of 8.5 and 12.5 seconds, which are selected to illustrate the scenarios of short waves and relatively longer waves. The fluid momentum and vorticity are normalized by the characteristic length and velocity. Figure. 25 (a) and (b) manifest the buoy's response and wave elevation from a

81

side view of wave crest and wave trough at periods of 8.5 and 12.5 seconds. The blue region represents water, and the red area refers to air. The wave crest and trough are extracted at time steps of 950 and 1100 for the period of 8.5 seconds and at time steps of 800 and 1000 for the period of 12.5 seconds. On both Figure. 25 (a) and (b), the left plot shows the wave crest and the right one shows the wave trough. The buoy is lifted while the crest is passing, and then it sinks during the trough. The pitch motion is observable, with the buoy tilted with the wave surface.

(a) Wave crest and wave trough, T=8.5s;
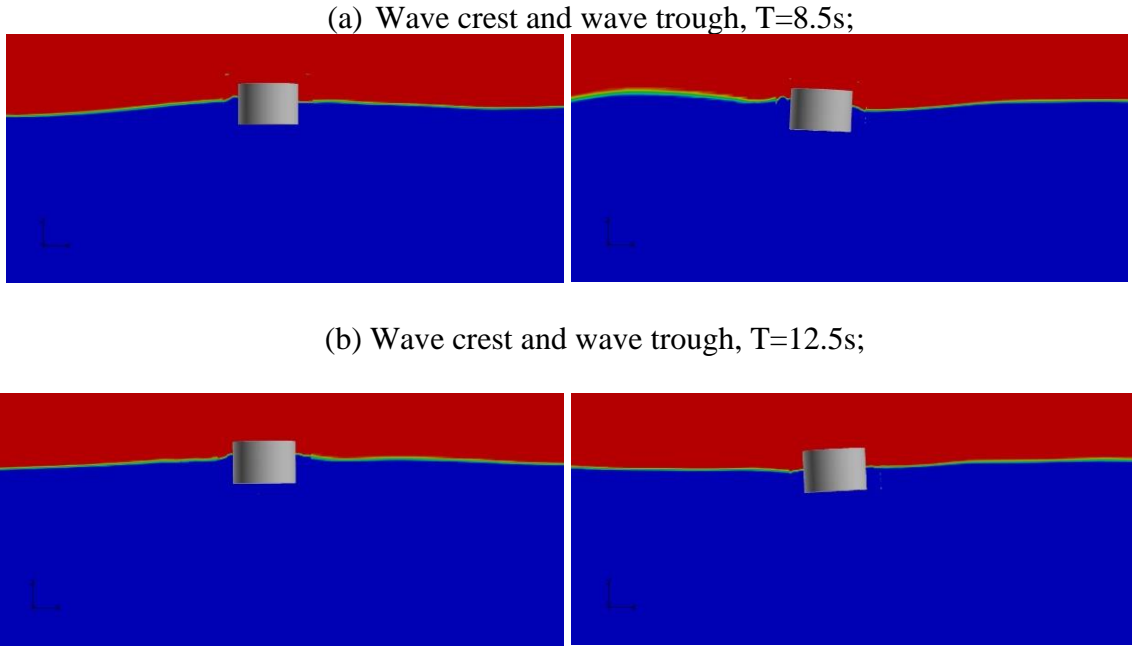

(b) Wave crest and wave trough, T=12.5s;

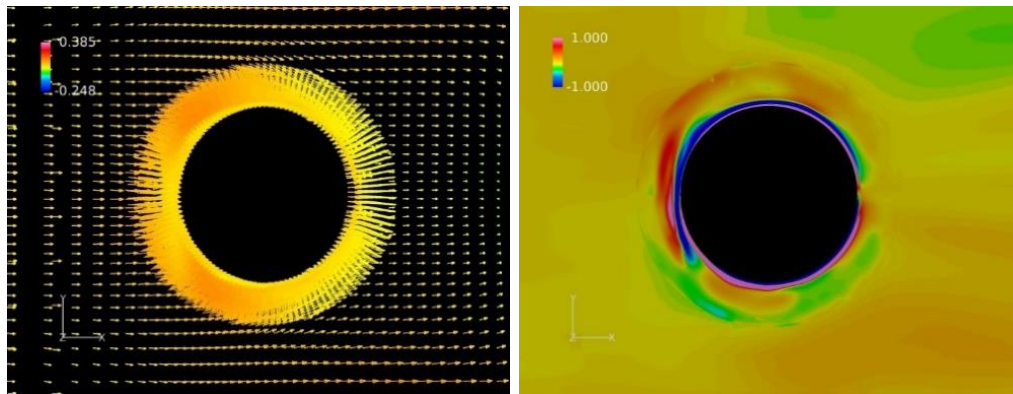**Figure. 25 Wave crest and wave trough, (a) T=8.5s; (b) T=12.5s**

Figure. 26 (a), (b), and (c) exhibit the flow momentum field and vortex distribution at the depth of z/D=-0.2 at time steps of 3200, 3300, and 3400, respectively, with a wave period of 8.5 seconds. Three time steps correspond to wave crest, in-between time, and

wave trough. The evolution of momentum and vorticity from wave crest to trough can be observed. The left plots display flow momentum field, and the right plots display vortex distribution in all figures (a), (b), and (c). Figure. 27 shows how momentum and vorticity evolve from wave crest to trough at a wave period of 12.5 seconds. The data are extracted at time steps of 3150, 3250, and 3350. It can be observed in both Figure. 26 and Figure. 27 that when the wave crest passes by the buoy, the fluid flows to the positive direction and pushes the buoy to the surge positive direction; oppositely, when the wave trough passes by the buoy, the fluid flows in the opposite direction from the wave crest and pushes the buoy to the negative direction.

Both Figure. 26 and Figure. 27 show vortex formation and evolution, with the vortex during crest passing being more conspicuous on the left side of the buoy. Because the flow is oscillatory, the vortex is not as fully developed and prolonged as the vortex pattern presented by Gu et al. (2019) when omnidirectional current is applied. The LES still captures the vortex evolution when the wave passes. The vortices indicate that the flow separation in the boundary layer around the buoy is modeled reasonably.

For the wave with the period of 12.5 seconds, the vortex appears in longer stretches that are extended farther away from the buoy. The vortex on the left side forming during the crest gradually vanishes as the wave passes, and the vortex begins to form on the buoy's right side during the wave trough. However, the vortex during the trough manifests in smaller and shorter stretches compared to those during the crest and is only limited to the adjacent areas of the buoy.

(a) Flow momentum and vortex field at wave crest, 3200th step;

(b) Flow momentum and vortex field between wave crest and wave trough, 3300th step;
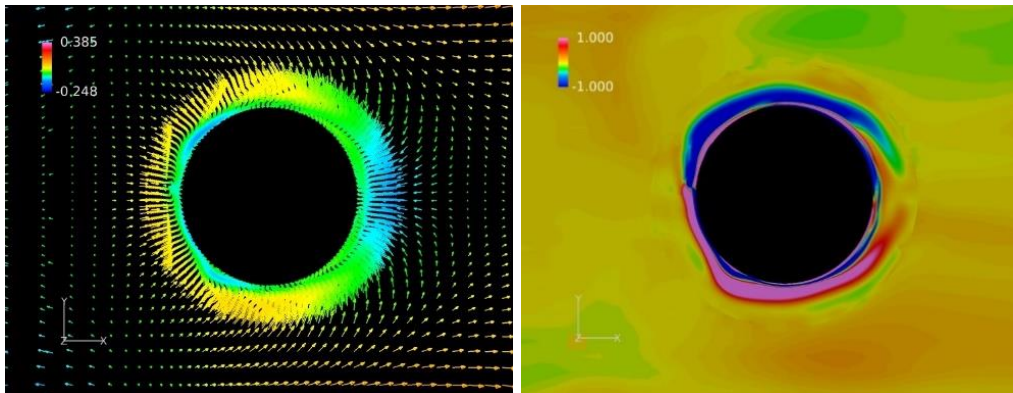
(c) Flow momentum and vortex field at wave trough,3400th step;
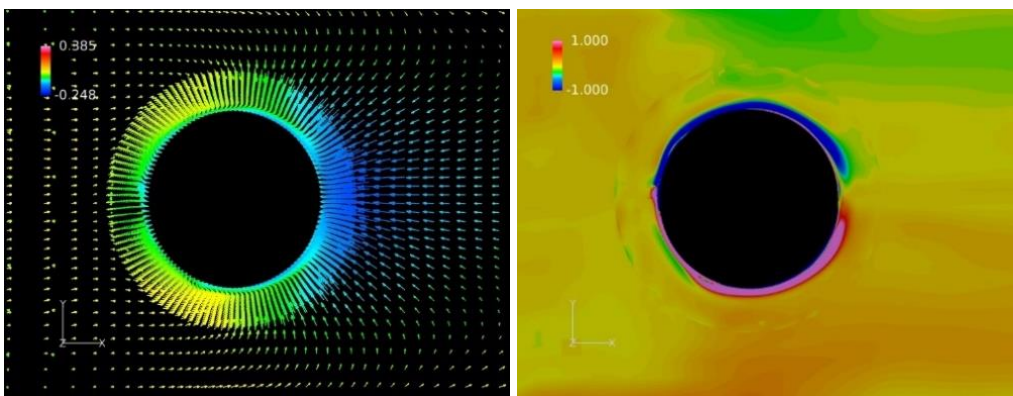
Figure. 26 Flow momentum field (left) and vortex distribution (right) at z/D=-0.2, T=8.5s

(a) Momentum and vortex field at wave crest, at 3150th step;
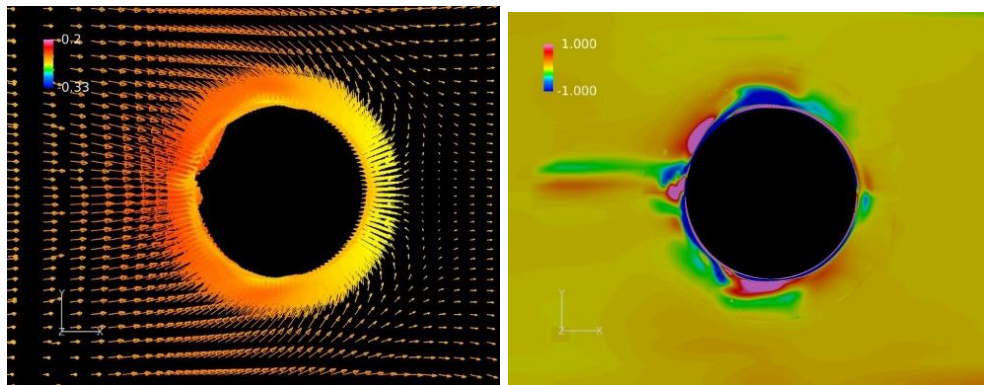
(b) Momentum and vortex field between wave crest and wave trough, at 3250th step;
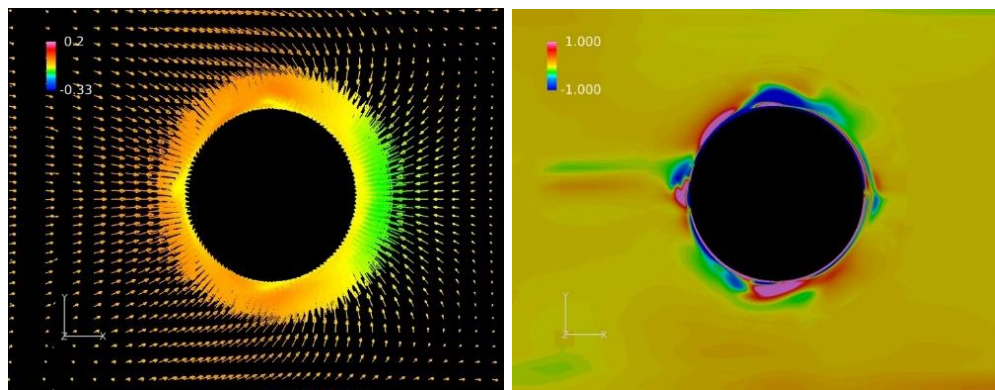
(c) Momentum and vortex field at wave trough, at 3350th step;
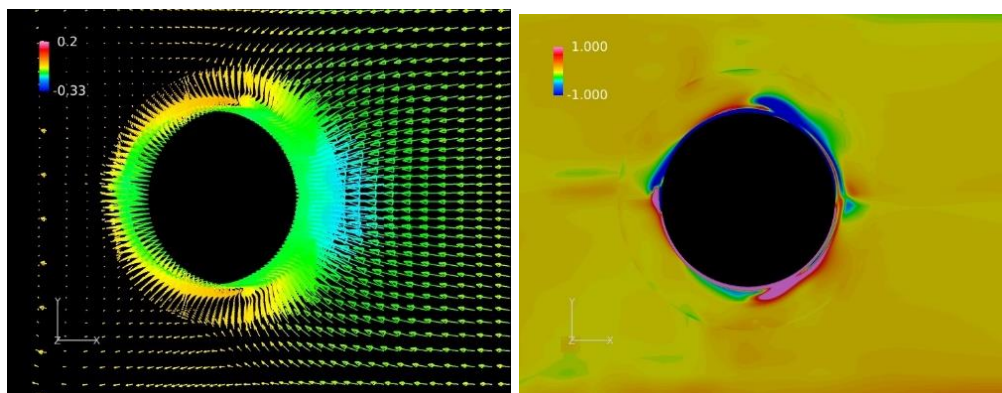
Figure. 27 Momentum field (left) and vortex distribution (right) at z/D=-0.2, T=12.5s

Figure. 28 shows the momentum distribution to the bottom of the buoy while wave crest or trough passes. Figure. 28 (a) and (c) indicates that strong vortex shedding occurs during the wave crest as the buoy surges to the positive direction. The vortex represents the viscous and turbulence damping effects that strongly influence the buoy's motion in surge, heave, and pitch. The eddy-relating damping effects are difficult to be estimated in the conventional numerical approach however can be modeled reasonably by CFD.

(a) Momentum at the bottom at wave crest, 3200th step; T=8.5 seconds
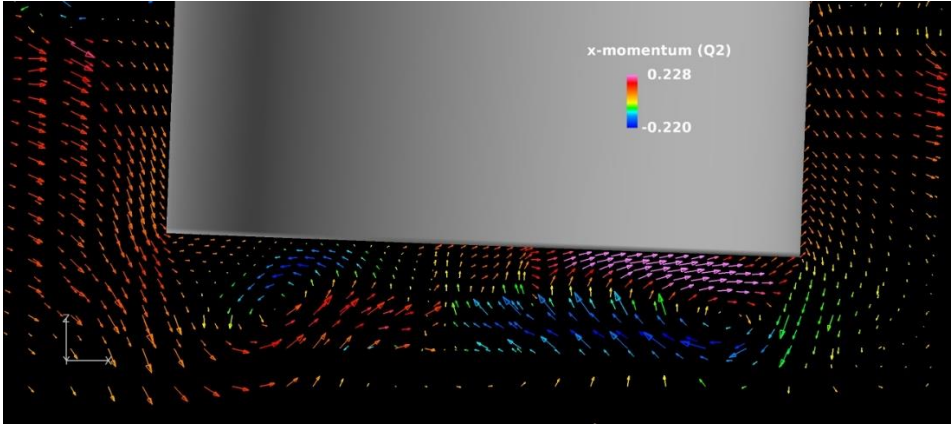
(b) Momentum at the bottom at wave trough, 3400th step; T=8.5 seconds
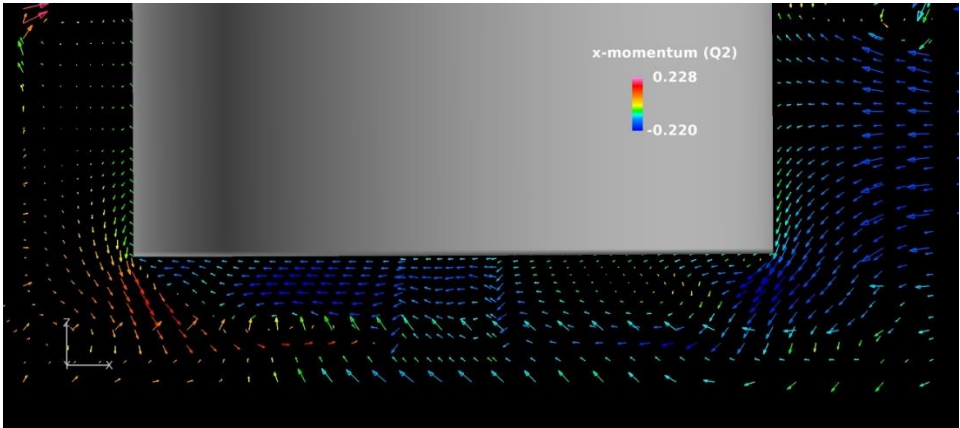
Figure. 28 Momentum field at the buoy bottom

86

(c) Momentum at the bottom at wave crest, 3150th step; T=12.5 seconds
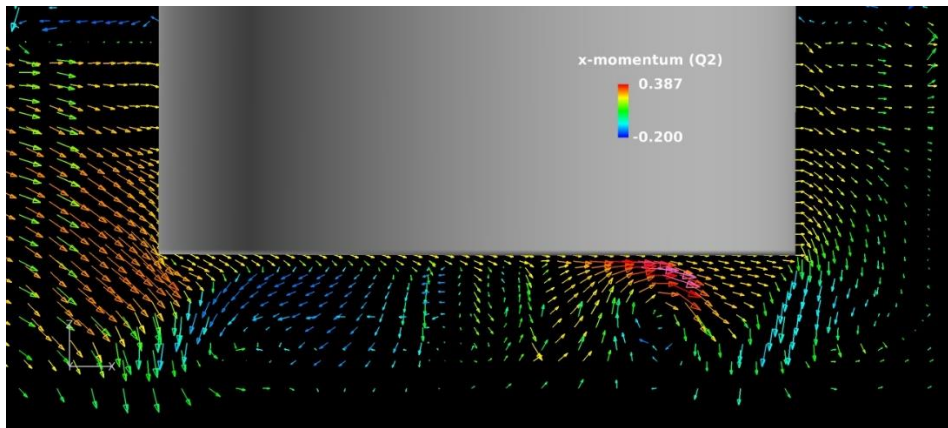
(d) Momentum at the bottom at wave crest, 3350th step; T=12.5 seconds
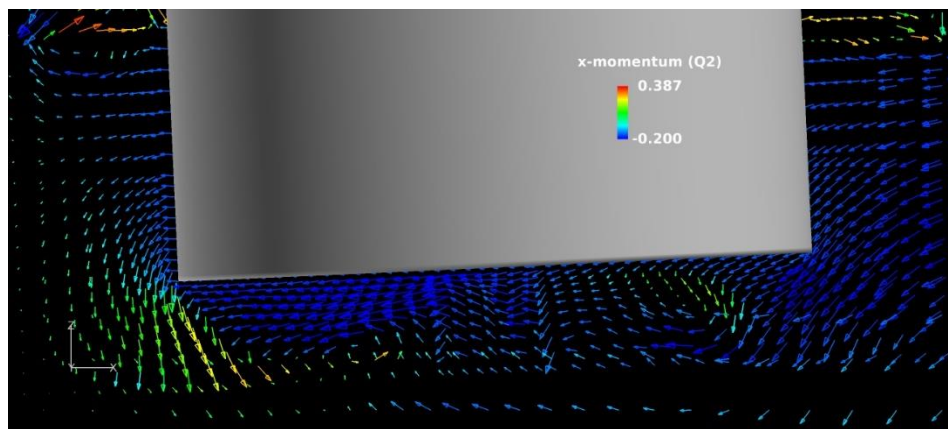
Figure. 27 (Continued) Momentum field at the buoy bottom

5.4.2 Motion and Spectrum Analysis

Figure. 29, Figure. 30, Figure. 31, Figure. 32, and Figure. 33 show the time histories of surge, heave, and pitch motion, wave elevation detected by the probe, and the associated harmonic spectrum analysis results, with incoming wave periods of 7, 8.5, 10.5, 12.5, and 14.5 seconds, respectively. The left plots exhibit comparisons of time histories, and the right plots exhibit comparisons of spectrum analysis results.

87

In all wave periods, the detected wave elevation manifests a regular pattern, which is consistent with the expectations and verifies the functionality of the numerical wavemaker. However, the CALM buoy's motion time histories in the three directions appear slightly irregular, especially for the surge and pitch motions. The irregularity implies that the motion includes motion components at certain frequencies other than the wave frequency. The phenomena are observed at other wave periods.

Harmonic spectrum analyses are carried out for the sea surface and motion time histories to further examine the buoy RAO. The harmonic spectrum, which displays the power spectral density (PSD) of selected frequencies, is presented in the right plots of Figure. 29 to Figure. 33. The time duration used for harmonic spectrum analysis is determined based on the desired fundamental frequency. For example, in terms of a wave period of 7 seconds, the motion response at 0.142 Hz is to be captured. Therefore, the used time duration is determined to be 84 seconds with a corresponding fundamental frequency of 0.0119 Hz. The 0.143 Hz is the 12th harmonic in the spectrum. Regarding the wave periods of 8.5, 10.5, 12.5, and 14.5 seconds, the corresponding frequency is 0.118, 0.095, 0.08, and 0.069 Hz, respectively. The fundamental frequency is 0.0118, 0.0119, 0.0114, and 0.0115 Hz, respectively. The associated time duration used for spectrum analysis is 85, 84, 87.5 and 87 seconds, respectively. The spectrum plots show that the ramp-up stage passed after 20 seconds; therefore, the last 90 seconds of the time domain motion data proves suitable for the harmonic spectrum analysis.

In terms of waves with a period of 7 seconds, the spectrum in Figure. 29 indicates that all four spectra had their highest peaks at a frequency of about 0.143 Hz, equivalent

to the period of 7 seconds, meaning that the main responses of surge, heave, and pitch are aligned with the wave frequency. The main response occurs at the 12th harmonic. Figure. 30 shows that the four spectra when the wave period is 8.5 seconds have their highest peaks at the frequency of 0.118 Hz, and the primary response is captured at the 10th harmonic. Turning to the wave periods of 10.5, 12.5, and 14.5 seconds, Figure. 31, Figure. 32, and Figure. 33 reveal that the four spectra have their highest peaks at the frequencies of 0.095 Hz (period of 10.5 seconds), 0.080 Hz (period of 12.5 seconds), and 0.069 Hz (period of 14.5 seconds), which are at the 8th, 7th, and 6th harmonics at the corresponding harmonic spectrum, respectively. It is concluded that for all wave periods, the primary response frequencies of surge, heave, and pitch motion are all identical to the wave frequency.
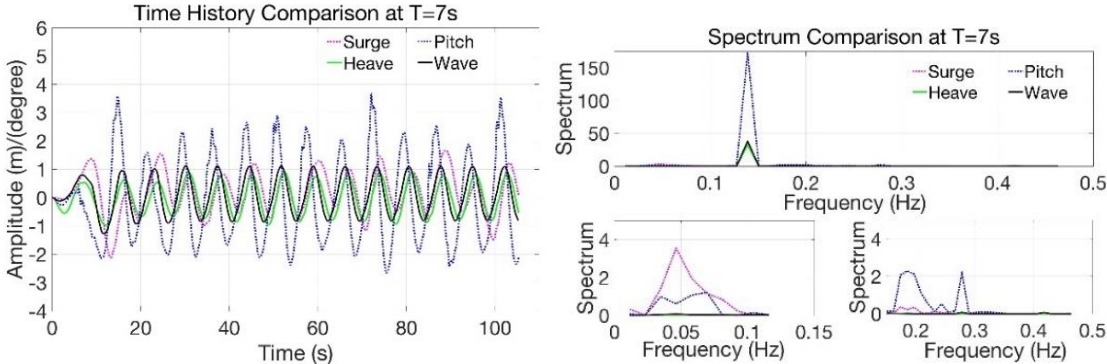
Figure. 29 Simulated motion time histories and spectrum, T=7s.
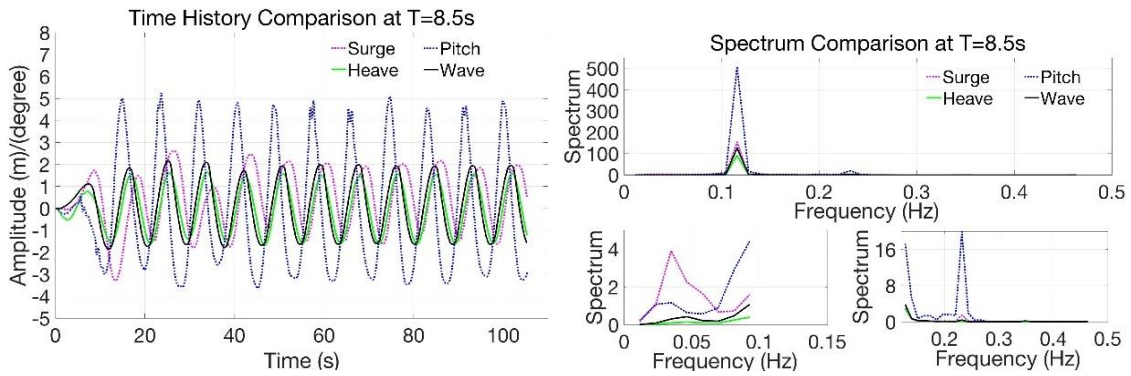
Figure. 30 Simulated motion time histories and spectrum, T=8.5s.
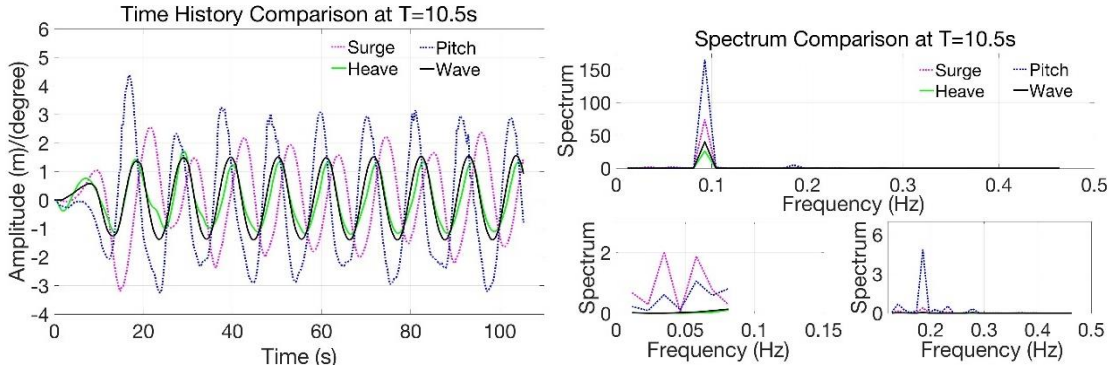
Figure. 31 Simulated motion time histories and spectrum, T=10.5s.
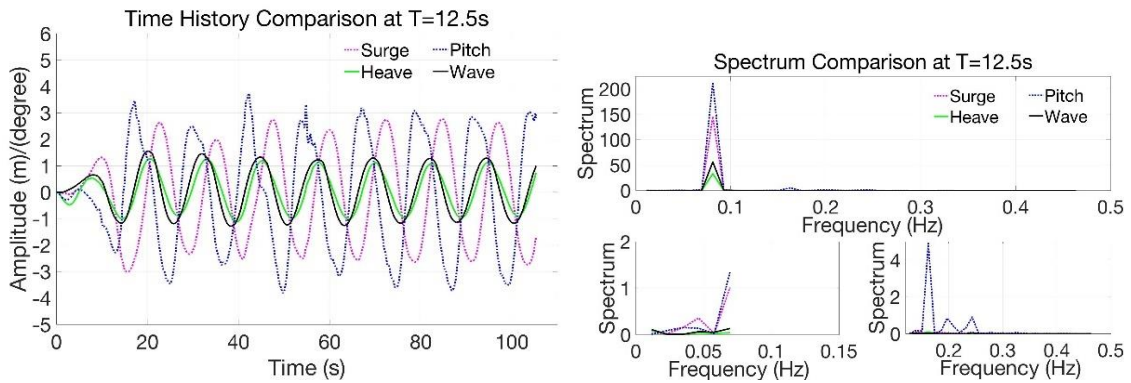
Figure. 32 Simulated motion time histories and spectrum, T=12.5s.
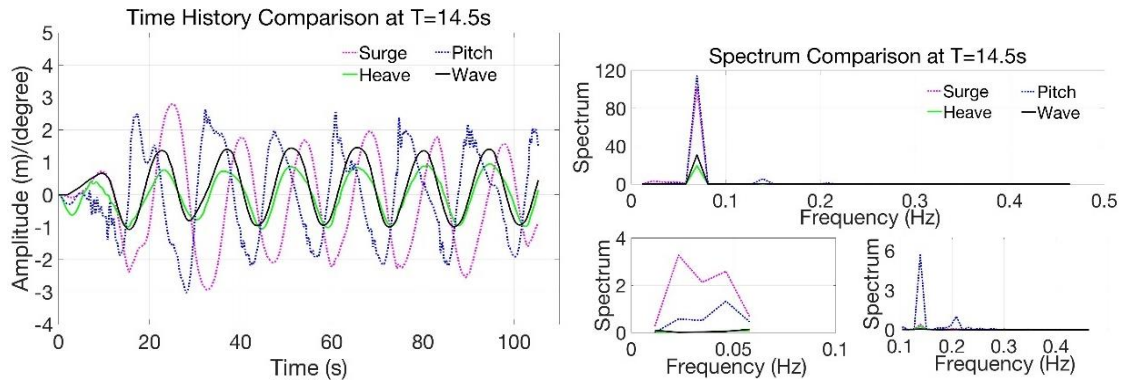
Figure. 33 Simulated motion time histories and spectrum, T=14.5s.

However, besides the central highest peak for the spectra of surge, heave, and pitch, there are some other low peaks for all five wave periods. The local areas of the spectrum to the left and the right of the main peak are enlarged, and the enlarged small peaks are presented under the primary spectrum figures. The motion subcomponents implied by these small peaks at certain frequencies probably contribute to the irregularity of the motion time histories.

First, observations are carried out for the surge spectra for all five cases. In all the surge spectra, the leftmost peaks located around 0.05 Hz represent the surge natural period of the buoy, 20.5 seconds. Turning to the pitch spectrum, the peaks at around 0.05 Hz also exist for all five periods, indicating the coupling effects from surge motion. The motion component at the surge natural frequency is identified in the surge and pitch. The chaotic vortex forming alternately on both sides of the buoy due to the oscillatory flow might have triggered the surge motion at its natural frequency.

Second, the pitch spectra for the five cases are investigated. For all five wave periods, pitch spectra exhibit the most peaks. The phenomenon is also reflected in the five

91

pitch motion time histories, which are characterized by a higher degree of irregularity than surge and heave. Besides the leftmost peaks corresponding to surge natural frequency and the highest peak at wave frequencies, several peaks are situated at higher frequencies for all five cases, most of which correspond to the pitch natural frequency of 0.208 Hz and the heave natural frequency of 0.147 Hz. Peaks at the frequency of twice the wave frequency are sometimes distinguished, indicating motion excited at twice the wave frequency.

For instance, in terms of the pitch spectrum at a period of 7 seconds, shown in Figure. 29, another several peaks located around 0.2 Hz approximately correspond to the pitch natural frequency of 0.208 Hz. Additionally, there is a peak at around 0.28 Hz (two times the wave frequency), implying the motion component excited at twice the wave frequency. In the case of the pitch spectrum at a period of 8.5 seconds, shown in Figure. 30, the peak located from 0.23 to 0.24 Hz is twice the wave frequency of 0.118 Hz. Also, some small peaks are observed from 0.14 to 0.15 Hz, agreeing with the heave natural frequency of 0.147 Hz. Regarding the pitch spectrum with a period of 10.5 seconds, shown in Figure. 31, one notable peak is located at around 0.18 Hz (about twice the wave frequency of 0.095 Hz). Another small peak is observed around 0.14 Hz, indicating the heave natural frequency. Turning to the pitch spectrum at a period of 12.5 seconds, shown in Figure. 32, two notable peaks are situated at around 0.2 and 0.16 Hz, agreeing with the pitch natural frequency and the doubling of wave frequency, respectively. Finally, the pitch spectrum at a period of 14.5 seconds, shown in Figure. 33, include several peaks

92

located at 0.14 Hz and in the range of 0.18 to 0.21 Hz, correlating with twice the wave frequency and the pitch natural frequency.

Third, turning to the heave spectra, the peaks other than the highest peak at the wave frequency are not conspicuous for most of the wave periods. The time histories of heave motion manifest the relatively regular pattern with the period identical to the incoming waves.

In summary, the harmonic spectrum analyses demonstrate that not only is the response at the wave frequency excited, but the response at the natural frequencies of surge, heave, and pitch are also identified. The motion subcomponents at frequencies other than the wave frequency probably lead to the irregularity of the motion time histories. Coupling effects of surge and heave natural frequencies are noticeable, especially for the pitch motion. Coupling effects from pitch motion are also observed in motions in other directions.

5.4.3 Simulated RAOs and Validations

The RAOs of the coupled CFD-mooring analysis at the associated wave frequencies are calculated and are summarized in Table 8. The table includes the model test results and numerical simulation results of Ryu et al. (2006) based on diffraction/radiation methodologies. If multiple model tests were performed at certain periods, their results are included within the same cell in Table 8. The experimental heave RAO for the period of 12.5 seconds and the experimental surge, heave, and pitch RAO for the period of 14.5 seconds were not provided. Therefore, the RAO for the closest periods

are adopted for comparison, with their periods specified within the bracket after the specified RAO. Figure. 34, Figure. 35, and Figure. 36 compare various sets of data for the surge, heave, and pitch RAOs, respectively.

Generally, the surge RAO obtained from the coupled CFD-mooring analysis agrees well with the experiments and the previous simulations when the wave period is less than 10.5 seconds, as shown in Figure. 34. In terms of long waves with periods of 12.5 and 14.5 seconds, the numerical simulation results based on diffraction theory appeared 10% to 30% larger than model tests. The surge RAO obtained by the coupled analysis appear close to the model tests, especially for the period of 12.5 seconds. Even though the model test surge RAO for the period of 14.5 seconds was not supplied, the simulated RAO of the coupled analysis is close to and slightly larger than the experimental surge RAO for the period of 14 seconds. All datasets indicate that surge RAO increase as wave period increase. The simulation results of coupled analysis appear closer to model tests than the numerical results based on diffraction theory.

Turning to the heave RAOs displayed in Figure. 35, the experimental heave RAOs appear larger than the numerical results obtained by Ryu et al. (2006). The skirt contributes to an approximately 3% to 8% reduction in the heave RAO. The heave RAOs of the coupled analysis agree well with the model tests with a minimal difference of 2% for periods of 7 and 8.5 seconds. Two experiments are implemented by Ryu et al. (2006) at a period of 10.5 seconds, and the corresponding simulated RAO match with the smaller test result. Though heave RAO at the period of 12.5 seconds is not available, the simulated RAO of the coupled analysis is compared to those of adjacent periods. The results appear

approximately 5% smaller than the model tests for periods of 12 and 13 seconds. Nevertheless, two experiments conducted at the period of 12 seconds lead to heave RAOs of 0.86 and 0.66, manifesting a 25% discrepancy and implying the uncertainty of model tests of long waves. Finally, the simulated heave RAO of the coupled analysis when the period is 14.5 seconds is about 5% smaller than the numerically simulated RAOs of Ryu et al. (2006). The deviation is reasonable considering the large variance of heave RAO drawn from experiments for long waves. The heave RAO comparison shows the results from the coupled analysis being closer to the model tests than numerical results based on diffraction theory.
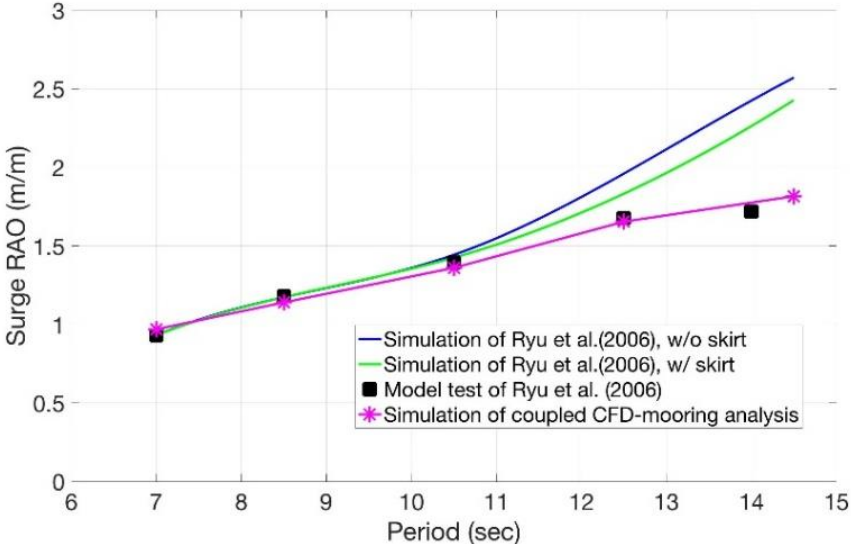

Figure. 34 Surge RAO comparison of Buoy #2
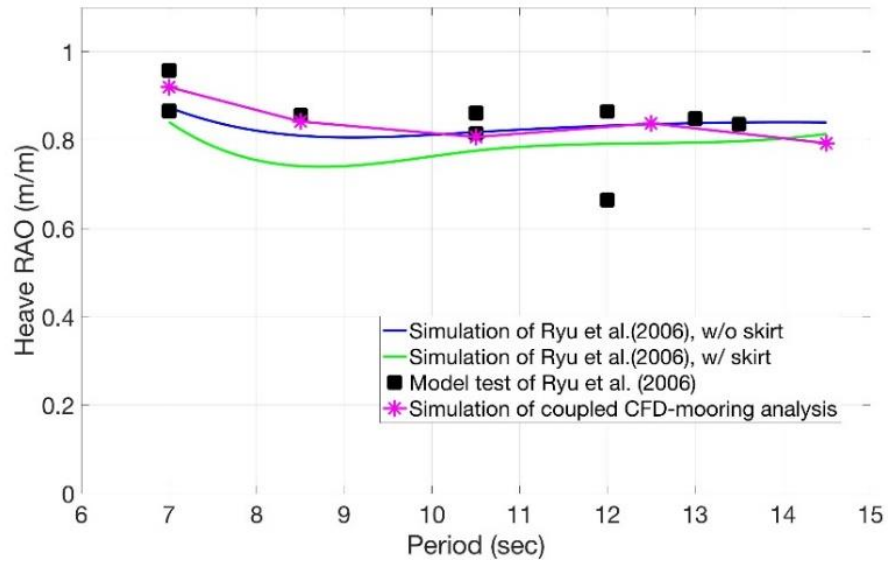
Figure. 35 Heave RAO comparison of Buoy #2
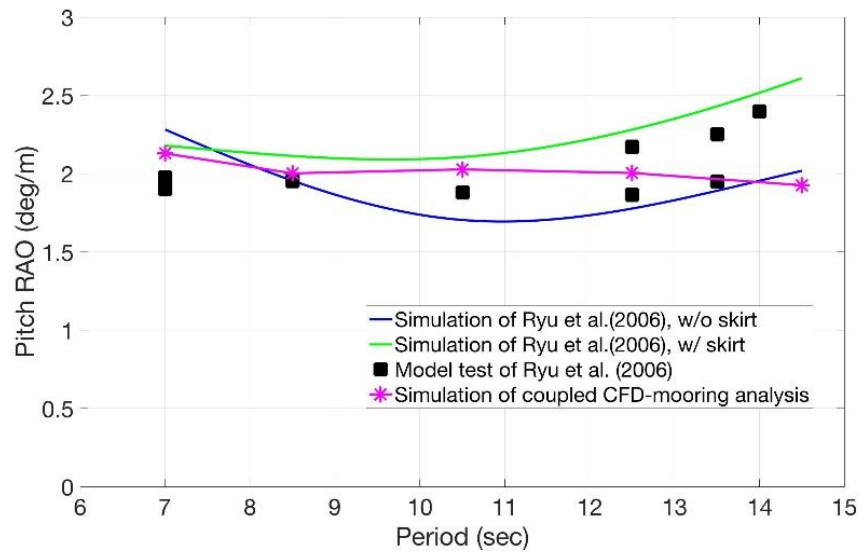
Figure. 36 Pitch RAO comparison of Buoy #2

Regarding the pitch RAOs in Figure. 36, the simulation results by Ryu et al. (2006) indicate that the pitch RAO with the skirt appears larger than that without the skirt for most of the wave periods. The experimental pitch RAOs lie in the region enclosed by the two curves of numerical simulations, as shown in Figure. 36. The pitch RAOs acquired by the coupled analysis agree well with the model tests for periods of 7, 8.5, and 10.5 seconds and are closer to the model test results than the previous numerical analysis. When the incoming wave has a period of 12.5 seconds, two sets of experiments are conducted to obtain experimental pitch RAOs of 2.17 and 1.87, with a rough difference of 16%. The pitch RAO of the coupled analysis is between them. Turning to the period of 14.5 seconds, the coupled analysis reaches an 8% smaller pitch RAO than the diffraction-based simulation without the skirt. For long waves with periods of 13.5 seconds, the experimental results show an approximate variance of 15% between the two datasets. The discrepancy implies the uncertainty of testing pitch RAOs in long waves. Even though pitch RAO for 14.5 seconds is not provided, the coupled analysis pitch RAO is still close to the experimental pitch RAO for wave period of 13.5 seconds, with a difference of 3%. Further investigation should be performed to find out why the pitch RAO experiments in long waves manifested a 15% variance.

To summarize, the coupled FANS-MOORING3D code is a powerful tool in predicting the CALM buoy's wave-induced motion with dynamic mooring interaction. The simulated RAOs agree with the model tests and appear closer to the experiments than the diffraction-based numerical simulation at periods of 7, 8.5, and 10.5 seconds. Regarding waves with periods of 12.5 and 14.5 seconds, the comparison in the surge and

heave directions indicates that the simulated RAOs agree with the model tests or diffraction-based simulation with acceptable deviation.

Table 8 Summary of Buoy #2 RAO comparison to Ryu et al. (2006)

Period	Motion	Simulated RAO w/ skirt	Model Test RAO, Ryu et., 2006	RAO w/o skirt, Ryu et., 2006	RAO w/ skirt, Ryu et., 2006
7s	Surge	0.970	0.93	0.93	0.93
	Heave	0.922	0.96/0.87	0.87	0.84
	Pitch	2.129	1.97/1.90	2.28	2.18
8.5s	Surge	1.140	1.18	1.17	1.17
	Heave	0.842	0.86	0.81	0.74
	Pitch	2.002	1.95	1.96	2.11
10.5s	Surge	1.360	1.39	1.44	1.43
	Heave	0.807	0.86/0.82	0.82	0.78
	Pitch	2.027	1.88	1.70	2.11
12.5s	Surge	1.654	1.68	1.96	1.83
	Heave	0.838	0.85 (13 s) /	0.84	0.79
	Pitch	2.004	2.17/1.87	1.78	2.28
14.5s	Surge	1.816	1.72 (14 s)	2.57	2.43
	Heave	0.793	0.84 (13.5 s)	0.84	0.81
	Pitch	1.926	2.40 (14 s)	2.02	2.61

Though the numerical simulations of Ryu et al. (2006) also showed agreement with experiments, large empirical drag coefficients were used for the analysis. The accuracy of the conventional numerical approach and validations against experiments strongly rely on the empirical estimations for drag, inertia effects, and vortex shedding. In addition, it is

not clear that whether Ryu et al. (2006) considered nonlinear effects of added mass, radiation damping, hydrostatic stiffness, and Froude-Krylov excitations that change with wetted surface.

The viscous and turbulence effects were reasonably modeled in the CFD-mooring coupled analysis and were considered a strong element to contribute to the damping effects in surge, heave, and pitch. In addition, wave loads, added-mass, hydrostatic loads, and radiation damping loads were calculated by pressure and shear force integration over the instantaneous wetted surface. The coupled FANS-MOORING3D code proves to be a powerful tool for the study of fluid-structure interaction coupled with mooring system.

5.4.4 Sensitivity Study on Skirt Inclusion

A sensitivity study for the skirt effect is conducted to investigate the effects of the skirt on motion characteristics further. Intuitively, the skirt forces more fluid to move together with the buoy while heaving and pitching, increasing the added mass and the drag force. The studies of Ryu et al. (2006) indicate that the skirt increases added mass and damping in heave and pitch directions but has limited influences on buoy RAO.

Simulations of wave-induced motion without skirt effects are additionally performed for wave periods of 7 and 12.5 seconds, representing short and long waves, respectively. Figure. 37 shows the comparison in surge, heave, and pitch directions. Figure. 37 (a) shows that the surge time histories of the two cases manifest minor discrepancies. Figure. 37 (b) suggests that heave does not show much reduction after the

skirt is included. However, the heave motion with the skirt of both periods show phase lag, which should have been caused by the increasing viscous effects. Also, the heave motion considering skirt effects appears more regular with fewer irregular fluctuations. A similar phenomenon can be identified for the pitch motion shown in Figure. 37 (c). For both wave periods, the skirt gives rise to more regular and smooth time histories.
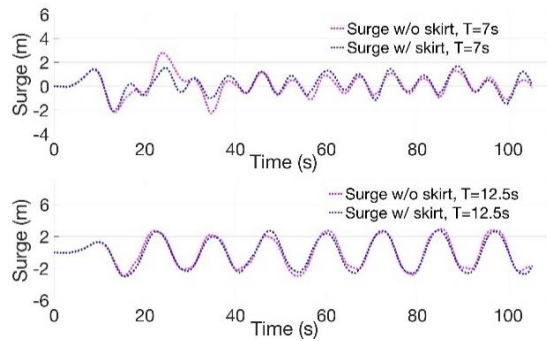
(a) Surge comparison   (b) Heave comparison
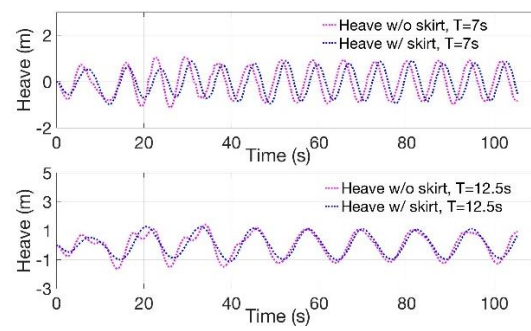
(c) Pitch comparison
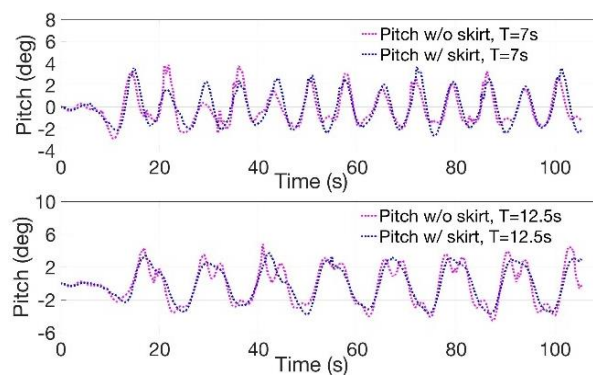
Figure. 37 Comparison of Skirt Exclusion vs Skirt Inclusion, at T=7s and T=12.5s

Harmonic spectrum analyses are conducted to investigate RAO changes due to the skirt. Figure. 38 shows the spectrum analysis results without the skirt for the two selected wave periods. As with Figure. 33 (a) and Figure. 33 (d), the primary motion responses in three directions are identified at frequencies of 0.143 and 0.08 Hz, corresponding to wave periods of 7 and 12.5 seconds, respectively.
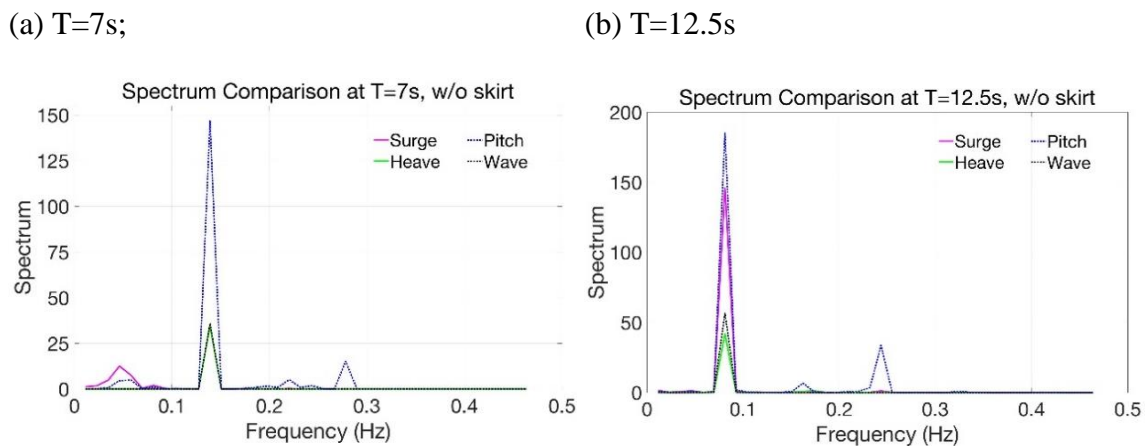
(a) T=7s;   (b) T=12.5s

Figure. 38 Harmonic spectrum analysis of motion w/o skirt. (a) T=7s; (b) T=12.5s.

Furthermore, there are some other low peaks in the spectrum other than the central highest peaks for both wave periods; these small peaks are higher than those shown in Figure. 33 (a) and Figure. 33 (d). For example, for the pitch spectra at T=12.5 seconds, one notable peak is situated at around 0.24 Hz, possibly indicating the motion at skirt-free pitch natural frequency. This peak is higher than the corresponding peak at 0.2 Hz shown in Figure. 32(d), indicating larger motion energy at a pitch natural frequency other than wave frequency. The higher peaks outside of wave frequency shown in Figure. 38 explain why motion without the skirt appeared less smooth with more irregular fluctuations. The

energy of motion subcomponents at frequencies other than wave frequency is higher than the corresponding energy of cases with the skirt because of fewer damping effects in the system.

Table 9 Summary of RAO comparison, skirt inclusion vs skirt exclusion

Period	Motion	Simulated RAO, w/o skirt	Simulated RAO w/ skirt	Percentage of change
7s	Surge	0.979	0.970	-0.92%
	Heave	0.984	0.922	-6.3%
	Pitch	2.021	2.129	5.3%
12.5s	Surge	1.652	1.654	0.12%
	Heave	0.862	0.838	-2.8%
	Pitch	1.879	2.004	6.6%

Table 9 summarizes the sensitivity of the RAO of the CALM buoy to the skirt effects. The surge RAO shows almost no change. Considering skirt effects, heave RAOs for wave periods of 7 and 12.5 seconds decrease slightly by 6.3% and 2.8%, while pitch RAOs for the two wave periods show an increase of 5.3% and 6.6%. Numerical simulations by Ryu et al. (2006) also demonstrate that for most wave periods, heave RAOs decrease while pitch RAOs increase with the skirt considered. Additionally, the RAOs still reasonably agree with the experimental results in Table 8 even without considering the skirt effects.

Though the skirt gives rise to increased added-mass and damping, the comparison of motion time histories and RAO manifests no considerable discrepancy, suggesting that

the wave-induced motion of the CALM buoy is not sensitive to skirt inclusion with the extra added-mass and increased viscous effects, probably because that the mass and cross-sectional area of the skirt is much smaller than the buoy hull. The buoy RAO should have been dominated by the buoy's inertial and viscous effects. Including the skirt seems to only alter the phase for heave and pitch motions and diminish the motion components at natural frequencies. The skirt exerts limited influence on the maximum amplitude and RAO but contributes to more regular and smooth motion time histories.

5.4.5 Full-scale Motion Verification

Full-scale simulations are implemented for the skirt-free CALM buoy system with the selected wave period of 12.5 s as an example for Froude scaling law verification. Figure. 39 displays the comparison between model-scale and full-scale simulations, in terms of wave elevation, surge, heave, and pitch motion, respectively. Figure. 39 (a) demonstrates that wave elevations from two simulations almost overlap with each other. Figure. 39 (b) indicates that the discrepancy between full scale and model scale surge motion time histories is small. Figure. 39 (c) reveals that the full-scale heave motion agrees well with the model scale, except for the minor difference in several peaks after 40 s. In Figure. 39 (d), the full-scale pitch motion exhibits a generally similar pattern with the model scale, except for the minor fluctuations from 40 s to 45 s.

(a)

Wave Elevation Comparison

(b)

Surge Motion Comparison

(c)

Heave Motion Comparison

(d)

Pitch Motion Comparison
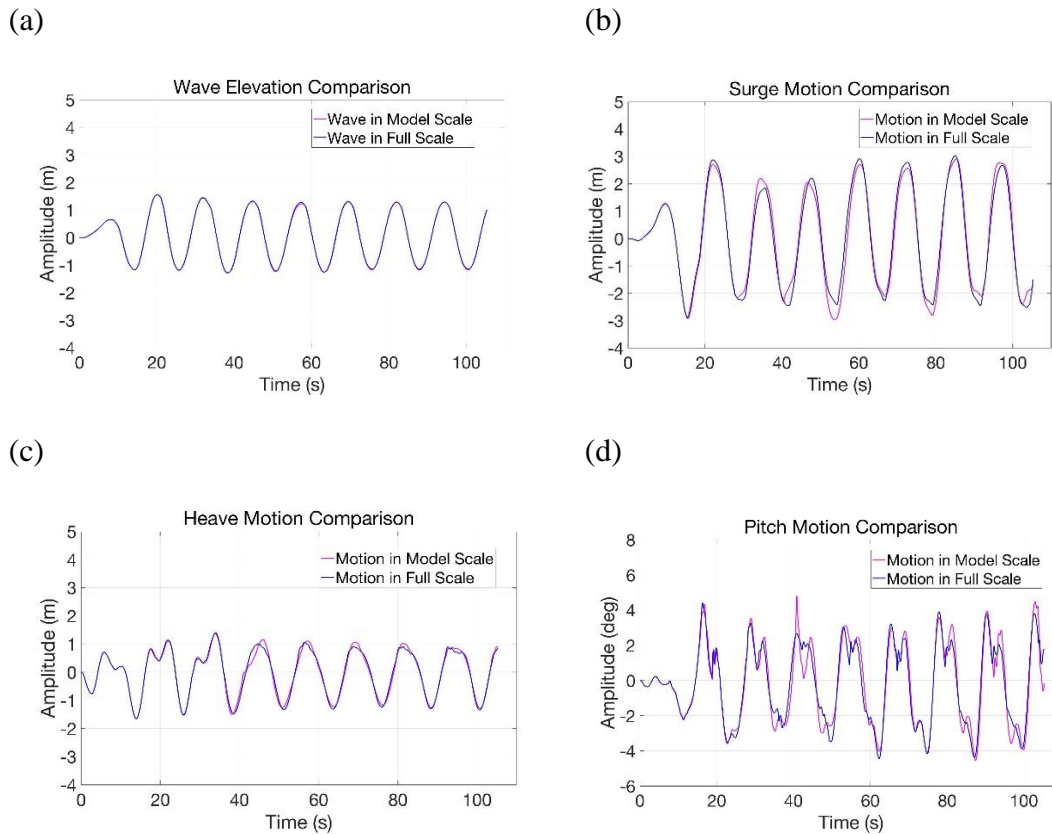
Figure. 39 Comparison of wave elevation and motion between model- and full-scale

Also, the flow momentum field at the depth of z/D=-0.2 around the buoy are extracted at both the time of wave crest and wave trough, which are at the time step of 800 and 1000, respectively. The full-scale momentum is compared against the scenarios at the same location and time of the model-scale simulation. Figure. 40 demonstrates that the momentum fields at both wave crest and trough are similar to those of the model-scale simulation. The detailed fluid field analysis is presented in Section 3.3.1.

Therefore, the comparison demonstrates that simulations from the model and prototype scale manifest minimal discrepancy in the aspects of motion and general flow

pattern, verifying the Froude scaling law in terms of the wave-induced motion of the CALM buoy system.

(a) Flow momentum field during wave crest, full-scale vs model-scale

(b) Flow momentum during wave trough, full-scale vs model-scale

Figure. 40 Comparison of flow momentum field between full and model scale

5.5 Wave-Current-Body Interaction of Buoy #2

The wave-current-body interaction of the CALM buoy #2 is modeled using the same methodology. The simulated RAO in currents are compared with experimental RAO measurements of Ryu et al. (2006). Sway, roll, and yaw motions are also investigated.

5.5.1 Motion Comparison and RAO Validations

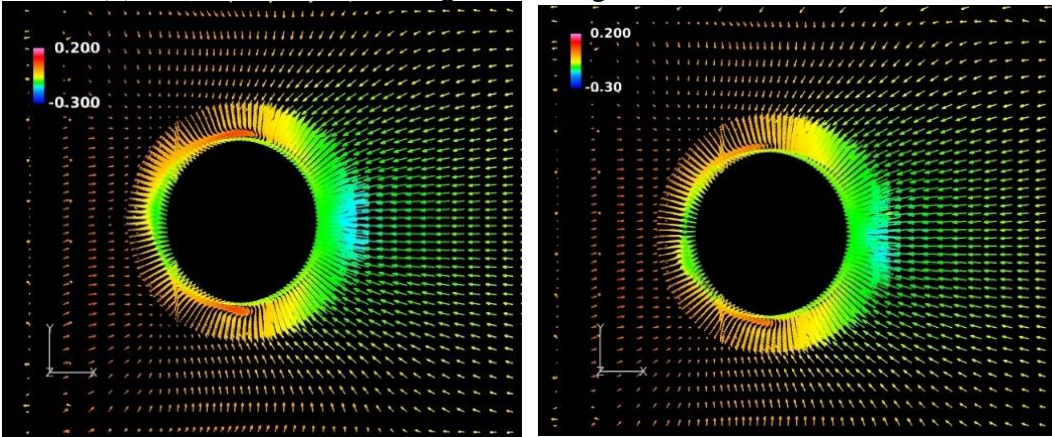When waves propagate in a current, the encounter period of the wave encountering a floating body is different from the waves' intrinsic frequency, which determines the wavelength and the wave kinematics. If the wave shares the same propagating direction with the current direction, the encounter frequency tends to be higher than the wave frequency. The two frequencies are related by Doppler shift as:

$$\omega = \omega_A - kU$$

where $\omega_A = 2\pi/T_A$, and T_A is the encounter period seen by an observer in the fixed coordinate.

A fixed or floating stationary structure in a wave field with current responds to the encounter period rather than to the intrinsic period. The wave frequency spectrum should be transformed into the encounter frequency for wave response calculations.

Three cases are simulated in this study with their simulation parameters displayed in Table 10 to investigate the buoy response under the combined wave-current condition. The RAOs at periods of 8.5, 10.5, and 12.5 seconds were available in the model tests performed by Ryu et al. (2006). The intrinsic periods are taken as 10.5, 12.5, and 13.5 seconds. The current speed is determined so that the encounter periods are 8.5, 10.5, and

12.5 seconds after Doppler transformation, respectively. Therefore, for the first case for example, even though the original wave period is 10.5 seconds, the encounter period seen by the buoy is 8.5 seconds, and the buoy responds to the period of 8.5 seconds. Theoretically, the RAO at the Case #1 should be closer to the experimental RAO of the period of 8.5 seconds rather than the period of 10.5 seconds.

Table 10. Simulation parameters of combined wave-current conditions

Case #	Intrinsic period	Current speed	Encounter period
#1	10.5 seconds	4.25 m/s (0.33)	8.5 seconds
#2	12.5 seconds	3.10 m/s (0.24)	10.5 seconds
#3	13.5 seconds	1.64 m/s (0.13)	12.5 seconds

Figure. 41, Figure. 42, and Figure. 43 show the time histories of sea elevation, surge, heave, and pitch motion for the Case #1, #2, and #3 when the encounter periods are 8.5, 10.5, and 12.5 seconds, respectively. All three figures show that the motion time histories appear to be in the encounter periods. The heave motion seems not affected by the current effects. The surge motion manifests an offset to the equivalent position, and the pitch motion appears to have a mean tilting angle. The mean surging offset and tilting angle increase as current speed increased. For example, the average offset of Case #1 shown in Figure. 41 is about 3.5 meters, and the average offset of Case #2 shown in Figure. 42 is about 1.8 m, smaller than Case #1. The average tilting angle of Case #1 is higher than that of Case #2 and #3 due to higher current speed. Case #2 and #3 manifest more

regular and smooth motion time histories than Case #1, probably due to the reducing
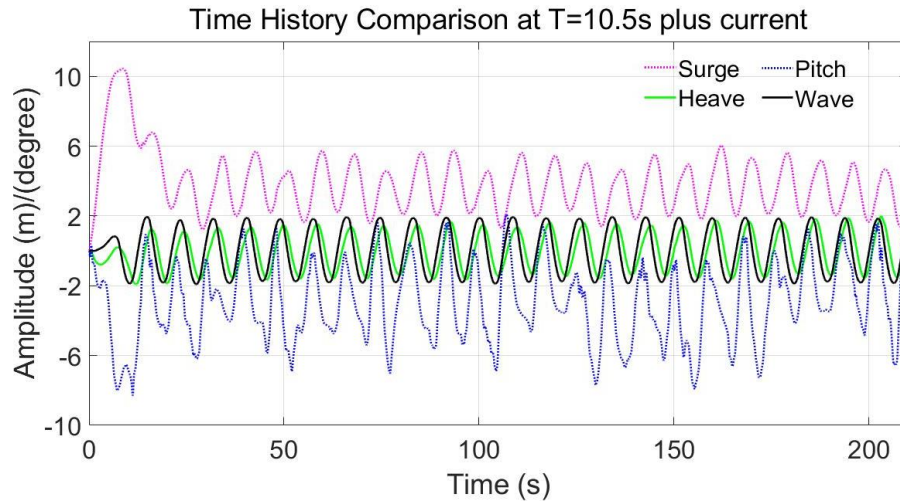
current speed and turbulence strength.

Figure. 41 Case #1 with intrinsic period of 10.5s and encounter period of 8.5s.
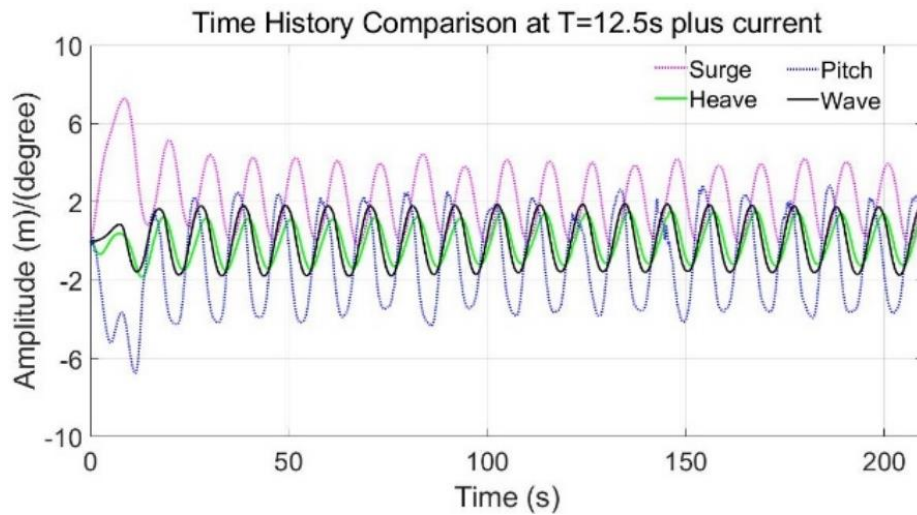
Figure. 42 Case #2 with intrinsic period of 12.5s and encounter period of 10.5s
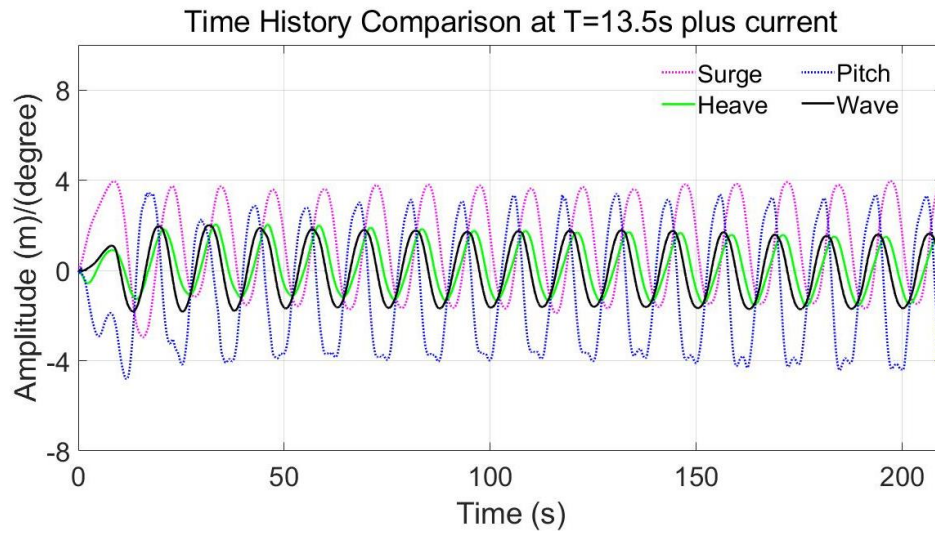
Figure. 43 Case #3 with intrinsic period of 13.5s and encounter period of 12.5s

Harmonic spectrum analysis is conducted to calculate RAOs of three cases. The left and the right plots of Figure. 44 show the spectrum analysis results of Case #1 and #2, respectively. The two cases show that the motions in surge, heave, and pitch are excited at the wave frequencies, which are 0.118 and 0.095 Hz, respectively. More small peaks are identified other than the main peak at wave frequency for the spectrum of Case #1. The pitch natural frequency of the system is around 0.21 Hz in accordance with Ryu et al. (2005). The small peaks are in the adjacent areas of the 0.2 Hz, implying that there are motion subcomponents at around pitch natural frequency. The motion represented by these small peaks is likely to be caused by strong vortex formation due to the wave-current-body interaction, contributing to the irregular pattern of pitch motion of Case #1 as shown in Figure. 41. The spectrum of Case #2 other than the primary peak appear flatter than that of Case #1, indicating fewer motion subcomponents excited and more regular and smooth motion time histories as shown in Figure. 42.
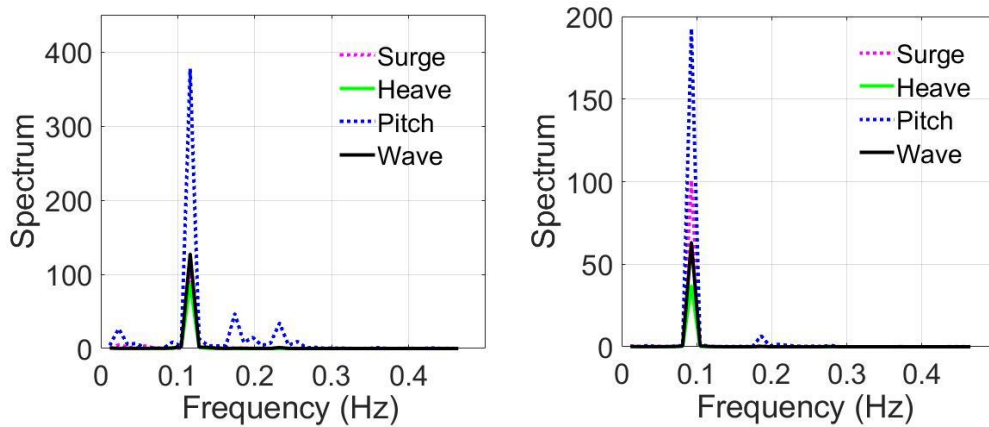
Figure. 44 Spectrum analysis results (a) Case#1; (b) Case #2

Since the time histories of Case #1 manifest higher degrees of irregularity, the RAOs are calculated based on the two approaches and are summarized in Table 11 along with RAOs measured by Ryu et al. (2006). It is expected that the RAO results should be corresponding to the encounter period rather than the original period.

RAOs of all cases agree well with experiments with minor difference. Since the motion time histories of Case #1 manifest irregularity, RAOs from spectrum analysis and SD calculation approach manifest a 15% difference in surge and pitch directions. Though RAOs from spectrum analysis appeared to be smaller than experiments, RAOs from SD calculation match well with experiments with a difference of at most 6%. In terms of Case #2 and #3, RAOs from two approaches are close and appear slightly smaller than experiments with around 2% to 6%. The agreement between coupled analysis and experiments indicates that the coupled FANS-MOORING3D program predicts well the buoy RAO in omni-directional combined wave-current conditions.

Table 11. RAO comparison of Buoy #2 in currents

	Motion	RAO (Spectrum)	RAO (SD)	Model Test by Ryu et al. (2005)*
Case #1: Encounter period 8.5s (intrinsic 10.5s)	Surge	0.895253	1.1075	1.18 (8.5s)
	Heave	0.824855	0.8090	0.86 (8.5s)
	Pitch	1.719921	2.0277	1.95 (8.5s)
Case #2: Encounter period 10.5s (intrinsic 12.5s)	Surge	1.263301	1.3689	1.39 (10.5s)
	Heave	0.76352	0.7637	0.86/0.82 (10.5s)
	Pitch	1.747193	1.7553	1.88 (10.5s)
Case #3: Encounter period 12.5s (intrinsic 13.5s)	Surge	1.611	1.617	1.68 (12.5s)
	Heave	0.858	0.862	0.85 (13 s) / 0.87 (12 s) / 0.67 (12 s)
	Pitch	2.183	2.181	2.17/1.87 (12.5s)
*Note: periods of tests are specified in the bracket.				

Currents exert slight influences on Spar RAOs in accordance with measurements performed by Kurian et al. (2012). For frequencies lower than 0.15 Hz, the surge, heave, and pitch RAOs of a truss Spar slightly reduce when current velocity increases. The trend is consistent with our observations on the CALM buoy that RAOs with currents are generally slightly smaller than experiments. However, limited research is available in the existing literature review for the buoy RAO when currents coexist. More comprehensive studies can be performed to unveil how currents affected buoy's wave-induced motion in more complicated wave-current combined conditions.

5.5.2 Six-DoF Simulations and Discussion

Sway, roll, and yaw motions are also investigated. These three DoFs are often neglected in the potential flow approach. However, CFD captures the vortex shedding formation and the corresponding VIM, which might be significant in sway, roll, and yaw directions. The corresponding current-only conditions for Case #1 and #2 are additionally considered to provide insights on how the current affects the wave-induced motion in terms of sway, roll, and yaw. The wave's influences on VIM are investigated.

Figure. 45 (a), (b), and (c) show the comparison of sway, roll, and yaw motion time histories, respectively, between current-only condition and combined current-wave condition. The upper and lower plots of each sub-figures correspond to Case #1 and #2 respectively. The VIM of the buoy is characterized by considerable transverse motion, which is observed in Figure. 45 (a). The SD of the sway in current-only condition is 0.88 m and 0.51 m for Case #1 and #2, which reduce to 0.33m and 0.36m with consideration of waves. The presence of waves seems to diminish the sway amplitudes considerably for both Case #1 and #2. The wave heights of the two cases are roughly 4 meters, larger than the typical operational conditions in typical sea-state scatter diagram but smaller than extreme conditions of storm events with significant wave height being as high as over 10 meters.

The VIM response shows significant reductions or even disappears in large waves (100 year or Hurricane waves) in accordance with Hong et al. (2008) and Goncalves et al. (2013). However, the reduction in VIM response is negligible in small waves as found in operational seas according to Martin et al. (2012) and Koop and Wilde (2016). The

selected wave heights lie between small waves and extreme large waves. Therefore, the VIM amplitudes show reductions of about 50%, but the transverse amplitudes of combined wave-current condition do not disappear and still show SD of around 0.35m.

(a) Sway

(b) Roll
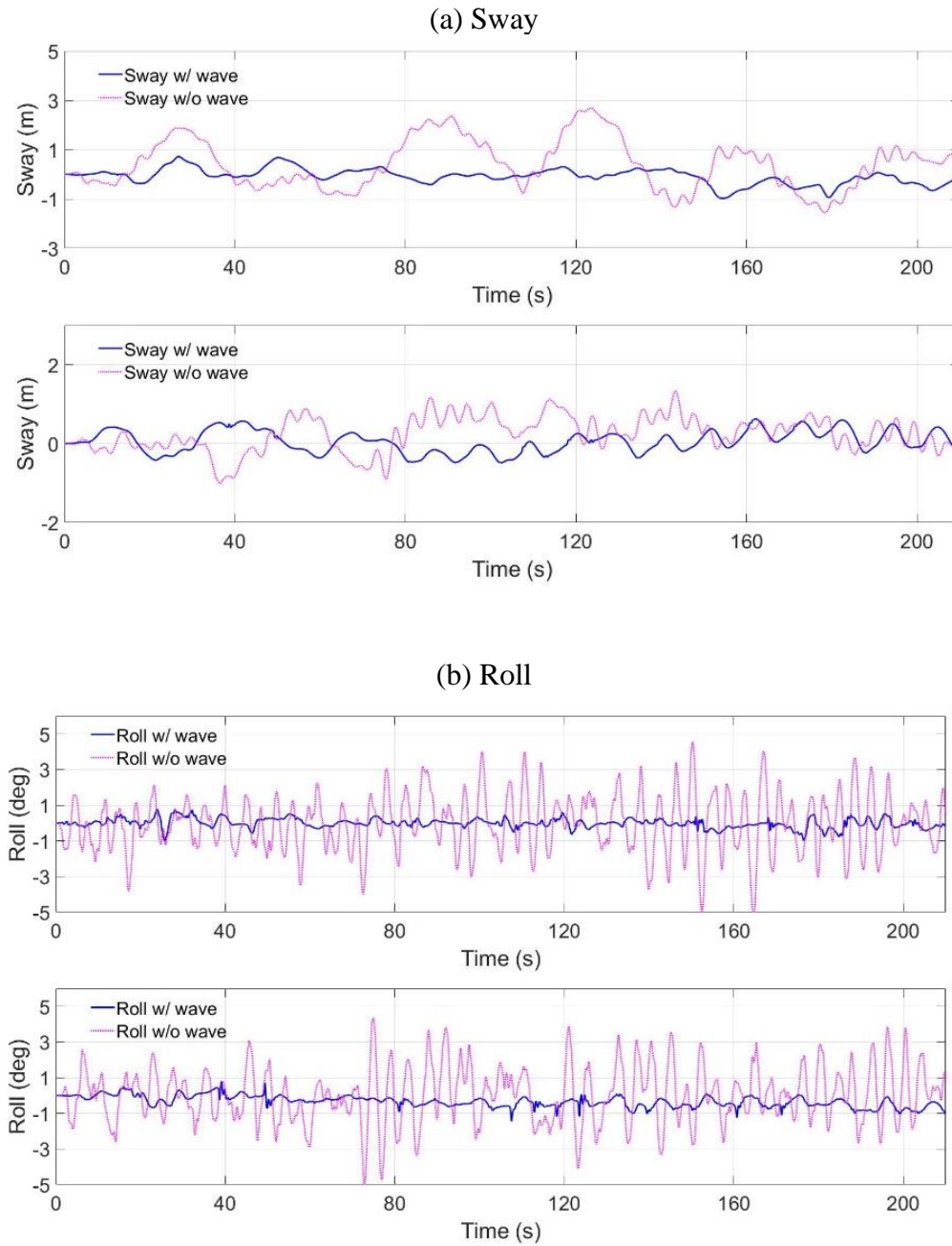
Figure. 45 Comparison of motion in sway, roll, and yaw.
Upper: Case #1; lower: Case #2.

(c) Yaw
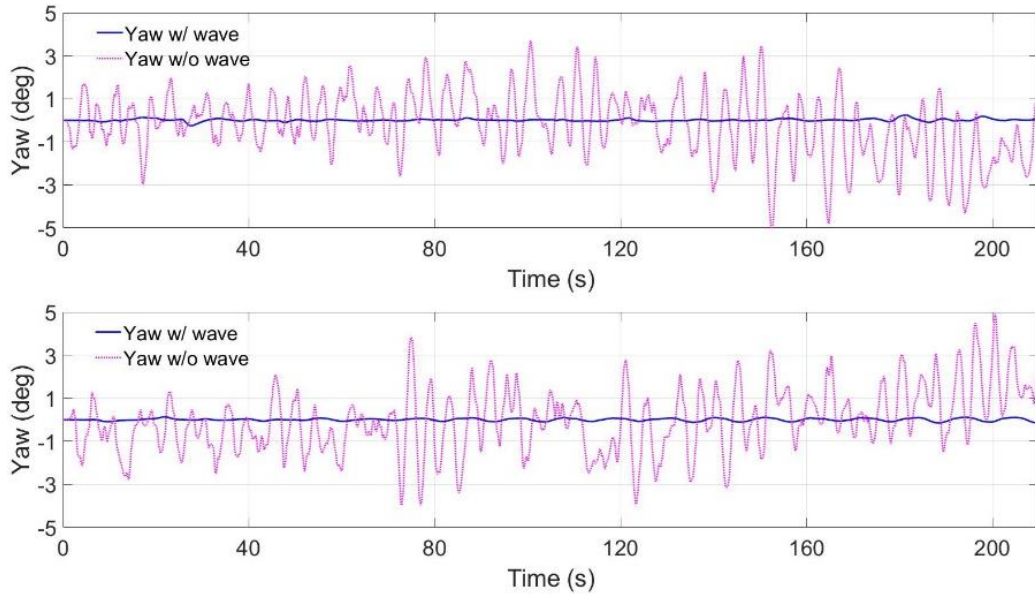
**Figure. 45 (Continued) Comparison of motion in sway, roll, and yaw.
Upper: Case #1; lower: Case #2.**

The sway motion is induced by vortex forming periodically on transverse sides of the buoy. Roll motion is also affected by the vortex shedding formation. Figure. 45 (b) indicates that the roll SDs in current-only conditions are 1.76° and 1.68° for Case #1 and #2 but are decreased to 0.27° and 0.31° under the influences of waves. Figure. 45 (c) shows the yaw SDs in current-only conditions are 1.61° and 1.52° for Case #1 and #2 and are decreased to less than 0.2° with waves.

The simulations indicate that roll and yaw motions are also significant in current-only conditions of both cases with maximum tilting angle to be around 4°-5°. The reduction of roll and yaw motion is considerable with the presence of large waves, and the reduction ratio is more conspicuous than sway motion.

114
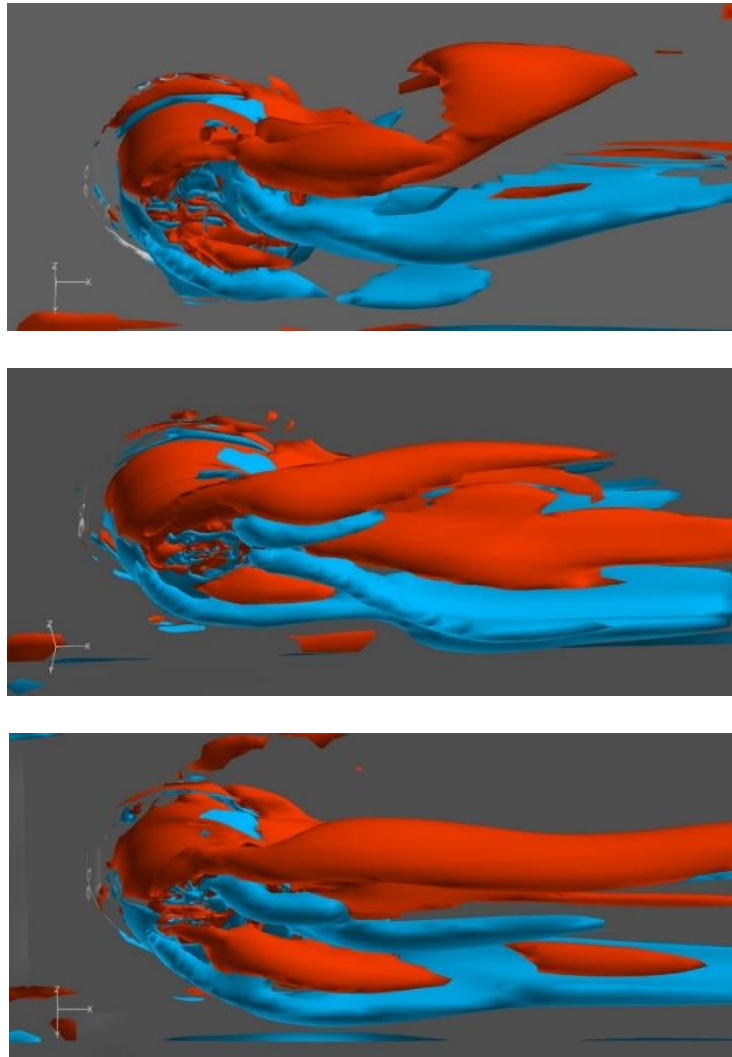
**Figure. 46 3-D vorticity of current-only condition, Case #1
(top to bottom: 6000th, 7000th, and 8000th step)**

Figure. 46 shows the 3D snapshots of the 6000th, 7000th, and 8000th time step of

the Case #1, demonstrating how vorticity evolved in the current-only condition. The

vorticity is normalized by the characteristic length and velocity. The considerable vortex

causes pressure difference between the two sides, exciting the transverse motion. The

vorticity stretches are long. All these vorticity contours show a lot of violent swirls, an

indication of large transverse motions. The vortex at the bottom of the buoy should be relevant to the VIM in the roll direction.

More details can be found in Figure. 47 and Figure. 48, which show the vorticity evolvement in the cutting plane of z=-0.2 of Case #1 and Case #2, respectively. The left plots show the current-only condition, and the right plots show the combined wave-current condition. The vorticity of the current-only condition seems swaying as time progressed, indicating the large transverse motion.

Figure. 47 Comparison of vorticity, current only vs current-wave combined conditions, Case #1 (left: current-only; right: current-wave combination)

In contrast, the vorticity pattern of the combined current-wave condition seems straighter than the current-only condition. The vortex swaying is not considerable in the right plots, implying that the transverse motion is reduced due to the wave effects. However, the vortex length is neither shortened nor prolonged conspicuously due to the wave effects, indicating that the wave exerts limited influences on the vorticity strength. The wave-induced water particle velocity is low compared to the current speed.
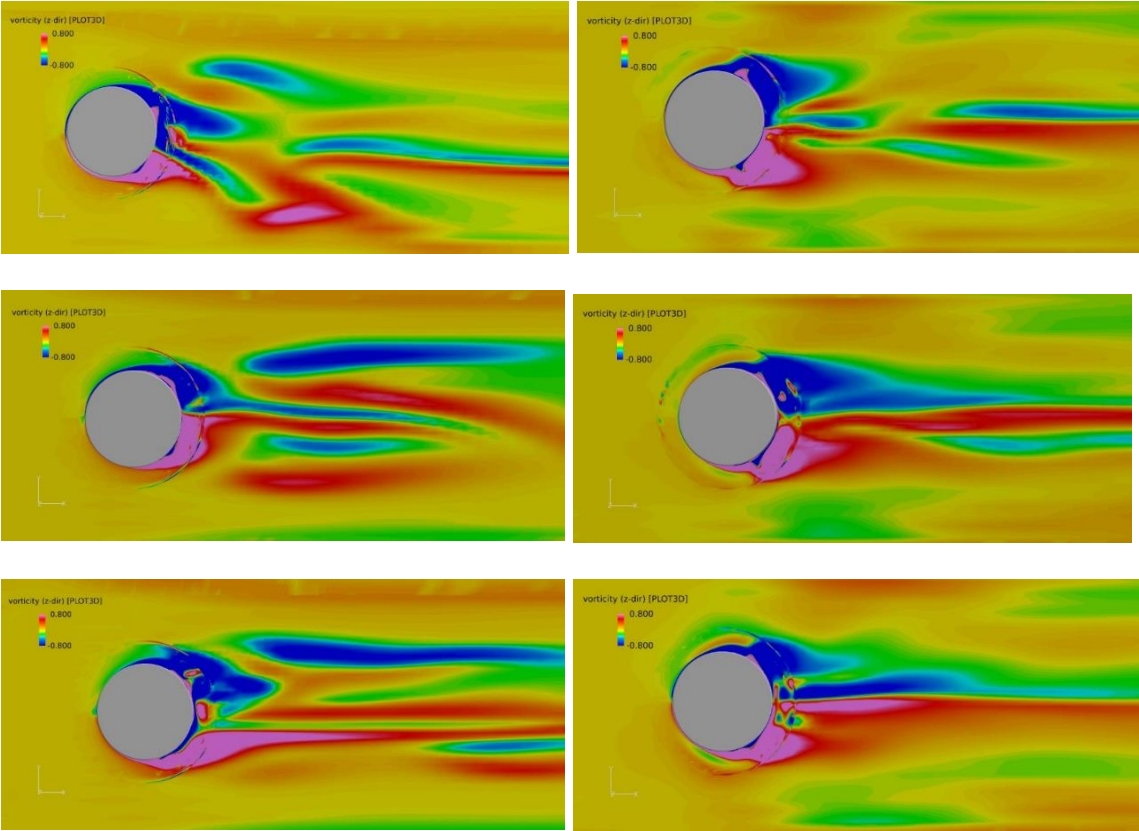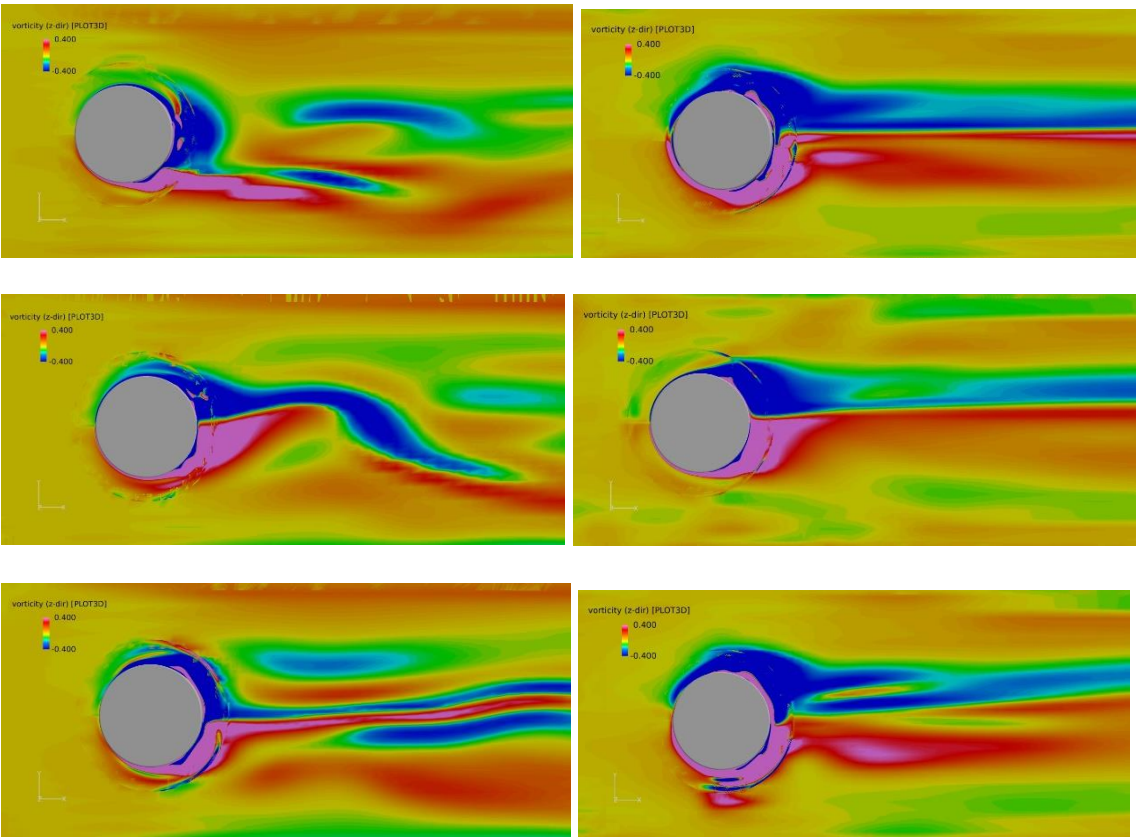

Figure. 48 Comparison of vorticity, current only vs current-wave combined conditions, Case #2; (left: current-only; right: current-wave combination)

5.6 Summary

The MOORING3D program and the six-DoF motion solver are coupled with the FANS CFD module incorporating the level-set method and LES model. The CALM buoy #1 and #2 are modeled in model scale. The mooring systems of both buoys are modeled by the MOORING3D program in full scale. The wave-induced motion simulation is achieved through the coupled codes.

In terms of Buoy #1, the wave-induced responses are analyzed by generating various sets of regular waves, including 8.5, 9.2, 10.5, 11.5, and 12.5 seconds. Both harmonic spectrum analysis and SD approach are used to investigate the RAOs, which are compared against the RAOs of AQWA-Orcaflex integrated model. The RAOs of spectrum analysis and SD approach manifest discrepancies due to motion subcomponents at other than wave frequency. Generally, the RAOs of the coupled analysis are smaller than AQWA-Orcaflex results in surge and heave and are bigger than AQWA-Orcaflex in pitch. The trend is consistent with studies performed by Woodburn et al. (2005), in which AQWA predictions over-estimate the surge and heave RAOs and under-estimate the pitch RAOs comparing to experiments. The ratio of change from AQWA-Orcaflex to CFD generally agree with experiments presented by Woodburn et al. (2005). The comparison indicates that the viscous and turbulence effects induced by the buoy are considerable in reducing motion in surge and heave. The diffraction analysis cannot predict well the wave excitation moments in pitch. The accuracy of motion prediction relies highly on how drag coefficients and vortex shedding effects are estimated empirically, which adds uncertainty for the simulations.

In terms of Buoy #2, the harmonic spectrum analyses unveil the RAOs which are validated against experiments of Ryu et al. (2006). The motion components at other frequencies are much lower than that of Buoy #1, therefore only spectrum analysis is needed. The simulated surge, heave, and pitch RAOs agree well with the model tests. The coupled CFD-mooring analysis results manifest closer to the model tests than previous numerical simulations, which also used high empirical drag coefficients to match with model tests. The skirt sensitivity study reveals the buoy's wave-induced motion to not be sensitive to skirt inclusion, suggesting the responses appearing to be dominated by the inertial and viscous effects of the buoy hull. The additional added-mass and viscous effects of the skirt seem only slightly affecting the RAOs. The viscous effects of the skirt seem limited due to its small cross-sectional area. However, the skirt proves beneficial in smoothing the motion and reducing irregular fluctuations.

In terms of the wave-current-body interaction of Buoy #2, the Doppler effect is captured, and the RAOs of encounter period of 8.5-,10.5-, and 12.5- seconds match well with experimental measurements. VIM in sway, roll, and yaw directions is identified when currents exist due to strong vortex formation modeled with the LES. However, the waves diminish the VIM amplitudes in sway, roll, and yaw considerably, agreeing well with the previous field measurements that the presence of waves can significantly reduce VIM amplitudes.

The CFD-mooring coupled method is demonstrated to be a powerful tool in assessing the wave-induced motion and dynamic interaction between the floating body and its mooring system. Additionally, the coupled method manifests its advantages in

119

many challenging scenarios that cannot be addressed by potential flow approaches, especially in the aspects of viscous effects modeling, vortex formation, complicated free surface effects, etc. The coupled FANS-MOORING3D code represents a feasible solution for motion prediction of moored floating systems exposed to highly complicated working conditions.

CHAPTER VI

VIM SIMULATION FOR SEMI-SUBMERSIBLE PLATFORMS[*]

6.1 Introduction

This chapter describes the VIM simulations of a semi-submersible moored by a semi-taut chain-rope-chain mooring system. Section 6.2 describes the CFD model of the semi-submersible. Section 6.3 presents the mooring systems with different damping levels that are to be used for investigation. Section 6.4 presents the VIM results of damping-free simulations and validation against experiments. Section 6.5 and 6.6 discuss the influence of mooring system on the VIM amplitudes.

6.2 Model and Grid System

The deep draft semi-submersible of four-square columns and four pontoons used by Waals et al. (2007) is selected for the simulation. Major dimensions are given by Waals et al. (2007). Figure. 49 (a) shows the 3D model of the semi-submersible. Since the free surface effect is negligible in the VIM study of in-line direction and transverse direction, only the submerged part of the floater is modeled. Figure. 49 (b) illustrates the dimensions of the submerged semi-submersible in a side view sketch, where height of the submerged column H is 24.5 m, and column width L is 14 m. The column aspect ratio H/L is therefore

---

1.75 and is a major factor in VIM response. The semi-submersible length and width are not provided and are estimated to be 70 m by Chen et al. (2015). The mass of the prototype semi-submersible is 44,000 tons. The model tests were conducted in 1:70 scale. Therefore, simulations are performed for the 1:70 model.

(a)   (b)
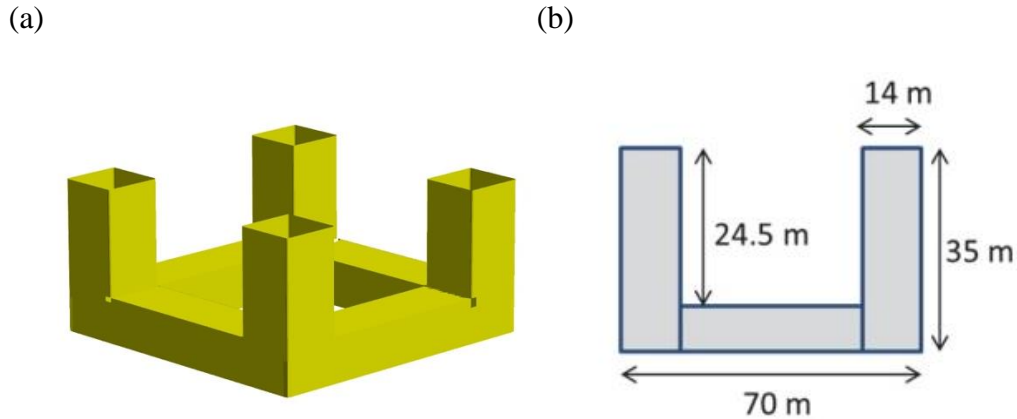
Figure. 49 Dimensions of the semi-submersible platform

Figure. 50 (a) demonstrates the grid structure around the semi-submersible. Structured multi-block overset grids are used. Since only horizontal motion is considered, all computational blocks are moving together with the semi-submersible, without calling PEGSUS at every time step. The characteristic length of the full-scale model is set as the column width L=14 m; and the characteristic length of the model-scale model is set as L=0.2 m. The four pontoons are covered by one block with 258×31×52 boundary fitted grid. Each of the four columns is surrounded by one block, which has the dimensions of 162×50×31. Eight small blocks are used for connection between the major blocks around columns and pontoons to allow for data communication. In total, 1.57 million grid points in thirteen blocks are used for the platform. The characteristic velocity V is set as 1 m/s in

122

full scale and 0.119523 (1/$\sqrt{70}$) m/s in model scale. The characteristic time is acquired by dividing L with V and is 14 s and 1.6733 s, for prototype and model scale, respectively. Table 12 summarizes the characteristic parameters for both prototype scale and model scale.

Table 12. Summary of characteristic length, velocity, and time

	Characteristic length (m)	Characteristic velocity (m/s)	Characteristic time (s)
Prototype	14	1	14
Model	0.2	1/$\sqrt{70}$	1.6733

The corner rounding effects of columns play a significant role in VIM sway amplitudes in accordance with simulations performed by Chen et al. (2016). The columns were sharp cornered in Waals et al. (2007). However, the geometry details of how sharp the corners are in the model test are not available. The sharp corners are also considered for the columns in the studies by Chen et al. (2016) and this study, and the associated diagonal column width is approximated to be D=1.385L=19.385m. Figure. 50 (b) demonstrates the simulation domain with the range of $-10 \leq$ x/L ≤ 28, $-16 \leq$ y/L ≤ 16, and $-11 \leq$ z/L ≤ 0. To resolve the near field flows, a fine grid basin is designed with the range of $-10 \leq$ x/L ≤ 28, $-6.32 \leq$ y/L ≤ 6.32, and $-3.1 \leq$ z/L ≤ 0. The coordinate system origin is at the center of the cut plane of the semi-submersible at water surface. Grid spacing in the x- and y-directions increases considerably in the far field ocean far away from the basin. These stationary background grids are divided into four blocks and add another 0.62

million grid points. Overall, the simulation system has 2.19 million grid points in 17 blocks. The sensitivity studies on time step and mesh density were performed by Chen et al. (2016). The mesh density adopted in this study is proved to be suitable. The time step size is selected as 0.05 dimensionless time, which is the same as time step used by Chen et al. (2016). The 0.05 dimensionless time is equivalent to 0.7 s for the prototype mooring line simulation and 0.0837 s for the model-scale hull simulation, which are obtained by multiplying 0.05 with the corresponding characteristic time specified in Table 12.
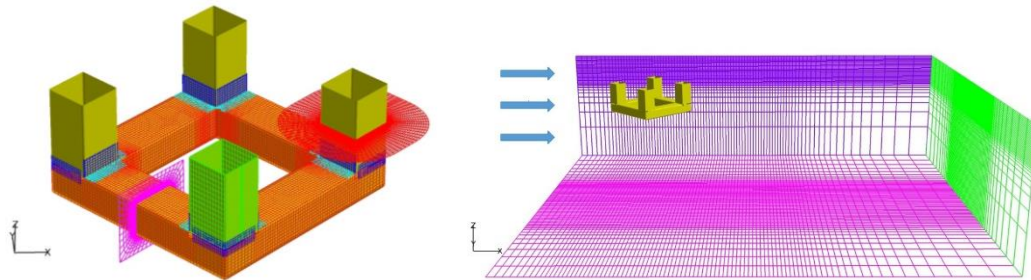
Figure. 50 (a) Grids around the floater; (b) Background grids and the computational domain

The initial position of the floater motion center is at x = 0 and y = 0, coincident with the coordinate system origin. The current speed is determined based on the target reduced velocities. The reduced velocity is defined by $V_r = UT_y/D$, where U is the current speed, T_y is the natural period of the transverse (sway) motion, and D is the projected width of the columns normal to the inflow, which is the diagonal column width. According to simulations achieved by Chen et al. (2016), the sway natural period is 203 s when D is

19.385 m. Therefore, the input current velocities can be determined by the known reduced velocities and the Reynolds numbers are determined based on the current velocities and the characteristics length. Reduced velocities of 7, 8, 9, 10, and 15 are selected for the VIM simulation to facilitate the comparison of the present simulation results with those obtained by Chen et al. (2016) and model tests, covering both the lock-in and post-lock-in situations.

The highest sway response is typically found for the current heading from 30 to 45 degrees with respect to the column face in accordance with Koop et al. (2016), thus 45 degree is selected to be the current heading, which is shown in Figure. 50 (b). Symmetry condition is imposed for the free surface (z = 0 plane). Neumann boundary condition is set for velocity in x and y directions, pressure, and turbulence on the free surface. As free surface's vertical motion is not considered, the velocity in z direction is given by the Dirichlet boundary condition. The same situation works for the bottom surface of the entire fluid domain, on which the vertical velocity is zero. Inlet boundary condition with prescribed current speed is applied to the x/L = −10 leftmost plane. Neumann conditions for velocity components and linear extrapolation for pressure are used on the rightmost outlet boundary plane of x/L = 28, as the current moves continuously across the downstream boundary. The velocity in y direction is set to have Dirichlet boundary condition on the boundaries at y/L = 16 and −16, while other parameters are defined with Neumann boundary condition. The wall clock time for each time step of computation is about 12 to 14 seconds.

6.3 Mooring Systems with Different Damping

Detailed mooring information is not available in the experiments performed by Waals et al. (2007). However, both surge and sway natural periods were provided in the experiments. Chen et al. (2015) estimated the associated mooring stiffness by adjusting the mooring stiffness to match the natural periods of the semi-submersible model in Waal's experiments. The stiffness in surge direction k_X is approximately 236,000 N/m and the stiffness in sway direction k_Y is approximately 92,600 N/m.

The identical surge and sway mooring stiffness is used in this study. At first, springs with the target stiffness k_X and k_Y, but without any damping effects, are modeled to simulate the scenario of model tests, in which soft springs are used to provide horizontal restoring force. The simulated VIM sway amplitudes with damping-free springs are to be compared to the model tests by Waals et al. (2007), model tests by Xu et al. (2012), and the CFD simulation by Chen et al. (2016).

Prototype mooring systems at different WDs are then designed and established in the MOORING3D version decoupled from FANS. The MOORING3D models are integrated with FANS code to achieve the coupled CFD-FEM analysis after validation by comparing to Orcaflex models. Semi-submersible platforms are mostly deployed in deep-water or ultra-deep-water fields. Semi-taut chain-polyester rope-chain mooing system is commonly used for the station keeping of the semi-submersible platform. Three WDs are selected for all of the cases with different reduced velocities, including 2500 m, 1750 m, and 1000 m. Additionally, for the WD of 2500 m, besides the conventional configuration of 16 mooring lines, another mooring system with 8 mooring lines is designed for

comparison. Mooring lengths are adjusted in the decoupled MOORING3D version to match the surge and sway mooring stiffness adopted by Waals et al. (2007) for each mooring configuration.
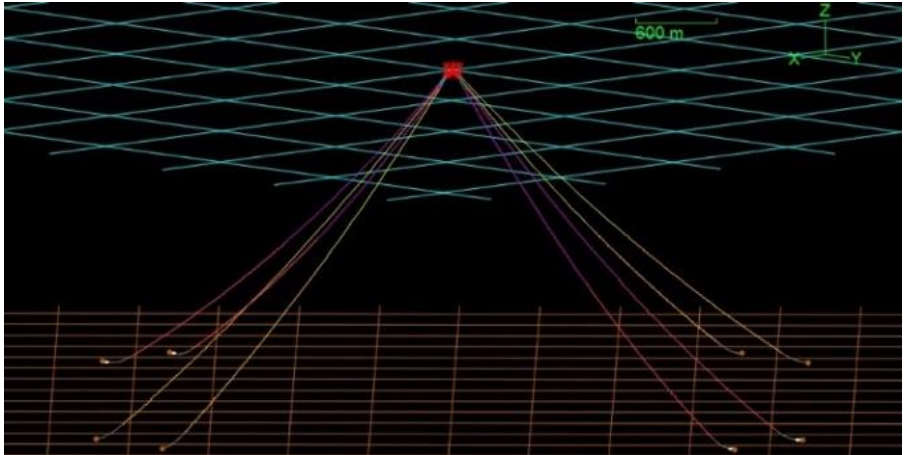
(a) 16-point mooring system
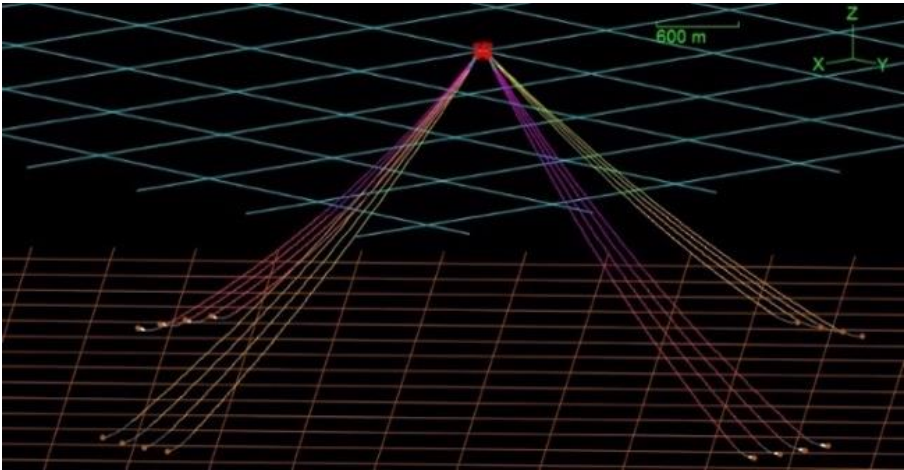
(b) 8-point mooring system

Figure. 51 The configuration of 16-point and 8-point chain- rope-chain

mooring system

Regarding the 16-point chain-polyester rope-chain system, the system has sixteen mooring lines. The fairlead angle is about 45 degrees for each mooring line. Each mooring line has three sections, including studless Grade R4S platform chain, polyester rope, studless Grade R4S anchor chain, and mooring connectors between them. The 16-point system is composed of four bundles, with each bundle located at each corner with the azimuth of 0 degree, 90 degrees, 180 degrees, and 270 degrees. Each bundle comprises of four mooring lines, with 4 degrees separation between adjacent lines within the same bundle group. The static configurations of all mooring systems are established by both Orcaflex and MOORING3D. Figure. 51 (a) displays the static configuration of the 16-point mooring system when the WD is 2500 m. Turning to the 8-point mooring system, the system is also composed of four bundles with the angular spacing of 90 degrees. Yet each bundle includes only two mooring lines. The configuration of the 8-point mooring system under the WD of 2500 m is specified in Figure. 51 (b). It can be seen that the mooring lines are almost taut for both 16-point and 8-point system. The touch down sections lying on the seabed are relatively short and the seabed-induced friction is negligible.

Line composition and properties of the 2500 m WD 16-point mooring system are presented in Table 13 as an example. Only lengths of chain and rope section are adjusted to make the mooring stiffness equal to target surge and sway stiffness of 236,000 N/m and 92,600 N/m to design 16-point mooring systems of 1000 m WD and 1750 m WD. All other line properties as listed in Table 13 remain identical. The drag coefficients are determined based on the Reynolds number around the mooring lines and the sensitivity

study of the drag coefficients will be discussed in Section 3.2.2. In terms of the 8-point mooring system at 2500 m WD, an equivalent mooring line is formed by combining two adjacent mooring lines within each bundle of the 16-point system to obtain an equivalent 8-point system. The young's modulus remains the same, but the unit weight is doubled. The corresponding cross-sectional area increases by 2 and the outer diameter increases by $\sqrt{2}$.

Table 13. Summary of mooring line composition and properties

	R4S Platform chain	Polyester Rope	R4S Anchor Chain
MBL (KN)	23559	21600	23599
Unit weight (kg/m)	493	52.5	493
Length (m)	132	3753	270
Diameter (mm)	157	274	157
Drag Coefficient	2.2	1.0	2.2

The current not only exerts drag loads on the semi-submersible hull, but also exerts drag loading on the mooring system. For simplicity, a shear current profile extending from sea surface to the depth of 750m is assumed in MOORING3D to model current applied on the mooring system. The surface current magnitude is determined based on the target reduced velocities. The current velocity decreases linearly from surface current velocity to zero at the 750m WD, as WD increases. Current velocity normally decreases as depth increases in the field; therefore, linear shear current is assumed for simplification.

Mooring system stiffness is one of the crucial parameters that determine the in-line surge offset and the crossflow VIM transverse response. The mooring system stiffness curves in both in-line and crossflow directions are generated in Orcaflex and MOORING3D. The resultant stiffness curves are compared to the target stiffness of k_X and k_Y, 236,000 N/m and 92,600 N/m, respectively. Figure. 52 and Figure. 53 display the comparison between simulated mooring stiffness and target stiffness in 2500 m WD and 1750 m WD, respectively. Three stiffness curves almost overlap with each other. In case of 1000 m WD, Figure. 54 shows the comparison of the mooring stiffness in surge and sway. Both Orcaflex and MOORING3D models show that the surge stiffness increases by about 5% to 10% compared to the target stiffness 236,000 N/m when offset exceeds 6 m. The nonlinearity of the surge stiffness will affect the surge natural periods at large offsets but exerts little impact on the transverse motion. In terms of the transverse direction, the sway mooring stiffness curves obtained by both MOORING3D and Orcaflex still overlap with the target stiffness of 92,600 N/m. Figure. 55 shows the mooring stiffness comparison in terms of the 8-point mooring system at 2500m WD. The stiffness curve comparison validates the MOORING3D models by comparison to Orcaflex models.

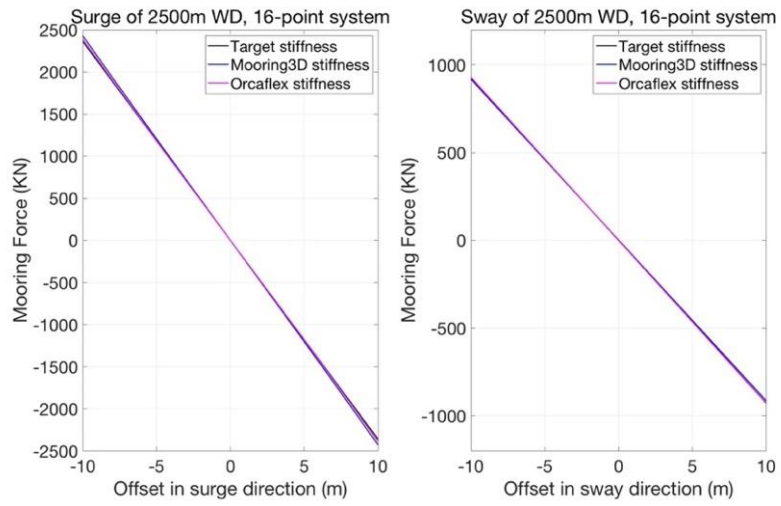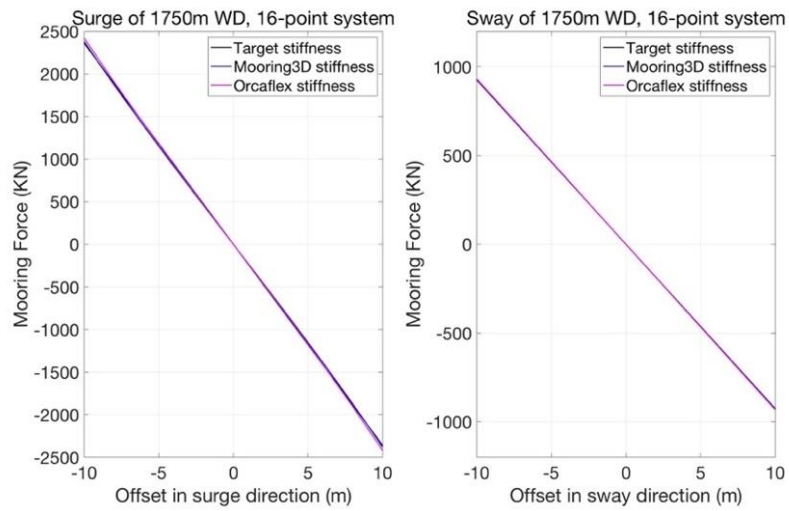**Figure. 52 Mooring stiffness comparison at 2500 m WD**

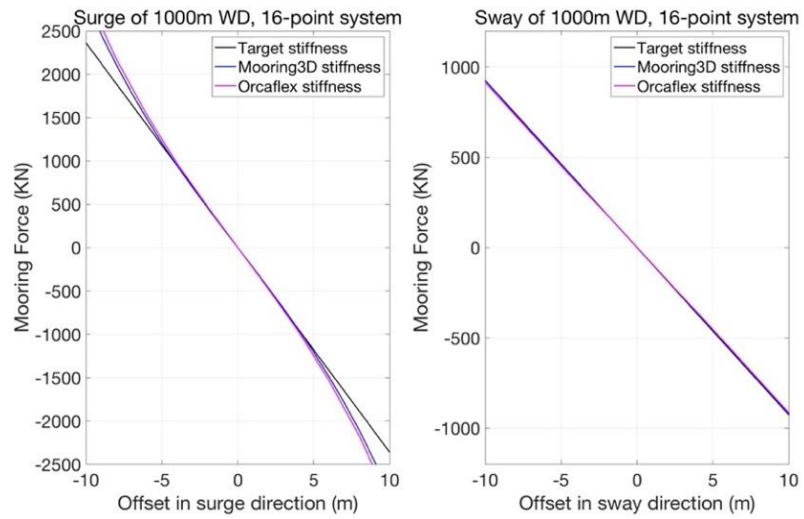**Figure. 53 Mooring stiffness comparison at 1750 m WD**

131

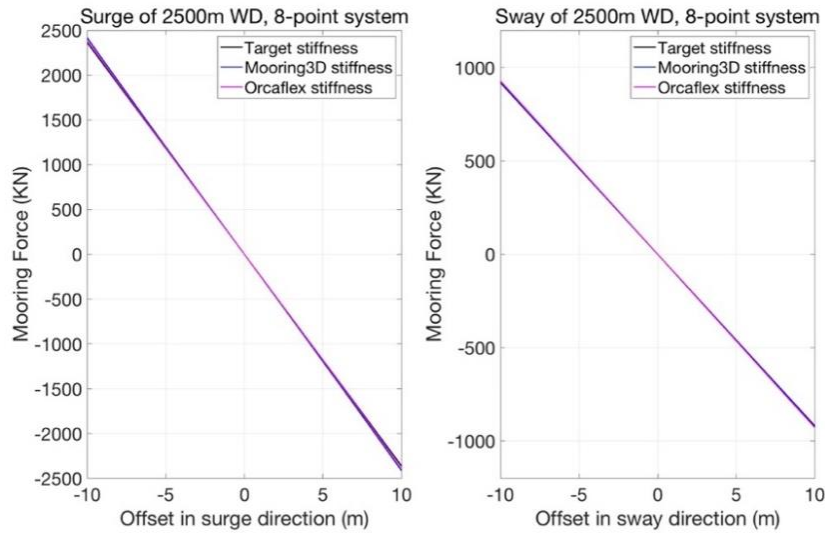**Figure. 54 Mooring stiffness comparison at 1000 m WD**

Figure. 55 Mooring stiffness comparison of 8-point system at 2500 m WD

6.4 Simulated Results with Ideal Damping-free Mooring System

Dimensionless quantities are used in the FANS code. Figure. 56 displays the simulated normalized surge and sway motion histories with ideal damping-free mooring system modeled as single springs, when the reduced velocity (Vr) is 7, 8, 9, 10 and 15. The left plots show the surge motion time histories, and the right plots show the sway motion time histories for all of the five reduced velocities. The dimensionless X and Y time histories in these figures are additionally normalized by dividing diagonal column width D. As Vr increases, the normalized surge offset increases from approximately 0.2 (Vr=7) to approximately 0.68 (Vr=15). The sway amplitudes are to be compared with model test results obtained by Waals et al. (2007) and by Xu et al. (2012) and are to be discussed in this section.

The average sway periods under each reduced velocity are extracted and are summarized in Table 14 below. It is observed that as Vr increases, the average period decreases. The average period when Vr is 7 is very close to the sway natural period of 203 s, as provided by Chen et al. (2016). This indicates the phenomenon of "lock-in". The sway natural period of the semi-submersible is dominated by the vortex shedding frequency. When frequency of vortex shedding matches the resonance frequency of the floating system, the floater can begin to resonate, vibrating with harmonic oscillations driven by the energy of the flow. The vortex shedding period and the associated sway period is "locked-in" to the sway natural period of the system, therefore the sway period 202 s when Vr is 7 is very close to the sway natural period 203s.

In terms of other reduced velocities, the period result matches well with the general trend as indicated by the equation of Strouhal number: $St = fL/U$, where f is the vortex shedding frequency, U is the current velocity and L is the characteristic length, which can be relating to body dimension or motion amplitude. The vortex shedding period decreases with increasing current velocity.

Table 14. Summary of average sway periods (Reprinted from Huang et al., 2020)

Reduced velocity	7	8	9	10	15
Average sway period	202 s	186 s	182 s	171 s	136 s

y in Figure. 56 should be normalized by dividing D to compare with model test results obtained by Waals et al. (2007) and by Xu et al. (2012). The nominal amplitude is used and defined as $\sqrt{2}\sigma(y)$ to represent the average motion responses, where σ(y) is the standard deviation of y(t). The statistical analysis includes data only after the response motions are stabilized to minimize errors caused by somewhat shorter numerical simulations. Table 14 shows that the average sway periods decrease as reduced velocity increases. Hence longer duration of 4200s is considered for Vr of 7, 8, and 9 and shorter duration of 2800s is used for Vr of 10 and 15. The stabilized transverse motion time histories of all reduced velocities include sufficient cycles to extract the nominal amplitudes. Figure. 57 shows the comparison of the experimental nominal sway amplitudes by Waals et al. (2007) and by Xu et al. (2012), simulated sway amplitudes by Chen et al. (2016) with D=1.385L, and sway amplitudes of the simulation in this study at Vr=7, 8, 9, 10, and 15.
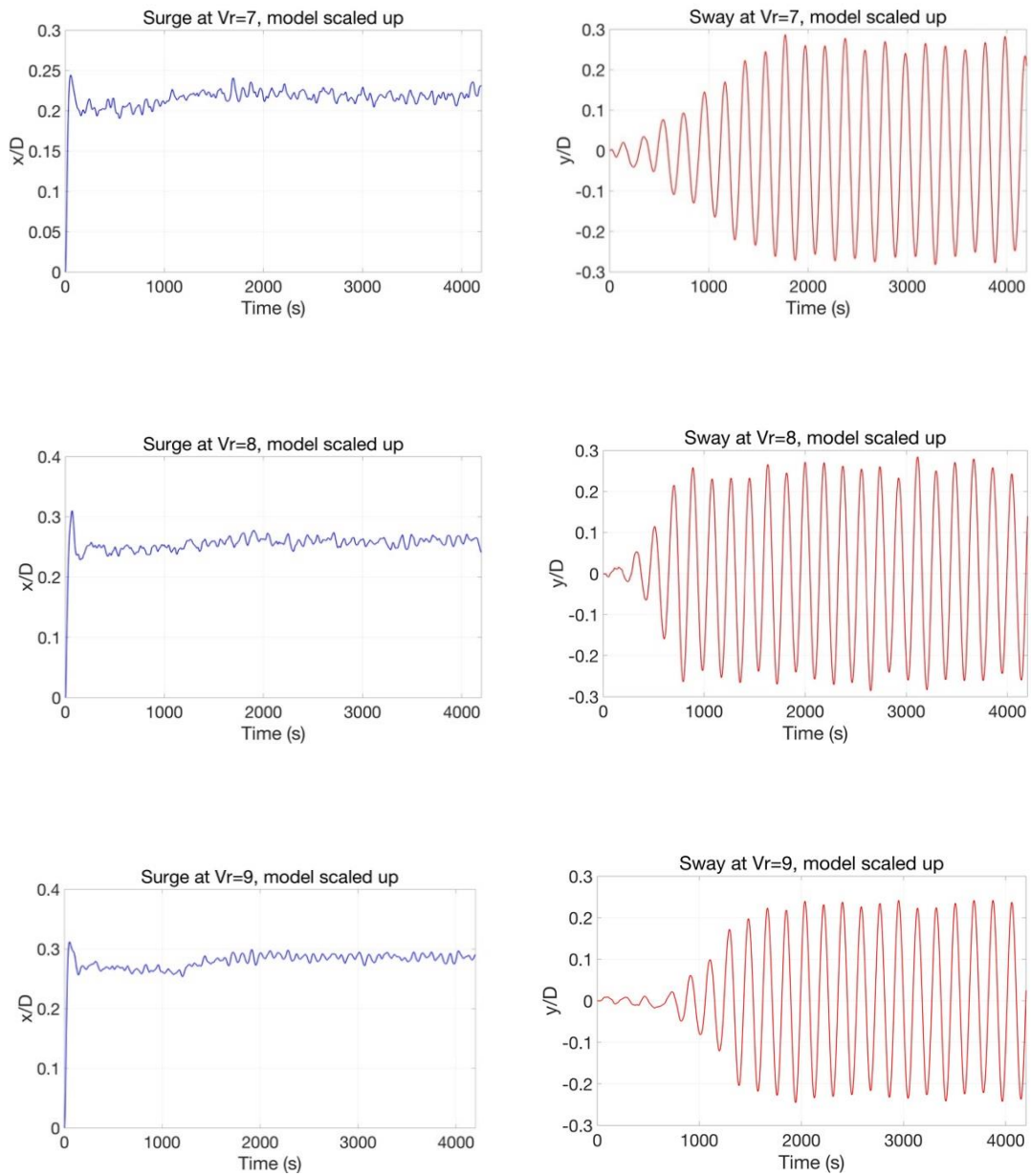
Figure. 56 Motion histories of the model scale semi-submersible in surge and sway direction (Reprinted from Huang et al., 2020)
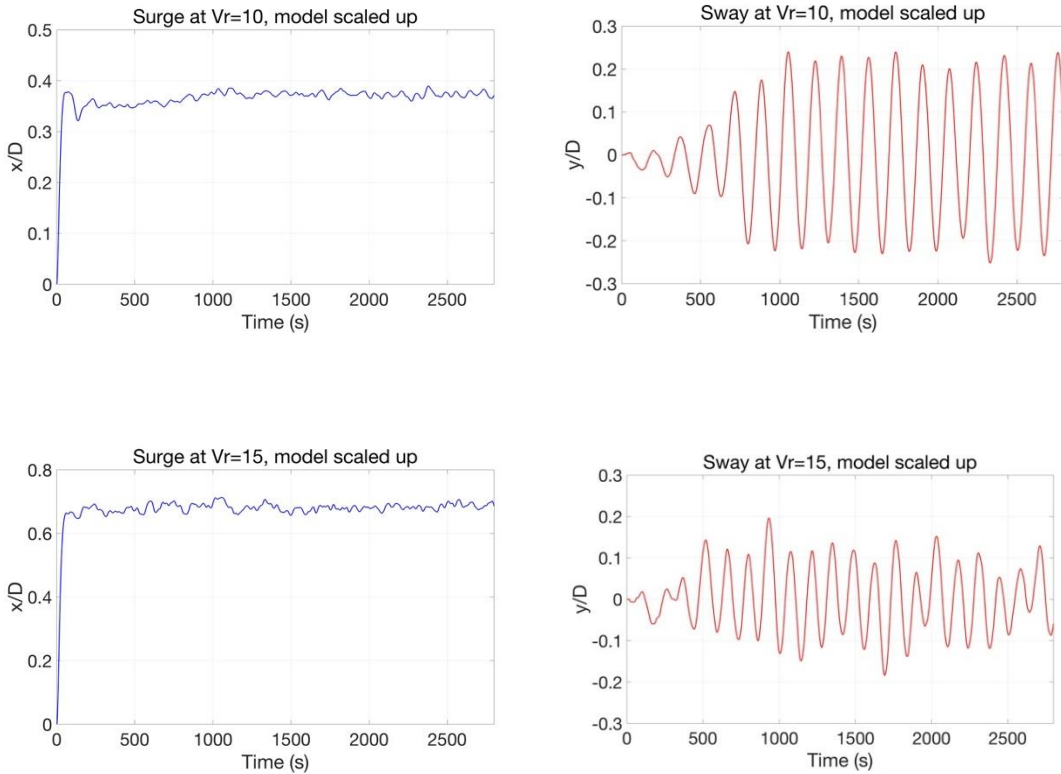
Figure. 56 (Continued) Motion histories of the model scale semi-submersible in surge and sway direction (Reprinted from Huang et al., 2020)

The comparison in Figure. 57 shows that the simulated nominal transverse amplitudes by this coupled analysis generally agree well with the CFD simulations by Chen et al. (2016). Reduced velocities of 7 and 8 represent lock-in range and reduced velocity of 15 represents the post lock-in range. Reduced velocities of 9 and 10 indicate the transitional range between lock-in and post-lock-in, and corresponding simulations are performed. The results at reduced velocities of 7, 8 and 15 are in close proximity with the previous CFD results. Simulations with Vr of 9 and 10 were not performed by Chen et al. (2016). However, the results of this coupled analysis still generally agree well with the regression line. Since the dimensions of the semi-submersible adopted in both studies are

identical but mesh density is different, the comparison also verifies that the results are not sensitive to the mesh density selected, and that the mesh density adopted in this study is sufficient for VIM modeling.

Waals et al. (2007) pointed out that small differences in the geometry might cause different motion responses. On one hand, the increased draft in semi-submersible is responsible for the pronounced VIM, therefore the column aspect ratio H/L, is a major factor in motion responses. On the other hand, the roundness of the column corners can also affect the flow pattern and the associated motion responses. The column aspect ratio H/L=1.75 adopted in this study is identical to what is used by Waals et al. (2007). How the corner is rounded in the model test is unknown to us, therefore the corner rounding is approximated as D=1.385 L. The semi-submersible in Xu et al. (2012) had a smaller aspect ratio of H/L=1.45, but the corners were more rounded with D=1.2485 L.

Corresponding model tests at Vr=7 and Vr=8 were also performed by Waals et al. (2007) and Xu et al. (2012). The simulated transverse motion response of the coupled analysis for the sharp cornered geometry (D=1.385 L) is about 15% smaller than the Waals et al. (2007) measurement at Vr=7. The result by coupled analysis lies in between the results of two model tests at Vr=8. While a narrow lock-in range was revealed in Waals et al. (2007), the CFD simulation results of both this study and the study by Chen et al. (2016) show broader lock-in ranges, more in accordance with those of Xu et al. (2012). Chen et al. (2016) also performed CFD simulations with more rounded corners with D=1.283 L and with aspect ratio of 1.75. The simulations agree well with measurements by Xu et al. (2012) and manifest larger transverse amplitudes than simulations with D=1.385L and

137

tests by Waals et al. (2007), demonstrating that the rounding in the column corner is a substantial factor in semi-submersible VIM responses. The difference in how column corners are rounded may cause discrepancies between CFD simulations and model tests. More details in terms of validation of CFD simulation can be found in the study by Chen et al. (2016).

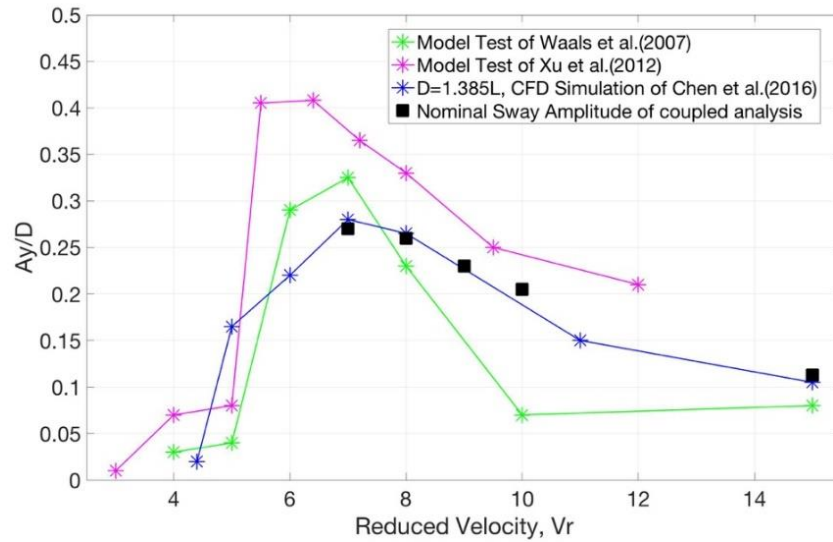**Figure. 57 Comparison of simulated nominal transverse amplitudes to previous simulation and model tests (Reprinted from Huang et al., 2020)**

6.5 VIM Amplitudes versus Mooring Systems at Various WDs

6.5.1 Motion Comparison

Details of simulation results for VIM cases with 16-point mooring systems at different WDs are investigated in this section. The current loadings are identical to the

simulation case with damping-free springs, and the corresponding reduced velocities are 7, 8, 9, 10, and 15.

Figure. 58, Figure. 59, Figure. 60, Figure. 61, and Figure. 62 present the comparison of transverse (sway) motion histories and motion trajectories of simulation cases with 16-point mooring systems of different WDs at the selected reduced velocities. The left plots show the sway motion comparison and the right plots show the trajectory comparison for all of the five reduced velocities of 7, 8, 9, 10, and 15. Generally, the sway amplitudes at 2500 m WD are smaller than sway amplitudes at 1750 m WD and 1000 m WD for all reduced velocities. The motion histories at three WDs all have smaller sway amplitudes than those of simulation with damping-free springs. It is also evident that the surge offset of all three cases with mooring systems are higher than that of the damping-free case, and the increase in offset is due to the current drag load acting on mooring lines, in addition to the hydrodynamic loads on the floater.

Table 15. Offset comparison of different WD mooring system (Reprinted from Huang et al., 2020)

Overall Water Depth	Offset when no current applied on	Offset with current applied on
1000	4.8882	5.9138
1750	4.9343	6.8402
2500	4.9874	7.3497

It is also observed that the horizontal in-line offset increases as WD gets larger. The same tendency is observed in a comparison model in Orcaflex. A constant horizontal current load in surge direction is applied on the semi-submersible hull. The same current profile extended to 750m WD is applied on all three mooring systems. The resultant offsets are summarized in Table 15. The summary reflects that under the same horizontal load on the hull but without any currents acting on the mooring lines, the in-line offsets are all around 4.9m and are almost identical. After current load is applied to the mooring systems, the horizontal offset increases as a result, and the growth in offset increases as WD increases. One possible reason is that the length of fairlead chain sections is longer for mooring lines placed in deeper areas, and the drag coefficient of chain is higher than that of polyester rope. The longer platform chain at large WD induces the rise in overall drag loads, leading to the rise in in-line offset as the water depth increases.

The surge offsets with mooring systems are higher than that of the damping-free case for most of reduced velocities, and the horizontal surge offset increases as WD increases. However, there is an exception to the surge offset at 1000m WD when Vr=15. The offset at 1000 m WD when Vr=15 appears smaller than that of the damping-free case. This is due to the slight increase in surge stiffness of 1000-m-WD mooring system when offset is larger than 5 m, as indicated in the left plot of Figure. 54. The average horizontal offset when Vr=15 is approximately 12.5 m, far more than 5 m, where the averaging surge mooring stiffness at 1000 m WD is larger than the target surge stiffness 236,000 N/m. As 236,000 N/m is still adopted by the damping-free case, the resultant horizontal surge offset subjected to "stiffer" in-line mooring stiffness at 1000m WD when Vr=15 appears smaller

than that of the damping-free case. However, though surge mooring stiffness deviates from the target stiffness at large offset, the sway stiffness and the resultant transverse motion are not affected at 1000m WD according to the discussion in Section 2.3. The following discussion verifies that the nominal sway amplitudes with 1000-m-WD mooring system is larger than that with mooring systems under greater water depths.
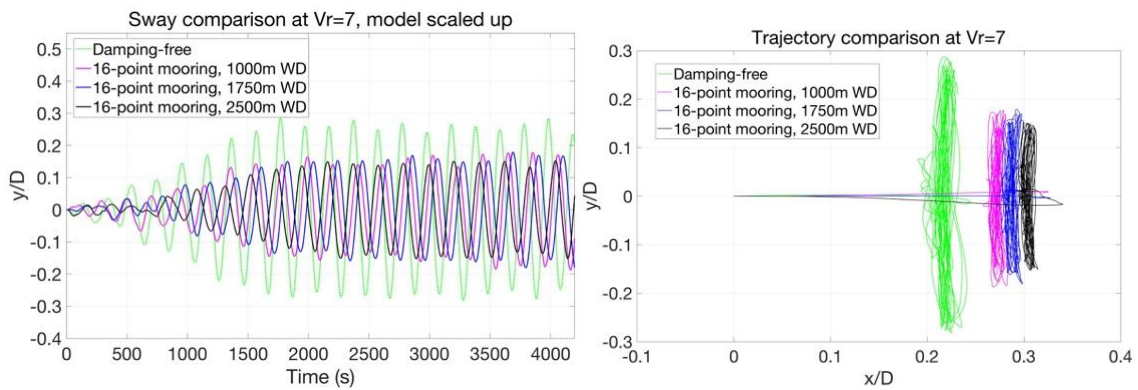

Figure. 58 Comparison of sway motion time histories & trajectory of Vr=7

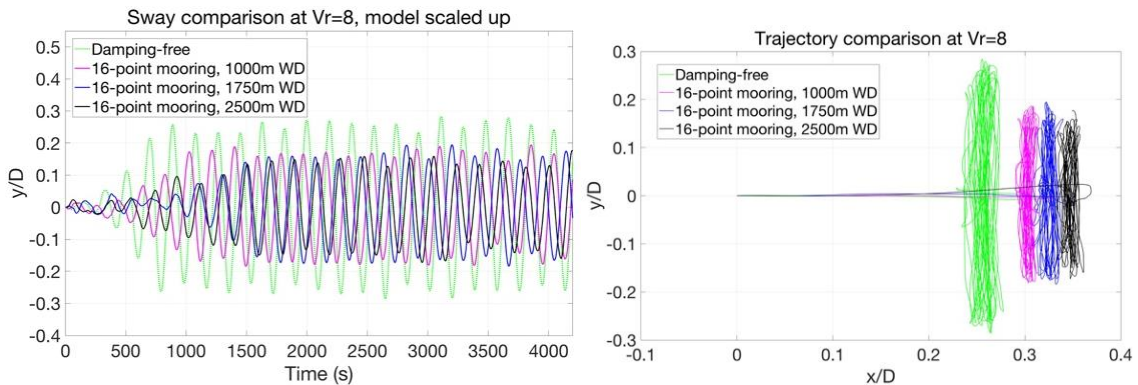**(Reprinted from Huang et al., 2020)**

Figure. 59 Comparison of sway motion time histories & trajectory of Vr=8

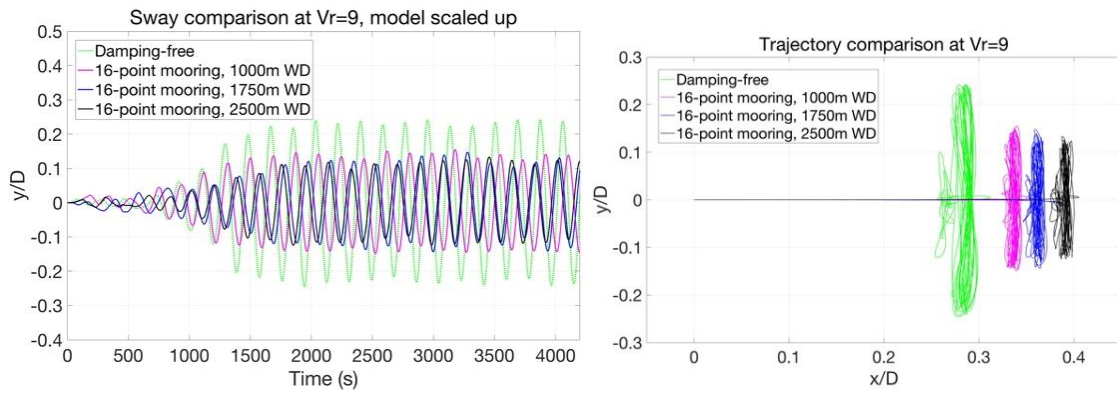**(Reprinted from Huang et al., 2020)**

Figure. 60 Comparison of sway motion time histories & trajectory of Vr=9

(Reprinted from Huang et al., 2020)

Figure. 61 Comparison of sway motion time histories & trajectory at Vr=10

(Reprinted from Huang et al., 2020)

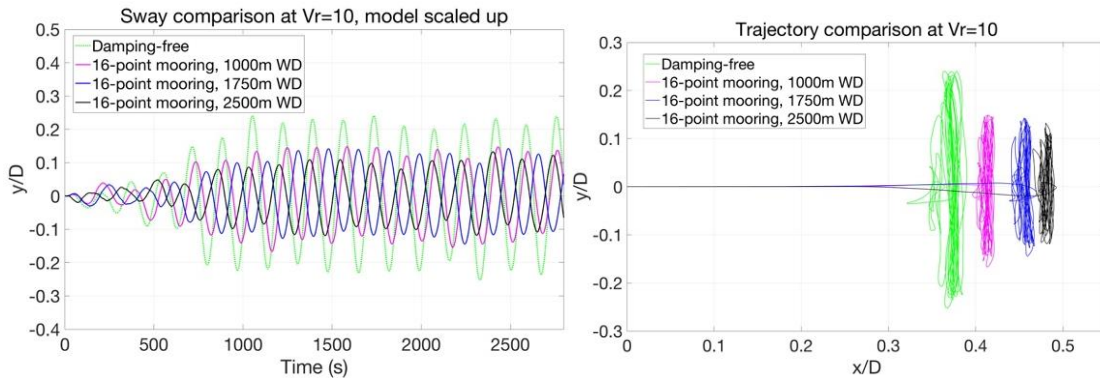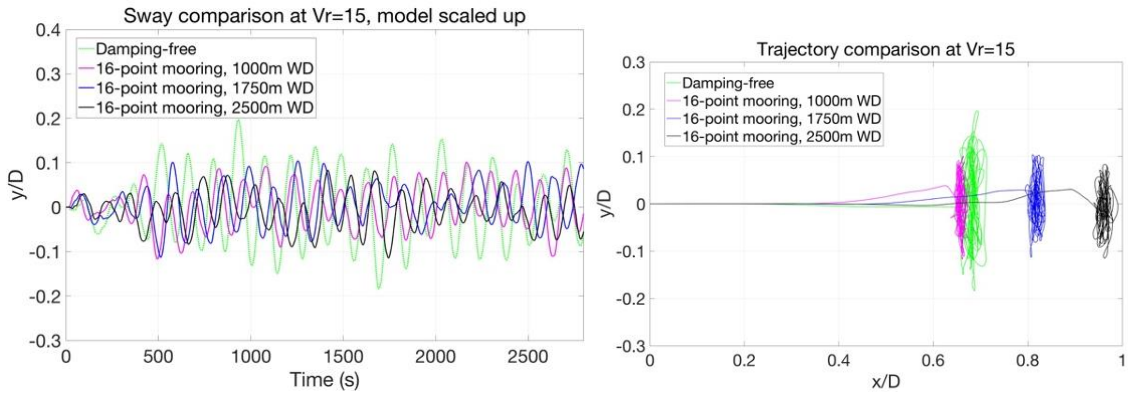**Figure. 62 Comparison of sway motion time histories & trajectory at Vr=15**

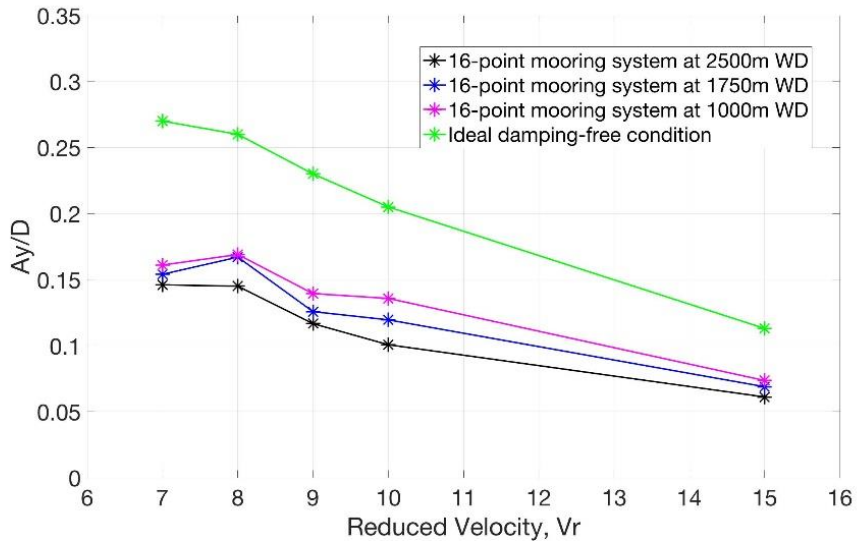**(Reprinted from Huang et al., 2020)**

Figure. 63 Comparisons of nominal sway amplitudes at different WDs

(Reprinted from Huang et al., 2020)

Nominal sway amplitudes are extracted from the motion histories through statistical analysis to achieve a clearer comparison of sway amplitudes between different

WDs. Figure. 63 illustrates a more straightforward comparison that how the nominal sway amplitudes vary with water depth. Generally, the nominal sway amplitude manifests a decreasing tendency as water depth increases and as reduced velocity increases.

The reduction should be attributed to the damping effects induced by mooring system. Brown et al. (1999) concluded that mooring system damping is caused by line hydrodynamic drag, line internal forces, and seabed interaction. Brown et al. (1999) also indicated that the dominating mooring line damping component is caused by hydrodynamic drag, and the contributions from the internal structural damping of the mooring line can be ignored. In terms of seabed friction, the touch-down sections of taut chain-polyester rope-chain mooring lines are short, thus friction effects from the seabed are negligible. The drag forces on the mooring lines cause the main damping effects. As water depth becomes larger, the mooring line overall length increases as a result, leading to the rise in the total drag area and the associated drag forces. The increasing water depth contributes to the increasing mooring damping effects, and consequently reduces the VIM sway amplitudes.

The reduction of VIM nominal sway amplitudes from damping-free condition to 1000 m WD is about 40% at Vr=7, and the reduction of VIM nominal sway amplitudes from damping-free condition to 2500 m WD is about 46%. The reduction ratios for 1000 m WD and 2500m WD are 35% and 44% respectively at Vr=8. The reduction ratios for two WDs are 39% and 50% respectively at Vr=9. The reduction ratios for two WDs are 40% and 51% respectively at Vr=10. The reduction ratios for two WDs are 35% and 46% respectively at Vr=15. The observed amplitude reduction demonstrates that mooring

damping effects are the major cause of the phenomenon that VIM amplitudes obtained in field measurements are much smaller than measurements from model tests. The reduction ratio of as high as 50% demonstrated by Ma et al. (2013) agrees well with the reduction range obtained in this study. How much the VIM response is reduced strongly depends on the magnitude of damping effects that can be provided by the mooring system.

In summary, although the mooring system could increase the overall damping effects, resulting in the reduction of the transverse motion by around 40% to 50%, the in-line offset increases as WD and current drag load increase. Though the reduction in transverse motion amplitudes can diminish the VIM fatigue damage for mooring lines and risers and increase their design lives, the increase in in-line offset gives rise to higher tension in the upstream mooring lines and risers. A comprehensive study is necessary while evaluating the impact of mooring damping on the VIM fatigue of associated mooring lines and risers.

6.5.2 Sensitivity Study of Drag Coefficients

The drag coefficient of 2.2 for chain sections and 1.0 for polyester rope which are adopted in this study are less conservative approaches in contrast to industry standard. More conservative factors are employed per industry standards. For instance, in ABS Guide for Position Mooring Systems or the DNV Offshore Standard DNV-OS-E301, the drag coefficients of chain and polyester rope are taken as 2.4 and 1.6, respectively. In the examples in API RP 2SK, the drag coefficients of chain and rope is recommended to be 2.2 and 1.2. The marine growth or corroded surfaces of mooring chains may additionally

145

lead to increasing chain surface roughness and consequently the rise in drag loading. The estimated chain drag coefficient 2.2 in this study is a little smaller than 2.4. However, the chain length is much shorter than rope, therefore its impact is less significant. The estimated rope drag coefficient 1.0 is determined based on the flow regime around the mooring lines and the approximation of initial surface roughness and is smaller than 1.6. It is expected that the VIM nominal sway amplitude reduction is sensitive to the mooring drag coefficients.

The coefficients of 2.4 and 1.6 of chains and ropes recommended by ABS and DNV are applied to the 16-point mooring system at 2500m WD to perform the sensitivity study on drag coefficients. The simulation is replicated at Vr=9 and the results of the sensitivity study are displayed in Figure. 64. The VIM reduction appears more considerable with the compliance of industry standards. The reduction of nominal sway amplitudes at Vr=9 from damping-free case reaches as high as 62%, more than 50% demonstrated by Ma et al. (2013). However, the conservative estimation of mooring line drag coefficients by industry aims at conservative analysis of mooring line tension and maximum offset. The over-estimation is too conservative in terms of coupled VIM analysis and drag coefficients of 2.2 and 1.0 are sufficient for the investigation of mooring damping effects on VIM.

It is also noted that the varying drag loading can exert impact on the average sway periods. The sway period is dominated by the vortex shedding period. The time history comparison in Figure. 64 indicates that the increasing mooring drag effects lead to a slight increase in vortex shedding period and the resultant transverse motion period. The

146

damping-free case period is 182.3s. The periods of 2500m-WD cases with smaller drag

coefficients and with industry-standard coefficients are 185.7s and 186.5s, respectively.

The increase is around 2%. As discussed in Section 3.1, the vortex shedding period can be

determined by Strouhal number, which is an empirical parameter based on oscillation

amplitude, current velocity, floater geometry, Reynolds number, etc. The determination

of Strouhal number of deep-draft semi-submersible remains unresolved, and how damping

affects vortex shedding period by changing motion characteristics and vortex-structure

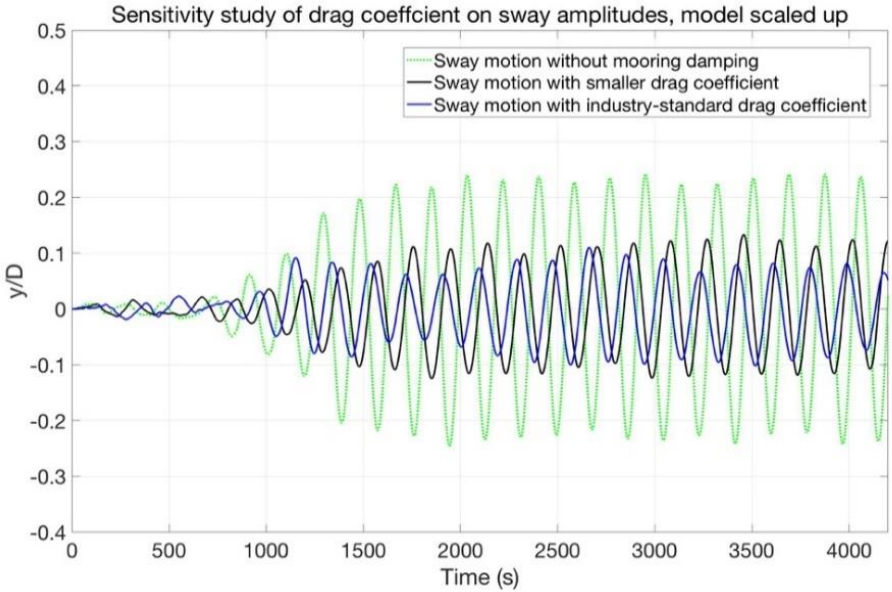interaction requires further research efforts and investigation.

Figure. 64 Sensitivity study of drag coefficient on sway amplitudes, Vr=9

(Reprinted from Huang et al., 2020)

6.5.3 Vorticity Contour Analysis

Snapshots of the vorticity contours are captured on z/L = −0.5 and z/L = −2, which are at the middle of the column and at the pontoon, respectively. The snapshots are taken at selected simulation cases when the transverse motion is fully developed. The vorticity is normalized by the characteristic length and velocity described earlier.

(a) Z-vorticity on the z/L=-0.5 and -2, with 16-point mooring at 2500m WD, Vr=7
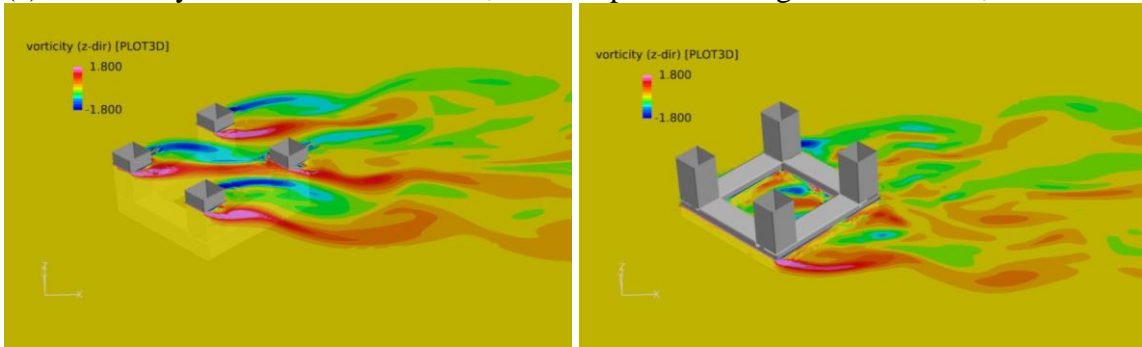
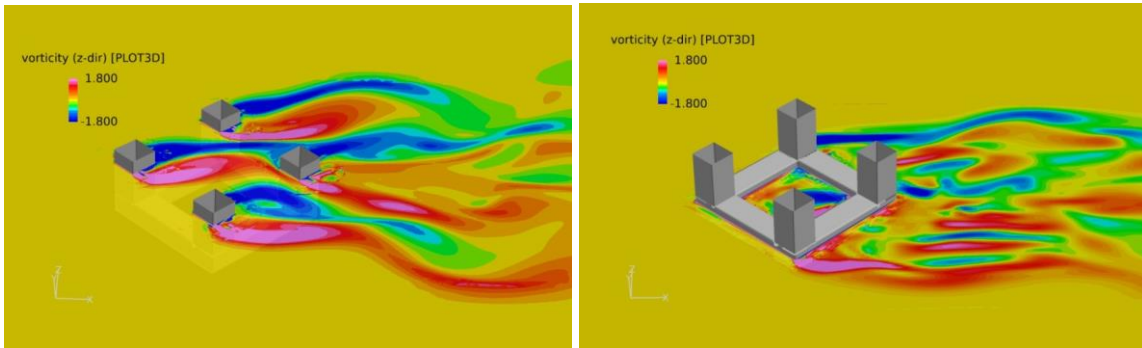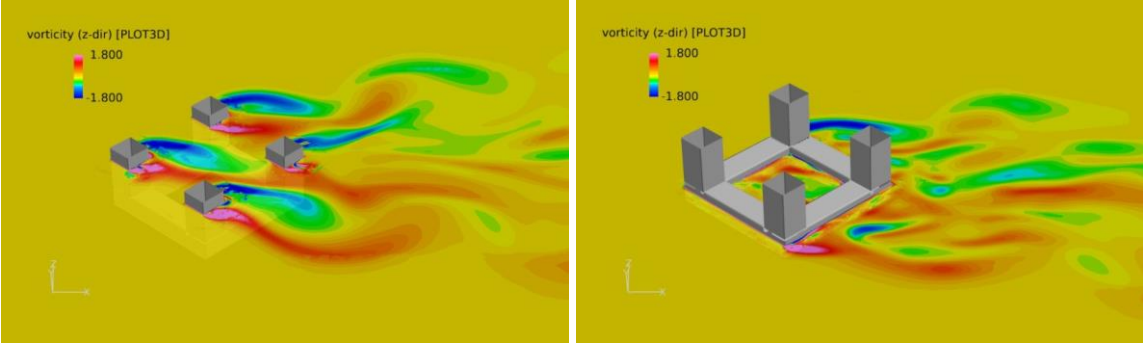(b) Z-vorticity on the z/L=-0.5 and -2 with 16-point mooring at 2500m WD, Vr=15

Figure. 65 Comparison between Z-vorticity contours at Vr=7 and Vr=15

Figure. 65 shows the comparison of vorticity contour scenarios for the 2500m WD between Vr=7 and Vr=15. Figure. 65 (a) shows the z-vorticity on the two horizontal planes when Vr=7 and Figure. 65 (b) shows the corresponding plots when Vr=15. Figure. 66 (a)

shows the z-vorticity at two elevations of the damping-free case when Vr=9, in which the sway amplitudes are the largest at this reduced velocity, and Figure. 66 (b) shows the z-vorticity on the two planes for the moored case at 2500m WD, in which the sway amplitudes are the smallest when Vr=9. Vr of 7 represents the lock-in condition, Vr of 15 represents the post-lock-in condition, and Vr of 9 represents the transitional range between the two. Additionally, Figure. 67 shows the three-dimensional z-vorticity of the case in Figure. 66 (b).

(a) Z-vorticity on the z/L = -0.5 and -2 plane, damping-free case, Vr=9

(b) Z-vorticity on the z/L=-0.5 and -2 plane, with 16-point mooring at 2500m WD, Vr=9
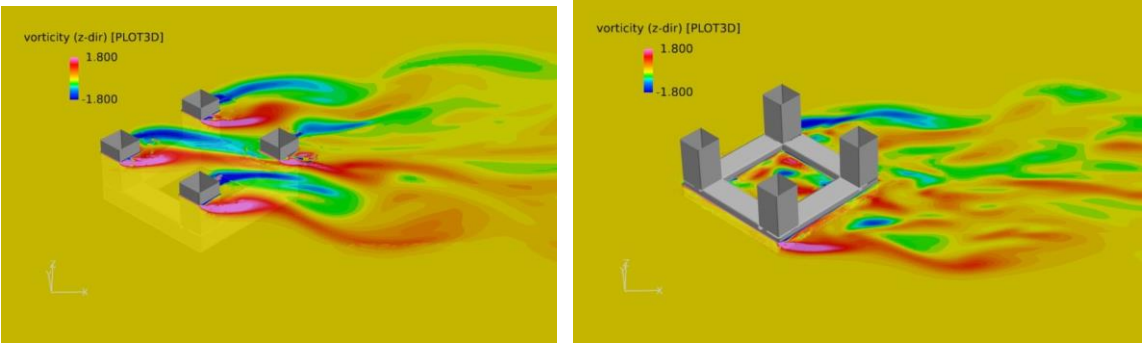
Figure. 66 Z-vorticity contours at Vr=9, at damping-free condition and moored condition
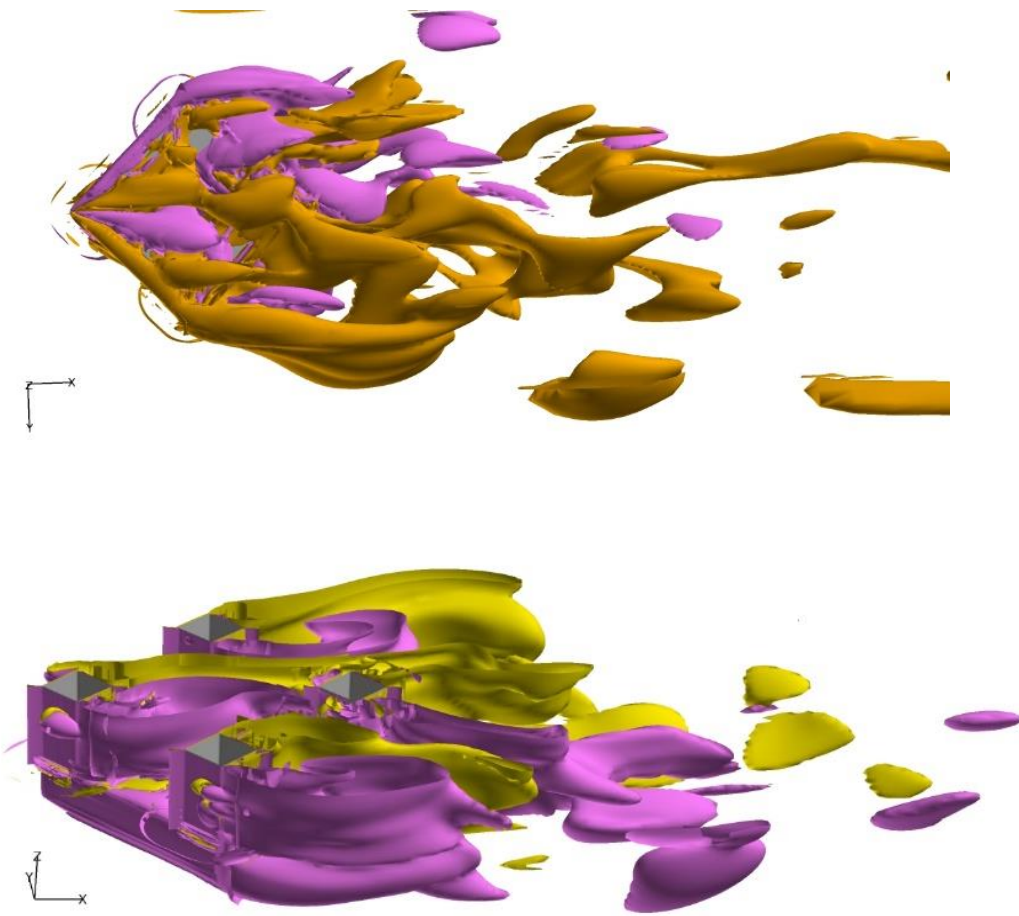
Figure. 67 3-D Z-vorticity contours of Vr=9 at moored condition

All these vorticity contours show a lot of violent swirls, an indication of large transverse motions. Figure. 65 reveals that as current velocity increases, the vorticity contours appear in longer and wider stretches and the case of Vr=15 manifests the longest and widest vortex stretches. Figure. 66 indicates that the difference between vorticity contours of the damping-free case and the 2500m WD case is not conspicuous in terms of flow pattern and vorticity strength. Figure. 65 and Figure. 66 indicate that the general pattern of vorticity contours and vorticity strengths are more dominated by the current

velocity than by the transverse amplitude. Figure. 67 indicates that strong vortex structures are also observed at the bottom of the semi-submersible. The vortices shed from the three upstream columns have little interaction with each other in all simulation cases, while the rear column is in the wake of the leading one and strongly affected by the vortices shed from it.

6.6 VIM Amplitude versus Mooring Line Number

Comparison is also performed between the sway motion histories of the semi-submersible with 16-point mooring system and those with 8-point mooring system at WD of 2500 m, to further prove that drag forces acting on the mooring lines are the main components of mooring damping effects.

Though mooring lines of the 8-point system has the equivalent diameter, $\sqrt{2}$ times that of the 16-point system, the total drag area of the 8-point system is still reduced due to the reduction of mooring line numbers. Theoretically, the VIM sway responses of the 8-point mooring system should be larger than that of the 16-point mooring system. Figure. 68 presents the comparison at 2500 m WD at Vr=7 and demonstrates that sway amplitudes with 16-point mooring system tend to be smaller than those with 8-point mooring system for all reduced velocities considered. The nominal sway amplitudes are extracted from motion histories and are presented in Figure. 69. The nominal sway amplitudes of simulation cases for Vr=7, 8, 9, 10 and 15 show amplitude reduction of 23%, 22%, 19%, 21%, and 17% from 8-point mooring system to 16-point mooring system, respectively.
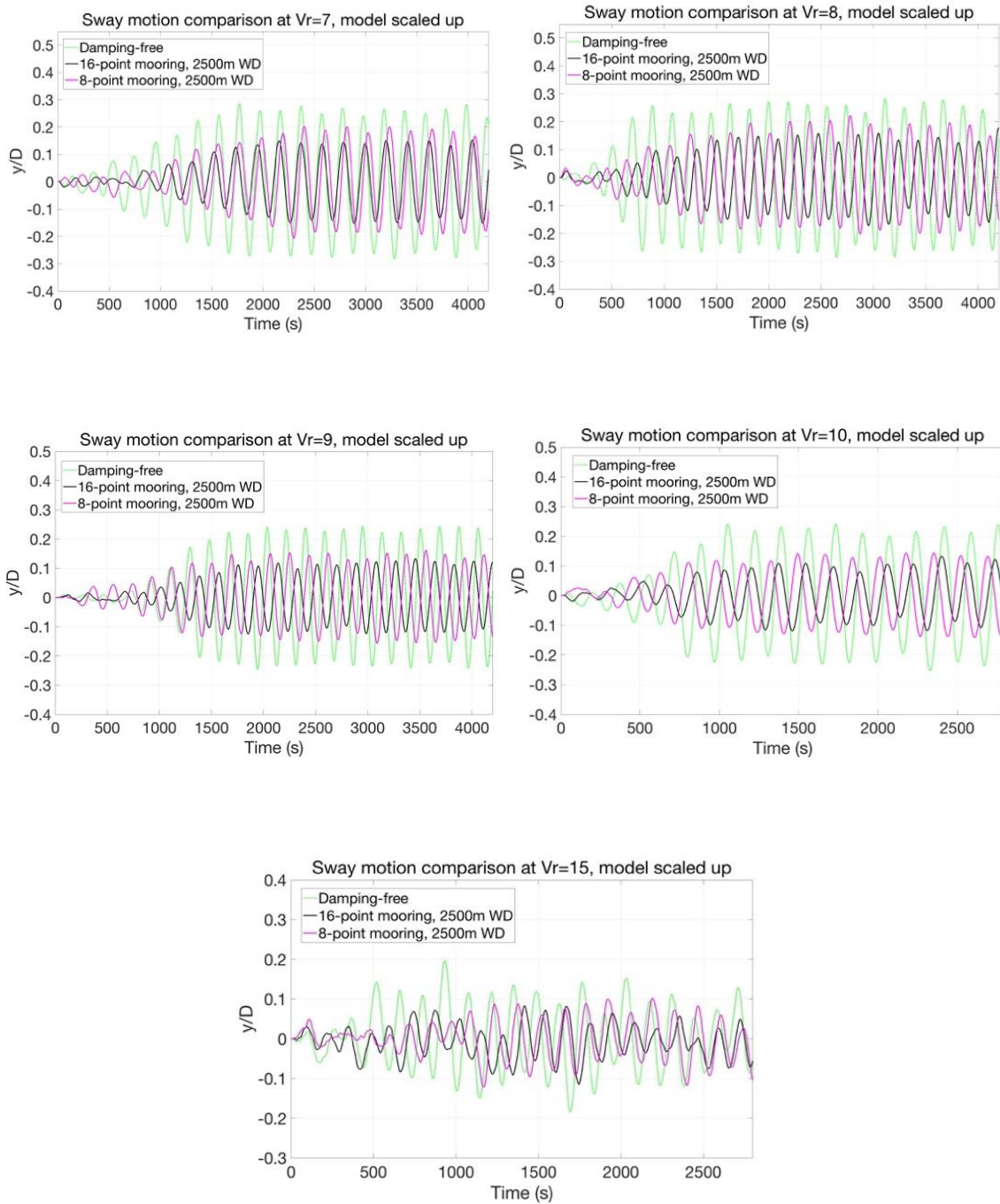
Figure. 68 Comparison of transverse motions between 8-point system and 16-point system at WD=2500 m, when Vr=7, 8, 9, 10, and 15. (Reprinted from Huang et al., 2020)

152
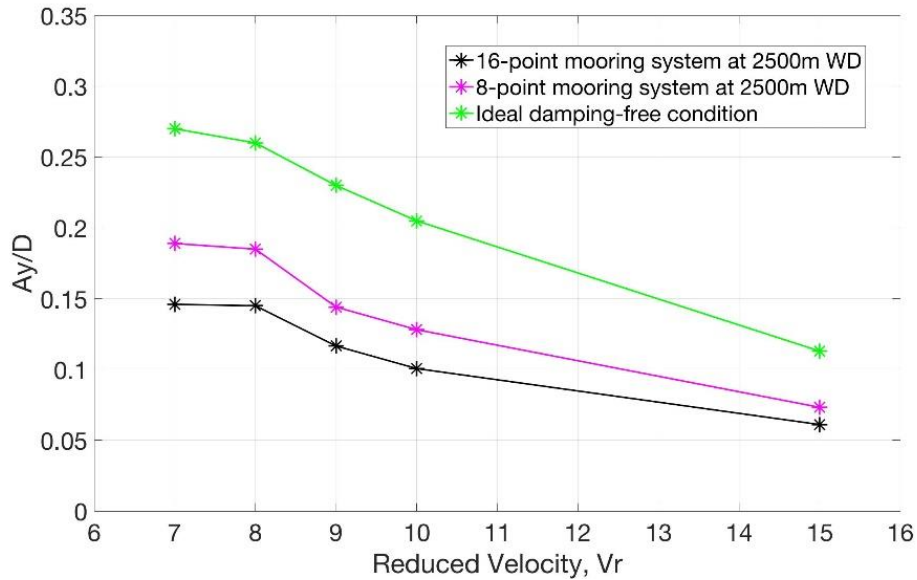
Figure. 69 Comparisons of nominal transverse amplitudes between 8-point system and 16-point system at 2500 m WD (Reprinted from Huang et al., 2020)

6.7 Summary

The 6-DoF motion solver and the MOORING3D in-house program are integrated with the FANS code for the time-domain coupled CFD-mooring simulation of VIM of a deep draft semi-submersible moored by a semi-taut chain-polyester rope-chain mooring system. At first, the simulation cases with ideal damping-free springs are conducted when the reduced velocity is 7, 8, 9, 10 or 15, and the motion responses generally agree very well with previous CFD simulations and the selected model tests.

Mooring systems which are stationed at WDs of 2500 m, 1750 m, and 1000 m are then designed to represent various damping levels for the investigation of the mooring-induced damping effects. The simulation results demonstrate that the in-line horizontal offset increases considering the drag loads applied on the mooring system. The nominal

transverse motion amplitudes show reduction which ranges from 40% to 50%, with comparison to the damping-free simulation cases. Since the mooring-induced damping effects are attributed to the drag forces on the mooring lines, the VIM amplitude reduction is sensitive to the selection of mooring line drag coefficients. Also, motion histories of simulation cases with 16-point mooring system and 8-point mooring system are compared, indicating that the 8-point mooring system simulation cases manifest larger sway amplitudes. The simulation results reveal that the mooring-induced damping effects represent a dominant contribution to the reduction in VIM transverse motion amplitudes in both lock-in range and post-lock-in range. The phenomenon, that field measurements of VIM response in the loop current events with operational sea states is found to be smaller than model tests, is probably caused by the damping effects from mooring system. Further investigation is recommended to assess the effects of mooring-induced damping on semi-submersible VIM for both model scale and prototype scale. The coupled model of FANS codes and the in-house MOORING3D program proves to be a powerful tool for the study of complex fluid-structure interaction coupled with mooring system.

CHAPTER VII

CONCLUSIONS

7.1 CALM Buoy's Responses in Wave and Currents

The FANS CFD code is coupled with the in-house FEM mooring analysis program, MOORING3D, to study the dynamic responses of a CALM buoy system in waves and currents. Model-scale free-decay in surge, heave, and pitch are simulated and validated by experimental comparison.

Regular waves with various time periods are generated with a numerical wavemaker. Model-scale simulations of the CALM buoy's wave-induced motion are performed, with RAOs compared to other numerical simulations or experiments. In terms of Buoy #1 with the slack chain mooring system, the coupled CFD-mooring analysis yields smaller RAOs in surge and heave directions and larger RAOs in pitch direction than AQWA-Orcaflex simulations. The range of change ratio agrees well with change ratio range from AQWA simulations to experiments which were obtained by Woodburn et al. (2005). The analysis indicates that viscous effects and free surface effects are critical in the buoy's responses in waves. In terms of Buoy #2 with the truncated mooring system, the RAOs agree well with experiments performed by Ryu et al. (2006) and manifest closer to experiments than previous simulations based on diffraction analysis.

The sensitivity study of the skirt demonstrates the skirt exerting limited influence on the buoy's RAO. The motion of the CALM buoy appears to be dominated by the inertial

and viscous effects of the buoy hull. The damping effects of the skirt seem limited due to its small cross-sectional area. However, the skirt proves beneficial in smoothing the motion and reducing irregular fluctuations.

The wave-current-body interaction simulations are performed for Buoy #2. The RAOs of the encounter periods match well with the corresponding experiments. The VIM in sway directions are significant in the current-only condition but shows reduction with the presence of waves. The amplitudes in roll and yaw directions are also diminished considerably in the wave-current combined condition.

The conclusions demonstrate that the accuracy of conventional diffraction approach in industry relies highly on the empirical estimation of damping effects; and, the coupled FANS-MOORING3D code provides accurate predictions of motion responses of floating systems under complicated environmental conditions.

7.2 VIM of Semi-submersibles

Field measurements of semi-submersibles reveal that the VIM responses are typically found to be smaller than those observed in model tests. The possible factors causing the VIM response reduction in the field measurements include Reynolds number, wave effects, mass ratios, and external damping from mooring lines. The FANS code is coupled with the six-DoF motion solver and MOORING3D, for the coupled CFD-FEM analysis of the VIM of a semi-submersible with a semi-taut chain-polyester rope-chain mooring system. The LES turbulence model is used to provide accurate estimation of hydrodynamic loading.

Simulations are performed for the 1:70 model of the platform under varying reduced velocities. Full-scale mooring systems with different water depths and mooring line numbers are designed to represent various levels of mooring damping effects. The simulated motions of the semi-submersible platform with different mooring systems are compared to the experimental data. The impact of mooring-induced damping on the resultant motion characteristics is investigated by the comparison. The comparison shows that mooring damping is probably one critical reason of VIM response reduction in the field. The results indicate that the coupled FANS-MOORING3D code proves to be a powerful tool in addressing complicated fluid-structure-mooring interaction.

REFERENCES

[1] Bunnik, T., de Boer, G., Cozijn, J., van der Cammen, J., van Haaften, E. and ter Brake, E., 2002. Coupled mooring analysis and large-scale model tests on a deepwater calm buoy in mild wave conditions, Proceedings of the 21st OMAE, Oslo, Norway, June.

[2] Chen, H.C., Patel, V.C., and Ju, S., 1990. Solutions of Reynolds Averaged Naiver-Stokes equations for three-dimensional incompressible flows. Journal of Computational Physics, Vol. 88, No. 2, pp. 305-336.

[3] Chen, H.C., Yu, K., 2006. Numerical simulation of wave runup and greenwater on offshore structures by a level-set RANS method. 16th international offshore and polar engineering conference, vol. III. May 28–June 2, San Francisco, California. p. 185–92.

[4] Chen, H.C., Yu, K., 2009. CFD simulation of wave-current-body interactions including greenwater and wet deck slamming. Comput. Fluids 38, 970–980.

[5] Chen, H.C., Chen, C.R. and Huang, K., 2013. CFD Simulation of Vortex and Wake-Induced Vibrations of Dual Vertical Risers. 23rd Int Offshore and Polar Eng Conf, Anchorage, USA, ISOPE, Vol. 3, pp. 433-440.

[6] Chen, C.R., Chen, H.C., 2015. CFD Simulation of Vortex-Induced Motions of a Deep Draft Semi-Submersible Platform. Proc ISOPE 2015, Hawaii, USA, ISOPE-I-15-636

[7] Chen, C.R., Chen, H.C., 2016. Simulation of Vortex-induced Motions of a Deep Draft Semi-submersible in Current. Ocean Engineering, Vol, 116, pp. 107-116.

[8] Chen, X., 2002. Studies on dynamic interaction between deep-water floating structure and their mooring/tendon systems. PhD dissertation, Texas A&M University, College Station, Texas, US, 2002.

[9] Cozijn, H., Uittenbogaard R., and Brake. E., 2005. Heave, Roll, and Pitch Damping of a Deepwater CALM Buoy with a Skirt. Proceedings of ISOPE 2005, Seoul, Korea, ISOPE-I-05-296

[10] Garrett, D., 1982. Dynamic analysis of slender rods. Journal of Energy Resources Technology 104(4), 302-306.

[11] Goncalves, R., Rosetti, G., Fujarra, A., and Oliveira, A., 2013. Experimental study on vortex-induced motions of a semi-submersible with four square columns, part II: effects of surface waves, external damping and draft condition. Ocean Engineering, vol. 62, pp. 10-24.

[12] Gu, H., 2017. Coupled Mooring Analysis of a CALM Buoy by a CFD Approach. Proc ISOPE 2017, San Francisco, USA, ISOPE-I-17-223.

[13] Gu, H., Chen, H.C., and Zhao, L., 2019. Coupled CFD-FEM Simulation of Hydrodynamic Responses of a CALM Buoy. Ocean System Engineering, Vol. 9, No. 1, pp. 21-42.

[14] Hong, Y., Choi, Y., Lee, J., and Kim, Y., 2008. Vortex- Induced Motion of a Deep-Draft Semi-Submersible in Current and Waves. Proc 18th ISOPE Conference, Vancouver, Canada.

[15] Huang, H. and Chen, H.C., 2019. Coupled CFD Analysis of Mooring Damping Effects on Vortex-induced Motions of a Deep Draft Semisubmersible. Proc ISOPE 2019, Hawaii, USA.

[16] Huang, H. and Chen, H.C., 2020. Investigation of mooring damping effects on vortex-induced motion of a deep draft semi-submersible by coupled CFD-FEM analysis. Ocean Engineering, Vol. 210, 2020.

[17] Huang, K., Chen, H.C. and Chen, C.R., 2010. Vertical Riser VIV Simulation in Uniform Current. ASME Journal of Offshore Mechanics and Arctic Engineering, Vol. 132, No. 3, Article No.031101.

[18] Huang, K., Chen, H.C. and Chen, C.R., 2012. Vertical Riser VIV Simulation in Sheared Current. International Journal of Offshore and Polar Engineering, Vol. 22, No. 2, pp. 142-149.

[19] Irani, M., Jennings, T., Geyer, J, Krueger, E., 2015. Some Aspects of Vortex Induced Motions of a multiColumn Floater. Proc OMAE 2015, St John's, Canada, OMAE2015-41164.

[20] Kang, Y., Sun, L., Kang, Z. and Chai, S., 2014. Coupled analysis of FPSO and CALM buoy offloading system in West Africa. Proceedings of the 33rd International Conference on Ocean, Offshore and Arctic Engineering, San Francisco, California, USA, June.

[21] Katayama, T., Tarao, Y., and Momoki, T., 2009. An Experimental Study on Viscous Effects on Heave Motion of Drifting Buoy. Proc ISOPE 2019, Osaka, Japan.

[22] Koop, A., Rijken, O., Vaz, G., Maximiano, A., Rosetti, G., 2016. CFD Investigation on Scale and Damping Effects for Vortex Induced Motions of a Semi-Submersible Floater. OTC 2016, Houston, USA, OTC-26977-MS.

[23] Koop, A., Wilde, J., 2016. Investigation on Reasons for Possible Difference between VIM Response in the Field and in Model Tests. Proceedings of the ASME 2016 35th, 2016, Busan, South Korea, OMAE2016-54746.

[24] Kurian, V., Liew, M., 2012. Dynamic Responses of Spar Acted upon by Random Wave and Current. 2012 IEEE Business, Engineering & Industrial Applications Colloquium (BEIAC), 2012 , Kuala Lumpur, Malaysia

[25] Le Cunff, C., Ryu, S., Duggal, A., Ricbourg, C., Heurtier, J., Heyl, C., Liu, Y. and Beauclair, O., 2007. Derivation of CALM buoy coupled motion RAOs in frequency domain and experimental validation. Proceedings of the 17th International Offshore and Polar Engineering Conference, Lisbon, Portugal, July.

[26] Liu, Y., Xiao, Q., Incecik, A., Peyrard, C., Wan, D., 2017. Establishing a fully coupled CFD analysis tool for floating offshore wind turbines. Renewable Energy, Volume 112, 2017, pp. 280-301

[27] Ma, W., Webster, W., 1994. An analytical approach to cable dynamics: theory and user manual. Sea Grant Project R/OE-26. Department of Naval Architecture and Offshore Engineering, University of California at Berkeley.

[28] Ma, W., Wu, G., Thompson, H., Prislin, I., Maroju S., 2013. Vortex Induced Motions of a Column Stabilized Floater. Proceedings of the International D.O.T. Conference, Houston, USA.

[29] Martin, B., and Rijken, O., 2012. Experimental Analysis of Surface Geometry, External Damping and Waves on Semi-Submersible Vortex Induced Motions. Proc OMAE 2012, Rio de Janeiro, Brazil, OMAE2012- 83689.

[30] Monroy, C., Ducrozet, G., Bonnefoy, F., Babarit, A., Gentaz, L. and Ferrant, P., 2011. RANS simulations of CALM buoy in regular and irregular seas using SWENSE method. International Journal of Offshore and Polar Engineering, 21(4), 264-271.

[31] Pontaza, J.P., Chen H.C., and Reddy, J.N., 2005. A local-analytic based discretization procedure for the numerical solution of incompressible flows. Int. J. Numer. Meth. Fluids, Vol. 49, pp. 657-699.

[32] Rijken, O. and Leverette, S., 2009. Field Measurements of Vortex Induced Motions of a Deep Draft Semisubmersible. Proc OMAE 2009, Honolulu, Hawaii, USA, OMAE2009-79803.

[33] Rijken, O., Schuurmans, S., and Leverette, S., 2011, Experimental Investigations into the Influences of SCRs and Appurtenances on Deepdraft Semisubmersible Vortex Induced Motion Response, Proc OMAE 2011, Rotterdam, the Netherlands, OMAE2011-49365.

[34] Ryu, S., Duggal, A. S., Heyl, C. N. and Liu, Y. 2005. Coupled Analysis of Deepwater Oil Offloading Buoy and Experimental Verification. International Society of Offshore and Polar Engineers, 2005-JSC-321.

[35] Ryu, S., Duggal, A. S., Heyl, C. N. and Liu, Y. 2006. Prediction of deepwater oil offloading buoy response and experimental validation. International Society of Offshore and Polar Engineers, 16(04), 290-296.

[36] Song, H., Chang, G., Hou, T., Zhang, J., 2014. Dynamic analysis of CALM buoy-based steel offloading line system. Proceedings of the 19th Offshore Symposium, Houston, Texas, February 2014.

[37] Sagrilo, L., Siqueira, M., Ellwanger, G., Lima, E., Ferreira, M. and Mourelle, M. J. A. o. R., 2002. A coupled approach for dynamic analysis of calm systems. Applied Ocean Research, 24(1), 47-58.

[38] Suhs, N. and Tramel, R. 1991. Pegsus 4.0 user's manual, Research Report No. ADA280608, Arnold Engineering Development Center, Arnold AFB, TN

[39] Waals, O., Phadke, A. and Bultema, S., 2007. Flow Induced Motions of Multi Column Floaters. Proc OMAE 2007, San Diego, California, USA, OMAE2007-29539.

[40] Woodburn, P., Gallagher P., Naciri, M., Borleteau, J., 2005. Coupled CFD Simulation of the Response of a CALM Buoy in Waves. Proc OMAE 2005, Halkidiki, Greece, OMAE2005-67063

[41] Xu, Q., Kim, J., Bhaumik, T., O'Sullivan, J., Ermon, J., 2012. Validation of HVS semi-submersible VIM performance by model test and CFD. Proceedins of OMAE 2012. Rio de Janeiro, Brazil. OMAE2012-83207.

[42] Yu, K., 2007. Level-set RANS Method for Sloshing and Green Water Simulations. PhD dissertation, Texas A&M University, College Station, Texas, US, 2007.

[43] Zhao, Y., 2014. Numerical Simulations of Violent Free Surface by a Coupled Level-set and Volume-of-fluid Method. PhD dissertation, Texas A&M University, College Station, Texas, US, 2014.